Master's Thesis

Messung der *W*-Helizität in Top-Quark Zerfällen mit dem ATLAS Experiment

Measurement of the *W*-Helicity in Top-Quark Decays with the ATLAS Experiment

prepared by

Cora Fischer

from Eschwege

at the II. Institute of Physics

Abstract

A measurement of the W-boson polarisation in top-quark decays is presented. The measurement was performed in the lepton+jets channel of top-quark pair events. The analysed data were collected with the ATLAS experiment in 2011 at a centre-of-mass energy of $\sqrt{s} = 7$ TeV in proton-proton collisions and correspond to an integrated luminosity of $\int \mathcal{L} \, \mathrm{d}t = 4.7 \, \mathrm{fb}^{-1}$. The event selection required either one electron or one muon, at least four high-energetic jets of which at least one must be tagged as a b-jet, and missing transverse momentum. Background contributions were either estimated from Monte Carlo simulation or measured via data-driven methods. For the measurement of the W-helicity fractions the angular variable $\cos \theta^*$ was used. A kinematic likelihood fit was performed to reconstruct the angular variable. The W-helicity fractions (longitudinal, left-handed, right-handed) were obtained by performing a template fit to data. Within this fit, a profiling method was used that estimates systematic uncertainties via fitting of nuisance parameters. Uncertainties that are not suited for profiling were evaluated via ensemble tests. The profiling fit was performed in four channels simultaneously (e+jets, μ+jets, 1 exclusive and 2 inclusive b-tags channels). The results are:

$$F_0 = 0.634 \pm 0.031,$$
$$F_L = 0.336 \pm 0.022,$$
$$F_R = 0.030 \pm 0.024,$$

for longitudinal, left-handed and right-handed helicity fractions, respectively. The measured values are in agreement with NNLO QCD Standard Model predictions [1], no significant deviation has been observed. Limits on anomalous Wtb couplings were set.

Zusammenfassung

Eine Messung der Helizität des W-bosons in Top-Quark Zerfällen wird vorgestellt. Die Messung wurde im Lepton+Jets Kanal von Top-Quark-Paar-Ereignissen durchgeführt. Die analysierten Daten wurden mit dem ATLAS-Experiment in 2011 bei einer Schwerpunktsenergie von $\sqrt{s} = 7$ TeV in Proton-Proton-Kollisionen aufgenommen. Die zugehörige integrierte Luminosität beträgt $\int \mathcal{L}\, \mathrm{d}t = 4.7$ fb^{-1}. Die Ereignisselektion verlangt entweder ein Elektron oder ein Myon, mindestens vier hoch-energetische Jets, davon mindestens einen Jet, der als b-Jet identifiziert wurde und fehlenden transversalen Impuls. Untergrund-Beiträge wurden entweder über Monte Carlo Simulationen oder mit Hilfe von datenbasierten Methoden abgeschätzt. Zur Messung der W-Helizitätsanteile wurde die Winkelvariable $\cos\theta^*$ verwendet. Um diese Variable zu rekonstruieren wurde ein kinematischer Likelihood-Fit durchgeführt. Die W-Helizitätsanteile (longitudinal, links- und rechtshändig) wurden über einen Template-Fit an Daten bestimmt. Dabei wurde eine Profiling-Methode verwendet, die die Abschätzung von systematischen Unsicherheiten über die Anpassung von Störparametern erlaubt. Unsicherheiten, die nicht für ein solches Profiling geeignet sind, wurden mit Hilfe von Ensemble-Tests evaluiert. Der Profiling-Fit wurde in vier Kanälen (e+Jets, μ+Jets, 1 exklusiv and 2 inklusiv b-tag Kanäle) simultan durchgeführt. Die Ergebnisse lauten wie folgt:

$$F_0 = 0.634 \pm 0.031,$$
$$F_L = 0.336 \pm 0.022,$$
$$F_R = 0.030 \pm 0.024,$$

entsprechend longitudinalem, links- und rechtshändigem W-Helizitätsanteil. Die gemessenen Werte sind in Übereinstimmung mit NNLO QCD Standardmodell Vorhersagen [1], es wurden keine signifikanten Abweichungen beobachtet. Ausschlussgrenzen auf anomale Wtb-Kopplungen wurden abgeleitet.

Contents

1. Introduction

Particle physics is the science that seeks to explore the smallest possible scales of nature: the fundamental constituents of our world, the elementary particles and the interactions between them. The exploration of the smallest scales requires high energies to gather the best resolution power that enables the investigation of fundamental particles. This is technically done by accelerating particles close to the speed of light and bringing them to collisions. The most powerful particle accelerator up to date is the Large Hadron Collider LHC, located at CERN, near Geneva. The LHC collides protons with protons at centre-of-mass energies of 7 TeV (in 2011) and up to 8 TeV (in 2012/2013). These high centre-of-mass energies allow the production of heavy particles that are not stable and cannot be observed otherwise in nature. The investigation of these particles helps to gather understanding of the most fundamental laws of nature. The theory that is known to best describe the fundamental laws is called the Standard Model of particle physics (SM). The last missing part of the SM, the *Higgs-boson*, has been discovered in 2012 [2, 3] at the LHC by the ATLAS and CMS collaborations in a world-wide effort and the contributions of thousands of scientists and engineers. Though this discovery constituted to the successful history of the SM, many questions about the fundamental nature remain unanswered. The SM is not able to explain all observations, e g. the strong hints for the existence of *dark matter* and *dark energy.* Therefore, theories beyond the Standard Model exist that introduce the existence of new particles with high masses. The LHC with its high centre-of-mass energy and luminosity provides the possibility to search for such particles and to perform precision measurements that test SM predictions.

Such a measurement is performed in this thesis in the field of top-quark physics. The top-quark is the heaviest known elementary particle, presumably having the largest coupling to the Higgs-boson that provides mass to all fundamental particles. The large mass of the top-quark with $m_t = 173.18 \pm 0.94 \,\text{GeV}/c^2$ as current world average [4] implies a life-time that is too short for the top-quark to develop bound states with other quarks, thus to *hadronise.* This property provides an excellent environment for SM tests. One of these tests is to determine the structure of the Wtb vertex in top-quark decays. In this thesis, the helicity of the W-boson from the top-quark is measured to do so. So-called *W-helicity fractions* are determined and compared to the SM prediction. Deviations from the SM prediction would hint to unknown new physics that cannot be explained within the SM. The fundamental aspects and results of the analysis towards the measurement of the W-helicity in top-quark decays with the ATLAS experiment will be discussed in this thesis.

The basic principles of the Standard Model are introduced in Chapter 2. This is followed by an introduction to top-quark physics in general and the properties of the Wtb vertex in particular in Chapter 3. The experimental setup including a short description of the LHC and a more detailed description of the ATLAS detector is given in Chapter 4. After particles are measured in the detector they need to fulfil criteria to be classified as certain objects, which will be explained in Chapter 5. The principles of Monte Carlo simulation on which the measurement relies are briefly introduced in Chapter 6. The measurement is performed in the ℓ+jets channel of top$-$anti-top-quark events. The event selection of this particular channel is described in

Chapter 7 along with the data sample. Results concerning event yields and kinematic distributions are presented here as well. The analysis strategy followed in this thesis including the event reconstruction with the help of a kinematic likelihood fitter, the statistical tools to extract the W-helicity fractions from data and the evaluation of systematic uncertainties of the measurement is explained in Chapter 8. The measurement of the W-helicity in top-quark decays is a precision measurement for which the evaluation of uncertainties is emphasised and of particular importance. Ways to reduce uncertainties of the measurement are shown in Chapter 9. The final results of the analysis including the full systematic evaluation are presented in Chapter 10. A summary and outlook is given in Chapter 11.

2. The Standard Model of Particle Physics

This chapter introduces the theoretical basics of the Standard Model of Particle Physics (SM). The SM is up to now the model known to describe experimental data best and no deviations from SM predictions have been found. The fundamental particles and forces that are described by the SM are shortly presented here as well as the mechanism of electroweak symmetry breaking that predicts a scalar boson in the SM, the so-called *Higgs-boson*. Up to last year, this particle represented the last missing piece of the SM. But with the discovery of the Higgs-boson in 2012 [2, 3], it seems that also this missing piece has been revealed to exist in nature. Although no deviations from SM predictions have been found so far, studies to test the SM still continue as the SM does not satisfactorily describe all observations and leaves some open questions, that will be shortly discussed in Sect. 2.4.

The SM is a theory that has been developed by various physicists mainly in the 1960s and 1970s [5–9]. The SM describes the elementary particles[a] and the interactions between them. The SM does not predict the fundamental particles but it rather incorporates the particles we know up to now in a common theoretical framework. The particle content of the SM is introduced in Sect. 2.1, the three fundamental forces described within the SM excluding gravity are introduced in Sect. 2.2.

2.1. Particle Content

The elementary particles in the SM are grouped in *fermions* with spin $s = 1/2$ and *bosons* with integer spins. The fermions are the matter particles and the spin-1 bosons are the so-called *gauge bosons* that mediate the three forces (see next Sect. 2.2). The fermions are arranged in three generations[b] and are divided in *leptons* and *quarks*. The visible matter is made up of particles belonging to the first generation: the *up* (u) and *down* (d) quarks form protons and neutrons, the constituents of atomic nuclei. The charged electrons e^- together with the nuclei form atoms. The second and third generations of quarks and leptons can only be produced in collision experiments and are not stable. They differ from the first generation by increasing masses of the particles. In total there are six different *flavours* of quarks: $up, down, charm, strange, top$ and *bottom*[c]. The electron is accompanied by an electrically neutral neutrino, the electron-neutrino ν_e, which is the weak isospin partner of the electron (see Sect. 2.2). The muon (μ) and muon-neutrino (ν_μ), the tau (τ) and the tau-neutrino (ν_τ) make up the second and third lepton generation, respectively, and only differ from the first generation by increasing mass of the charged leptons. The leptons carry *lepton numbers* L_e, L_μ and L_τ according to their lepton family. The fundamental fermions together with their charge and measured masses are given in Table 2.1. All particles are accompanied by their anti-particles which have the same spin and masses but opposite electric charges (except for the neutrinos) and are denoted by a bar, e. g.: the $\bar{t}$ is the anti-particle of the top-quark. The generations of fermions follow a striking mass

---

[a] Point-like particles with no further substructure.
[b] also called 'families'
[c] Symbols are given by u, d, c, s, t and b, respectively

	Quarks			Leptons		
Generation	Symbol	$Q[e]$	Mass [MeV/c^2]	Symbol	$Q\,[e]$	Mass [MeV/c^2]
1	u	$+\frac{2}{3}$	1.8 to 3.0	ν_e	0	$< 2.2 \cdot 10^{-6}$
	d	$-\frac{1}{3}$	4.5 to 5.3	e^-	-1	0.511
2	c	$+\frac{2}{3}$	$(1.275 \pm 0.025) \cdot 10^3$	ν_μ	0	< 0.170
	s	$-\frac{1}{3}$	95 ± 5	μ^-	-1	106
3	t	$+\frac{2}{3}$	$(173.18 \pm 0.94) \cdot 10^3$	ν_τ	0	< 18.2
	b	$-\frac{1}{3}$	$(4.18 \pm 0.03) \cdot 10^3$	τ	-1	1777

Table 2.1.: The generations of quarks and leptons, their charge Q in units of e and their measured masses [10]. Upper limits on neutrino masses are given at 95% CL from [11, 12] (ν_e), [13] (ν_μ) and [14] (ν_τ).

hierarchy. The masses span a range of about 9 orders of magnitude, where the top-quark is by far the heaviest fermion. In the SM, neutrinos are considered to be massless. But experimental findings of neutrino oscillations require neutrinos to have masses (see e. g. [15–19]). In Table 2.1, upper limits on the neutrino masses from direct mass measurements are given.

Besides the described fermions, the SM also incorporates force carriers, the gauge bosons γ, the photon, g, the gluons and $W^\pm$, Z^0, the weak bosons that mediate the weak force. These bosons mediate different forces and will be further described in the next section.

2.2. Fundamental Interactions

The three fundamental forces electromagnetic, weak and strong force are described within the SM. They are mediated by gauge bosons. The gauge bosons gather their name from the basic principle through which they emerge in the theory: the requirement of the Lagrangian $\mathscr{L}$, that mathematically describes the particles and interactions, to be invariant under *local* gauge transformations. This requirement can only be met if additional terms are introduced into $\mathscr{L}$ that contain the fields of the gauge bosons. All particles and mediators are described by quantised fields in the framework of quantum field theory. The quantisation of the gravitational field has not been successfully performed up to now. But due to the weakness of the gravitational force, it does not play a role in high energy collider physics and will not be further discussed here.

The electromagnetic force is mediated by massless photons, the weak force by the massive Z^0 and $W^\pm$-bosons and the strong force by eight massless gluons. All particles participate in the weak interaction, only charged particles participate in the electromagnetic interaction and only those particles that carry a so-called *colour-charge* participate in the strong interaction, namely quarks and gluons. The three interactions are summarised in Table 2.2. A more thorough description of the three forces is given in the following.

2.2.1. The Strong Interaction

The gauge group that characterises the strong interaction is the $SU(3)_C$ group, where C stands for colour, to which the eight mediators, the gluons g, couple. Accordingly, the theoretical framework that describes the strong interaction is called quantum chromo dynamics, QCD. The

interaction	couples to	mediator	mass $[\text{GeV}/c^2]$	relative strength
strong	colour	8 gluons (g)	0	1
electromagnetic	electric charge	photon (γ)	0	10^{-2}
weak	weak charge	$W^\pm$, Z^0	$\approx 10^2$	10^{-5}

Table 2.2.: The three interactions with their gauge bosons described in the SM [10]. The relative strength of the interaction is given by the respective couplings, $\alpha_s, \alpha_{\text{em}}$ and G_F (not pure coupling, modified by mediator mass!).

colour charge is an additional quantum number[d] that only quarks and gluons carry. Quarks can carry the colours red, green or blue, anti-quarks carry anti-red, anti-green or anti-blue. Gluons carry both colour and anti-colour. Quarks can only be observed in so-called *hadrons* which are bound states, either mesons ($q\bar{q}$) or baryons (qqq), and not as free particles. This is due to the non-Abelian character of the $SU(3)_C$ group. The generators of the $SU(3)_C$ group $t^a = \frac{1}{2}\lambda^a$, where λ^a are the eight 3×3 *Gell-Mann-matrices*, do not commute: $[t^a, t^b] = if^{abc}t^c$. f^{abc} are the structure constants of QCD. The impact of the non-Abelian gauge group is visible by looking at the classical[e] QCD Lagrangian:

$$\mathscr{L}_{\text{QCD}} = -\frac{1}{4}F_a^{\mu\nu}F_{\mu\nu}^a + \sum_q \bar{\psi}_{q,i}(i\gamma^\mu\partial_\mu\delta_{ij} - g_s(t^c A_\mu^c)_{ij} - m\delta_{ij})\psi_{q,j} \tag{2.1}$$

with $\qquad F_{\mu\nu}^a = \partial_\mu A_\nu^a - \partial_\nu A_\mu^a - g_s f^{abc}A_\mu^b A_\nu^c. \tag{2.2}$

The gluon fields are denoted by A_μ^a, the spinor $\psi_{q,i}$ represents the field of the quark q (the sum in Eq. 2.1 is over all quark flavours) with the colour i. This Lagrangian is invariant under the gauge transformation

$$\psi_i \rightarrow \exp\left[i(t^a\theta^a(x))_{ij}\right]\psi_j,$$

with $\theta(x)$ being a locally dependent phase factor. The term proportional to $g_s\bar{\psi}_{q,i}(t^c A_\mu^c)_{ij}\psi_{q,j}$ in Eq. 2.1 represents the quark-gluon interaction. The last term in Eq. 2.2 stems from the commutator $[t^a, t^b]$ and does not vanish; g_s is related to the strong coupling constant α_s via $g_s = \sqrt{4\pi\alpha_s}$. Inserting Eq. 2.2 into Eq. 2.1 one finds terms that are proportional to $(\partial_\mu A_\nu^a - \partial_\nu A_\mu^a)A_\mu^b A_\nu^c$ and $A_\mu^a A_\nu^b A_c^\mu A_d^\nu$ that represent three gluon and four gluon interactions, respectively. This means that gluons couple to themselves: the consequence is that the potential between two quarks increases with increasing distance, due to the effect of anti-screening[f]. When separating two quarks from each other, the energy in the field between them will at one point be large enough to create a new quark−anti-quark pair. Instead of separating two quarks from each other, another quark pair will be created which makes it impossible to observe single quarks. Only colour singlet states such as baryons and mesons can be observed in nature. This is what is called *quark confinement*. It requires the strong coupling to increase with decreasing energy, thus increasing distance. In renormalisable gauge theories, the couplings are energy dependent due to vacuum polarization

---

[d] The colour charge quantum number was initially introduced to explain the existence of qqq bound states with same quark flavours and spins to avoid the violation of Pauli's principle.

[e] Here, only the classical QCD Lagrangian is shown. A 'gauge fixing' part (to ensure invertibility of the gluon propagator) and a so-called 'ghost term' (to cancel unphysical polarisation states of the gluon) are left away, since this is a short introduction to QCD and the terms are not needed for the general understanding.

[f] The self-coupling terms of gluons lead to a cloud of gluons that carry colour charge around a single quark which increases the colour charge with increasing distance to the single quark.

effects. The quantities, such as couplings are parameterised depending on bare couplings and a starting energy scale μ_0^2. The bare quantities have to be independent of the energy μ^2 which leads to so-called *renormalization group equations* (RGE). The solution of the RGE yields in the case of the strong coupling α_s:

$$\alpha_s(\mu^2) = \frac{\alpha_s(\mu_0^2)}{1 + \frac{\alpha_s(\mu_0^2)}{4\pi}\beta_0 \ln\left(\frac{\mu^2}{\mu_0^2}\right)} \quad \text{with} \quad \beta_0 = 11 - \frac{2}{3}N_f \quad \text{at the one-loop level.} \tag{2.3}$$

N_f is the number of quark flavours that are relevant at a scale μ^2. For six quark flavours β_0 is always positive and α_s diverges to high values for low energies. At high energies, α_s is small and therefore one speaks of *asymptotic freedom* of quarks at small distances. The scale at which the divergence occurs (the denominator becomes zero) is often denoted as Λ_{QCD}. Below this scale, perturbation theory in α_s is no longer possible. The coupling can be rewritten in the form:

$$\alpha_s(\mu^2) = \frac{4\pi}{\beta_0 \ln\left(\frac{\mu^2}{\Lambda_{\mathrm{QCD}}^2}\right)}. \tag{2.4}$$

From measurements of $\alpha_s(m_Z^2)$ with m_Z being the Z-boson mass it is deduced that $\Lambda_{\mathrm{QCD}} \sim$ 200 MeV [10]. Knowledge of this behaviour of α_s is important to understand and model hadron collider phenomenology.

2.2.2. The Electroweak Interaction

In this chapter, the electromagnetic and weak force are described. A common theoretical framework that describes both forces was introduced by Glashow, Weinberg and Salam [6, 8, 20]. The electromagnetic and weak interaction unify to the *electroweak* interaction, mediated by the massless photon γ, two charged massive $W^\pm$-bosons and an electrically neutral, massive Z^0-boson. While the photon only couples to electric charge, the massive weak bosons couple to the *weak isospin T*. Only left-handed particles carry weak isospin. Therefore, left-handed doublets of fermions participate in the weak interaction, while right-handed particles transform as singlets under the corresponding symmetry transformation, thus they do not take part in the weak interaction. The corresponding gauge group of the electroweak interaction is $SU(2)_L \otimes U(1)_Y$. The group $SU(2)_L$ describes the weak interaction where the subscript L indicates the coupling to left-handed particles. The group $U(1)_Y$ describes the electromagnetic part of the interaction where the subscript Y refers to the so-called *hypercharge* that is defined as: $Y = 2(Q - T_3)$ with T_3 being the third component of the weak isospin. The fermion doublets and singlets together with their isospin T and third component T_3 and the hypercharge are listed in Table 2.3. No right-handed neutrinos are listed as in the SM they are *a priori* considered to be massless and the helicity measurement performed by Goldhaber et al. [21] implies that neutrinos are only left-handed (when they are produced in a weak interaction). The doublets consist of so-called flavour eigenstates, eigenstates of the weak interaction. Only in charged $W^\pm$-boson exchange it is possible to change the flavour of a quark. This is because mass eigenstates are not equal to flavour eigenstates but mixings of these. Conventionally, the mass eigenstates and flavour eigenstates of the up-type quarks (u, c and t) are set equal and the mixing is ascribed only to the down-type quarks (d, s and b). Therefore, in Table 2.3 the flavour eigenstates are denoted

	fermion multiplets			T	T_3	Y
leptons	$\begin{pmatrix} \nu_e \\ e^- \end{pmatrix}_L$	$\begin{pmatrix} \nu_\mu \\ \mu^- \end{pmatrix}_L$	$\begin{pmatrix} \nu_\tau \\ \tau^- \end{pmatrix}_L$	$1/2$	$+1/2$ $-1/2$	-1
	e_R^-	μ_R^-	τ_R^-	0	0	-2
quarks	$\begin{pmatrix} u \\ d' \end{pmatrix}_L$	$\begin{pmatrix} c \\ s' \end{pmatrix}_L$	$\begin{pmatrix} t \\ b' \end{pmatrix}_L$	$1/2$	$+1/2$ $-1/2$	$+1/3$
	u_R	c_R	t_R	0	0	$+4/3$
	d_R	s_R	b_R	0	0	$-2/3$

Table 2.3.: Fermions and their corresponding weak isospin T with third component T_3 and hypercharge Y [10].

as d', s' and b' and are related to the mass eigenstates via the CKM-Matrix V_{CKM}:

$$\begin{pmatrix} d' \\ s' \\ b' \end{pmatrix} = \begin{pmatrix} V_{ud} & V_{us} & V_{ub} \\ V_{cd} & V_{cs} & V_{cb} \\ V_{td} & V_{ts} & V_{tb} \end{pmatrix} \begin{pmatrix} d \\ s \\ b \end{pmatrix} = V_{CKM} \begin{pmatrix} d \\ s \\ b \end{pmatrix}. \tag{2.5}$$

This formalism has been developed by Cabibbo and extended by Kobayashi and Maskawa in 1973 [22, 23]. The matrix V_{CKM} is characterised by three mixing angles and one complex phase that leads to the violation of the CP-symmetry[g]. The matrix is non-diagonal which allows transitions between different generations via the weak interaction. The diagonal elements are nevertheless close to 1, transitions between different generations are possible but suppressed, especially between first and third generation particles. An equivalent formalism to the CKM-Matrix can be introduced in the lepton sector. This has been done by Pontecorvo, Maki, Nakagawa and Sakata who included the so-called PMNS-Matrix into the theory as an analogue to the CKM-Matrix that can describe transitions between different neutrino flavours[h] [24–26].

The generators of the non-Abelian $SU(2)_L$ group are the Pauli matrices τ_i, the generator of the $U(1)_Y$ Abelian gauge group is the hypercharge Y. A $SU(2)_L \otimes U(1)_Y$ transformation is of the form

$$\psi_L \rightarrow \exp\left[i\frac{1}{2}g\boldsymbol{\alpha}(x) \cdot \boldsymbol{\tau} + ig'\beta(x)Y\right]\psi_L \qquad \text{and} \qquad \psi_R \rightarrow \exp\left[ig'\beta(x)Y\right]\psi_R \tag{2.6}$$

with arbitrary phases $\boldsymbol{\alpha}(x)$ and $\beta(x)$. The vector $\boldsymbol{\tau}$ consists of the Pauli matrices τ_i and ψ_L and ψ_R are left-handed and right-handed spinors. The parameters g and g' are the couplings of $SU(2)_L$ and $U(1)_Y$, respectively. For the electroweak Lagrangian $\mathscr{L}_{\text{ew}}$ to be invariant under the transformation in Eq. 2.6, an isotriplet field $\boldsymbol{W}_\mu = (W_{1\mu}, W_{2,\mu}, W_{3\mu})$ and a singlet field B_μ

---

[g] C is the charge conjugation operator and P is the parity operator. Both symmetries are maximally violated in the weak interaction. The combination of both transformations is mildly violated in the SM.

[h] This PMNS-Matrix is not part of the SM, it only becomes relevant if neutrinos have non-zero masses.

have to be added. The corresponding Lagrangian takes the form:

$$
\begin{aligned}
\mathscr{L}_{\mathrm{ew}} = &- \frac{1}{4} \boldsymbol{W}_{\mu\nu} \boldsymbol{W}^{\mu\nu} - \frac{1}{4} B_{\mu\nu} B^{\mu\nu} \\
&+ i \bar{L} \gamma^{\mu} \left[\partial_{\mu} + i \frac{g}{2} \boldsymbol{W}_{\mu} \cdot \boldsymbol{\tau} + i \frac{g'}{2} Y B_{\mu} \right] L + i \bar{R} \gamma^{\mu} \left[\partial_{\mu} + i \frac{g'}{2} Y B_{\mu} \right] R.
\end{aligned}
\tag{2.7}
$$

The tensor $\boldsymbol{W}_{\mu\nu}$ is given by $\boldsymbol{W}_{\mu\nu} = \partial_{\mu} \boldsymbol{W}_{\nu} - \partial_{\nu} \boldsymbol{W}_{\mu} - g \cdot \boldsymbol{W}_{\mu} \times \boldsymbol{W}_{\nu}$ and $B_{\mu\nu}$ is $B_{\mu\nu} = \partial_{\mu} B_{\nu} - \partial_{\nu} B_{\mu}$. L and R denote left-handed doublets and right-handed singlets, respectively (see Table 2.3). The first two terms in Eq. 2.7 are kinetic energy terms of the gauge fields, the other terms represent interaction terms of particles with the gauge fields.

After *electroweak symmetry breaking* the fields mix to form the physical $\gamma, W^{\pm}$ and Z^0-bosons. The neutral bosons, represented as fields A_{μ} (photon) and Z_{μ} (Z^0-boson), are linear combinations of $W_{3\mu}$ and B_{μ}:

$$
\begin{pmatrix} A_{\mu} \\ Z_{\mu} \end{pmatrix} = \begin{pmatrix} \cos\theta_W & \sin\theta_W \\ -\sin\theta_W & \cos\theta_W \end{pmatrix} \begin{pmatrix} B_{\mu} \\ W_{3\mu} \end{pmatrix}.
$$

The weak mixing angle or also called Weinberg angle θ_W relates the two couplings g and g':

$$
\sin\theta_W = \frac{g'}{\sqrt{g^2 + g'^2}} \qquad \text{or} \qquad \tan\theta_W = \frac{g'}{g}.
\tag{2.8}
$$

The charged W-bosons are linear combinations of the first and second isotriplet field components:

$$
W_{\mu}^{\pm} = \frac{1}{\sqrt{2}} \left(W_{1\mu} \mp i W_{2\mu} \right).
$$

In Eq. 2.7, there are no mass terms for the gauge bosons as they would break the invariance under local gauge transformations. This is in conflict with the experimental measurements: the weak bosons are massive particles with masses of $m_W = (80.385 \pm 0.015)$ GeV/c^2 and $m_Z = (91.1876 \pm 0.0021)$ GeV/c^2 [10]. A solution to this problem is given by the mechanism of electroweak symmetry breaking.

2.3. Electroweak Symmetry Breaking

To ensure invariance of the Lagrangian under gauge transformation including mass terms for the massive gauge bosons, six authors proposed the mechanism of spontaneous symmetry breaking [27–29]. This mechanism is named after Peter Higgs the *Higgs-mechanism*. The basic idea is to add a potential to the Lagrangian of the following form:

$$
V(\phi) = \mu^2 (\phi^{\dagger} \phi) + \lambda (\phi^{\dagger} \phi)^2.
\tag{2.9}
$$

The field ϕ is a complex scalar $SU(2)$-doublet field that can be written as:

$$
\phi = \frac{1}{\sqrt{2}} \begin{pmatrix} \phi_1 + i\phi_2 \\ \phi_3 + i\phi_4 \end{pmatrix}.
\tag{2.10}
$$

The potential in Eq. 2.9 exhibits a rotational symmetry around $\phi = 0$. If the parameters are chosen as $\mu^2 < 0$ and $\lambda > 0$, then the potential has the form that is sketched in Fig. 2.1. This

potential is still symmetric around $\phi = 0$, but special is that the minima of the potential lie on a circle with radius $v = \sqrt{\dfrac{-\mu^2}{2\lambda}}$ around the symmetry axis. v is called the vacuum expectation value (VEV) and is non-zero. A theory always has to be developed around the ground state of a system. In this case the ground state is degenerated, choosing a particular ground state and developing around this state spontaneously breaks the rotational symmetry of the potential $V(\phi)$. Choosing a ground state ϕ_0 with small perturbations $h(x)$ (real scalar field) around it is
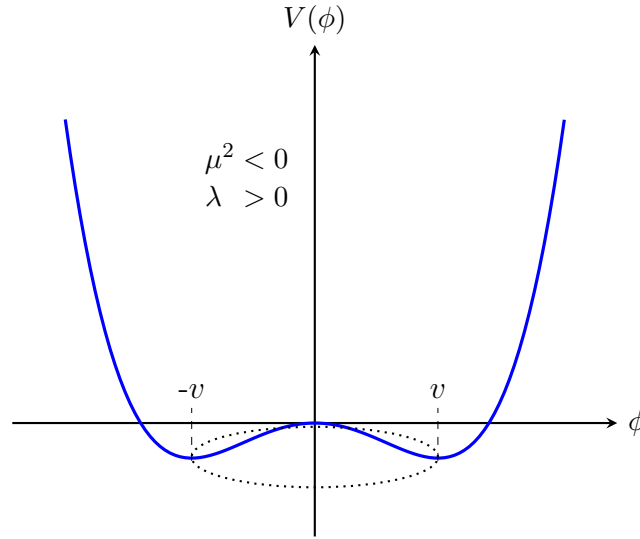

Figure 2.1.: A 2-dimensional sketch of the potential $V(\phi)$ for $\mu^2 < 0$ and $\lambda > 0$. The minima are given by $-v$ and v. Extending to three dimensions means to rotate the potential around the y-axis, indicated by the ellipse at the bottom.

conveniently written as:

$$\phi_0 = \frac{1}{\sqrt{2}} \begin{pmatrix} 0 \\ v + h(x) \end{pmatrix}. \tag{2.11}$$

Adding the potential $V(\phi)$ and a term of the form $(D^\mu \phi)^\dagger (D_\mu \phi)$ with the covariant derivative $D_\mu = \partial_\mu + i\frac{g}{2}\boldsymbol{W}_\mu \cdot \boldsymbol{\tau} + i\frac{g'}{2}B_\mu Y$ and substituting ϕ for ϕ_0 yields the desired additional mass terms in the Lagrangian:

$$\mathscr{L}_{\text{mass}} = -\lambda v^2 h^2 + \frac{1}{4}g^2 v^2 W_\mu^+ W^{-\mu} + \frac{1}{8}(g^2 + g'^2)v^2 Z_\mu Z^\mu. \tag{2.12}$$

The excitation of the Higgs-field $h(x)$ gives the scalar Higgs-boson with the mass $m_h = \sqrt{2\lambda}v$. The interaction of the weak bosons with the Higgs-field generated the mass terms $m_W = \frac{1}{2}vg$ and $m_Z = \frac{1}{2}v(g^2 + g'^2)$. The photon remains massless. Inserting the relation in Eq. 2.8 yields:

$$\frac{m_W}{m_Z} = \cos\theta_W,$$

which is consistent with the Glashow-Weinberg-Salam-theory. The mass of the Higgs-boson could not be predicted due to the unknown parameter λ. After the discovery in 2012, the most recent measurements of the Higgs-mass yield: $m_h = 125.5 \pm 0.2\,(\text{stat})\,^{+0.5}_{-0.6}\,(\text{syst})\,\text{GeV}/c^2$

(ATLAS [30]) and $m_h = 125.5 \pm 0.3\,\text{(stat)} \pm 0.3\,\text{(syst)}\,\text{GeV}/c^2$ (CMS [31]).

Mass terms for fermions can be created by allowing a *Yukawa*-coupling of the Higgs-field to the fermions. Thereby further coupling constants g_f have to be introduced. The masses of the fermions are then proportional to g_f:

$$m_f = \frac{1}{\sqrt{2}} g_f \cdot v.$$

Thus, the masses for fermions cannot be predicted but have to be measured in experiments as the coupling g_f is unknown.

Altogether, the SM incorporates the mechanism of electroweak symmetry breaking producing a Higgs-boson and the three above introduced forces are described by the $SU(3)_C \otimes SU(2)_L \otimes U(1)_Y$ symmetry groups.

2.4. Open Questions in the SM

The SM is a successful theory that could not be disproven in any experimental measurement up to now. Nevertheless, it does not include gravity. Moreover, measurements of the cosmic microwave background performed by WMAP and PLANCK indicate that the SM only describes about 5% of the content of our universe, the visible matter [32–34]. The rest is made of *dark matter* and *dark energy*. The SM provides no answer to the question of what these components are made of. It also has to be extended to include neutrino masses: oscillation measurements of neutrino flavours require neutrinos to have non-zero masses. Including neutrino mass terms is not straight-forward: the question that also arises is of which nature neutrinos are, are they Dirac- or Majorana-particles [35]? Depending on the answer, neutrino mass terms are different. Another problem arises if we consider the huge matter-antimatter asymmetry in our universe: the CP-violation incorporated in the SM via the CKM-mechanism cannot account for the observed matter-antimatter asymmetry. Therefore, one seeks for additional sources of CP-violation, but not successfully up to now.

On the theoretical side, the *hierarchy problem*, or also called *fine-tuning* problem emerges: the fact that the Higgs-boson as a scalar particle receives corrections to its mass via loop contributions of fermions that are 17 orders of magnitude higher than the Higgs-mass itself. This is considered to be *unnatural* and requires a fine-tuning. A solution to this problem is e. g. provided by the model of *Supersymmetry* [36, 37].

Furthermore, the SM has many free parameters, especially all particle masses that cannot be predicted but have to be measured by experiments. These parameters remain arbitrary and yet, changes of these would have dramatic influences on our world (see e. g. [38]). The origin of the generations of fermions and gauge symmetries is not explained, the three forces do not unify (as anticipated by Big Bang models). The latter problem can be solved by other theories, but there is no theory known, to satisfactorily answer the former questions.

All these short-comings motivate to further test the SM and search for physics beyond the SM (BSM). For such kind of studies the field of top-quark physics provides a unique environment. The physics of the top-quark and especially the Wtb vertex that is probed in a W-helicity measurement are introduced in the following chapter.

3. The Top-Quark

With the discovery of the top-quark in 1995 at the TEVATRON [39, 40], the weak isospin partner of the b-quark was found that completes the quark sector in the SM. Before the direct discovery of the top-quark, precision measurements of electroweak parameters, such as the masses of the weak Z- and $W^{\pm}$-bosons, were used to predict the mass of the top-quark as quantum loop corrections containing top-quarks influence these parameters (e. g. [41]). Eventually, the top-quark was discovered where it was expected from these indirect measurements of the top-quark mass. This mass is what makes the top-quark so special: with a mass of $m_t = 173.18 \pm 0.56\,(\text{stat}) \pm 0.75\,(\text{syst})\,\text{GeV}/c^2$ [4] (current world average), the top-quark is the heaviest known elementary particle. This large mass implies a life-time of the top-quark of about $\tau \sim 5 \cdot 10^{-25}$ s ($\tau \propto m_t^{-3}$) which is smaller than the time needed to form bound states with other quarks, which is of the order of 10^{-23} s ($\sim \Lambda_{\text{QCD}}^{-1}$) [10, 42]. The fact that the top-quark decays before it hadronises provides an excellent test ground for the SM and BSM theories: the spin information of the top-quark is directly transferred to the decay products without depolarisation by chromodynamic effects. With its high mass, the top-quark Yukawa coupling to the Higgs-boson is predicted to be of the order of unity. It is therefore believed that the top-quark might play an important role in electroweak symmetry breaking which is interesting for BSM searches, where the top coupling to new particles might be enhanced.

3.1. Top-Quark Production

At hadron colliders, top-quarks are mainly produced in pairs via the strong interaction. The leading order Feynman diagrams of top-quark pair production are depicted in Fig. 3.1. The process in Fig. 3.1(a) is initiated by quark−anti-quark annihilation ($q\bar{q}$-annihilation). The diagrams (b-d) show the production via gluon-gluon fusion (gg-fusion). The dominance of a process depends on the collided hadrons and the centre-of-mass energy $\sqrt{s}$ of the collider.

At hadron colliders, protons are brought to collision with protons or anti-protons. Those are composite objects. Thus, the actual process in a collision is initiated by the constituents of these hadrons, namely quarks and gluons the so-called *partons*. Let the beam momenta of the (anti-)proton beams be P_1 and P_2. Then the centre-of-mass energy of a collider is defined as $s = (P_1 + P_2)^2$. In fact, the partons in the initial states of the diagrams in Fig. 3.1 carry the momentum fractions x_1 and x_2 of the incoming hadrons. The actual centre-of-mass energy of the colliding partons is $\hat{s}$, where $\hat{s} = x_1 x_2 s$. The situation is depicted in Fig. 3.2. The cross-section of the hard-scattering process is denoted by $\hat{\sigma}$. The hadrons are indicated by the three parallel lines. The probability of a parton to carry a certain momentum fraction x of the (anti-)proton is described by the parton density functions (PDFs). In Fig. 3.2, $f(x_1, Q^2)$ and $g(x_2, Q^2)$ give the probabilities to find a parton with a certain momentum fraction at a scale Q^2 for the two incoming hadrons. At the LHC, g and f are equal, corresponding to the two protons that are collided. Making use of the factorisation theorem, the production cross-section of $t\bar{t}$ pairs in a
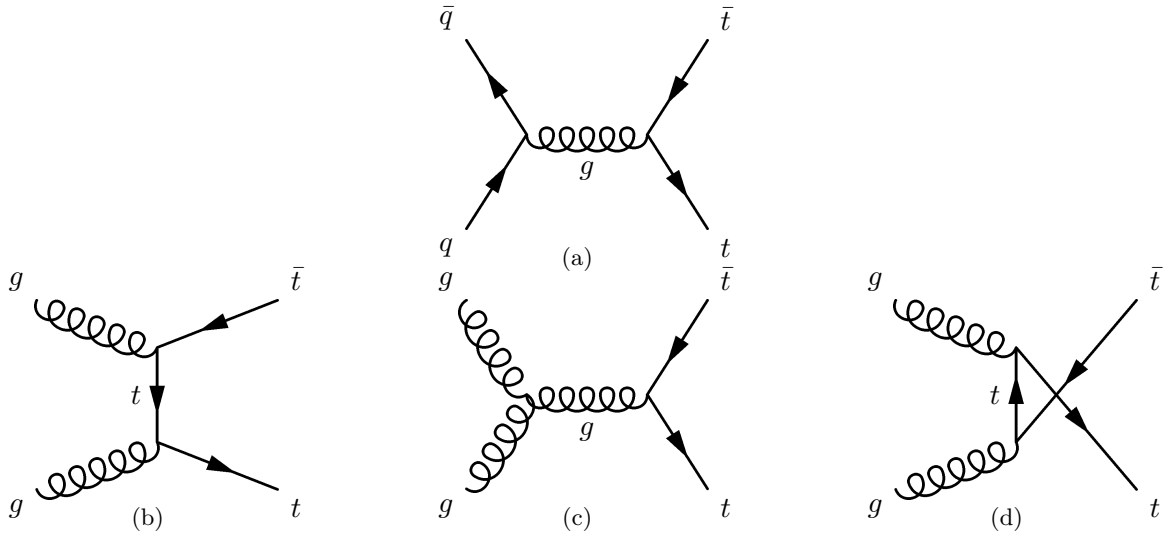
Figure 3.1.: Leading order Feynman diagrams of top-quark pair production in *pp* collisions via $q\bar{q}$-annihilation (a) and *gg*-fusion (b, c, d).

hadron collision can be written as:

$$\sigma_{AB \to t\bar{t}}(x_1, x_2, Q^2, \sqrt{s}) = \sum_{a,b} \int dx_1 \int dx_2 f_a(x_1, Q^2) g_b(x_2, Q^2) \hat{\sigma}_{ab \to t\bar{t}}(x_1, x_2, Q^2, \sqrt{s}).$$

The hard process (high energy/momentum regime) is included in $\hat{\sigma}$, the soft processes are included in the PDFs (low energy/momentum regime). *A* and *B* are the colliding hadrons, *a* and *b* are the colliding partons, the scale of the hard process Q^2 is in the case of top-quark pair production: $Q^2 = (2m_t)^2$. In order to produce $t\bar{t}$ pairs $\sqrt{\hat{s}} \geq 2m_t$ has to hold. This means, if $x_1 = x_2 \equiv x$ is assumed, the following minimum of x is needed:
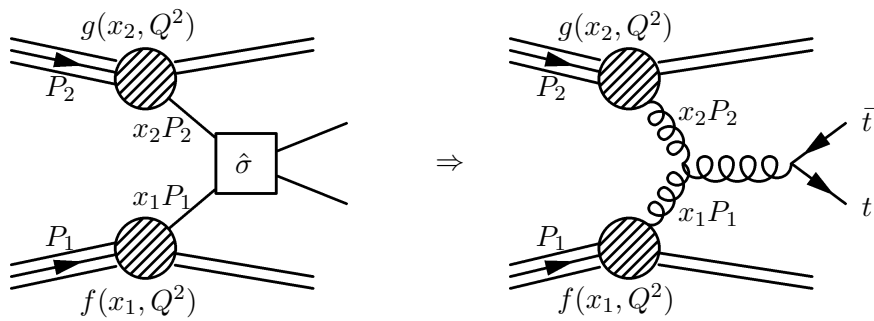
$$x \geq \frac{2m_t}{\sqrt{s}} \ .$$

Figure 3.2.: Production mechanism in hadron-hadron collisions illustrating the factorisation theorem: The cross section of the hard-scattering process is denoted by $\hat{\sigma}$. The soft processes are included in the PDFs *f* and *g* of the hadrons. The right sketch shows an *s*-channel *gg*-fusion to $t\bar{t}$ as an example for the hard process.

Thus, the minimum x depends on the centre-of-mass energy $\sqrt{s}$ of the collider. For the TEVATRON with a maximal $\sqrt{s}$ of 1.96 TeV, x has to take a large value ($x \approx 0.18$), while for the LHC with $\sqrt{s} = 7, 8$ TeV in the 2011 and 2012 runs, respectively, the value of x can be comparatively small ($x \approx 0.05(4)$ for $\sqrt{s} = 7(8)$ TeV). The PDFs at the scale $Q^2 = m_t^2$ are depicted in Fig. 3.3 for the CT10 PDF sets [43], for the different partons. It can be seen that for high x the valence quarks of the proton, up- and down-quark, dominate. For anti-protons, the curves look the same except for reversing the particles with the anti-particles. Thus, at the proton-anti-proton collider TEVATRON, the production of $t\bar{t}$ pairs is dominated by $q\bar{q}$-annihilation. At lower x-values, gluons are dominating in the proton. This leads to gg-fusion being the dominant production mechanism for $t\bar{t}$ pairs at the LHC. Table 3.1 shows the percentage of $q\bar{q}$-annihilation and gg-fusion of the total production cross-section for both colliders.
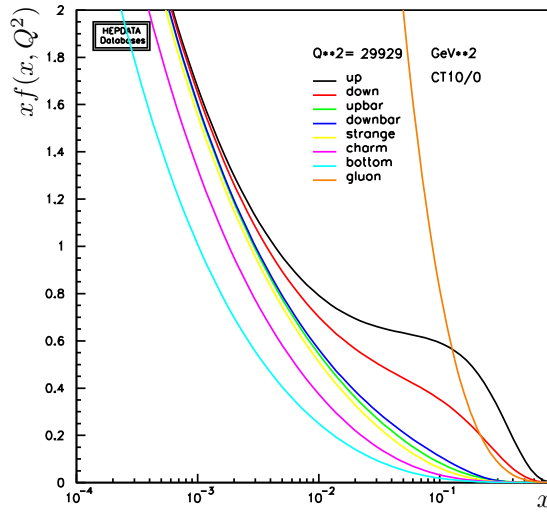

Figure 3.3.: CT10 PDF sets for the scale $Q^2 = m_t^2$. x denotes the momentum fraction while $xf(x, Q^2)$ represents the amount of partons at a certain x. The plot is produced via `HEPDATA` [44].

Process	TEVATRON ($\sqrt{s}$=1.96 TeV)	LHC ($\sqrt{s}$=7 TeV)
$q\bar{q}$-annihilation	85%	20%
gg-fusion	15%	80%

Table 3.1.: Percentage of $q\bar{q}$-annihilation and gg-fusion of the total $t\bar{t}$-pair production at the TEVATRON and the LHC [10, 45, 46].

So far, only the strong production of top-quark pairs has been discussed. Top-quarks can also be produced as single particles via the weak force. Feynman diagrams for the production of single top-quarks at hadron colliders are shown in Fig. 3.4 and 3.5. The s-channel production in association with a b-quark can be initiated via valence quarks at the TEVATRON, while at the LHC this is only possible by involving sea quarks of the proton. For the t-channel production as shown in Fig. 3.4(b), a b-quark is needed in the initial state. This can only originate from gluon splitting into a $b\bar{b}$ pair in the proton. The production of a single top-quark in association with a W-boson (Fig. 3.5) has both initial partons that originate from quark-gluon-splitting in the proton, described by the PDFs. It took about 14 years after the discovery of the top-

quark in strong pair production to observe the single top-quark production process (2009 at the TEVATRON [47, 48]). It is only produced via the weak interaction but it is not the lower cross-section compared to $t\bar{t}$ production[a] that made it so difficult to observe single top-quarks [49].
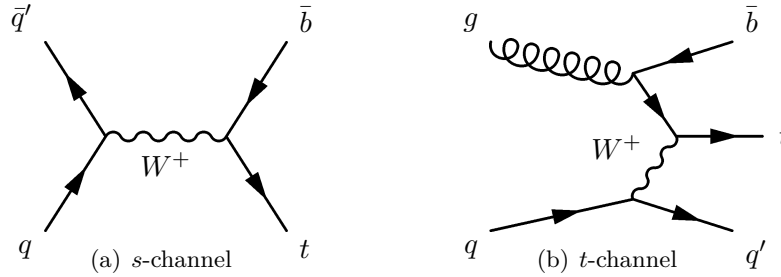

Figure 3.4.: Single top-quark production via *s*- and *t*-channel virtual *W*-boson exchange.
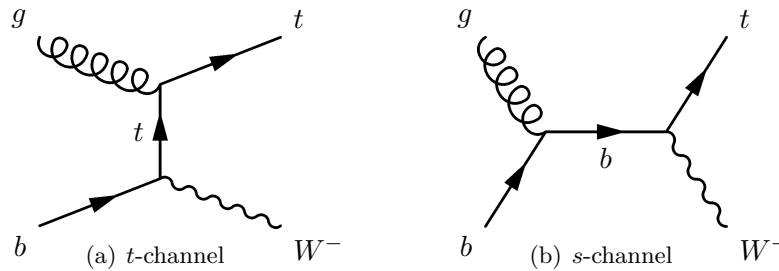

Figure 3.5.: Single top-quark production in association with a *W*-boson.

The main reason is the large background in the single top-quark analysis channels. Other than $t\bar{t}$ production, single top-quark production is less central as it involves rather sea quarks and gluons and as the $\hat{s}$ of the process is half as large and does not require large momentum fractions of the (anti-)proton for the initial partons. Thus, centrality of the event is no discriminator against background[b] events that also tend to be non-central. Also, single top-quark production produces less jets in the final state (compared to $t\bar{t}$, see Sect. 3.2). In this phase space region, one has a lot of background from other processes with much higher production cross-sections[c] (such as W+jets production). Just recently, CMS has announced the observation of the process of single top-quark production in association with a W-boson at $\sqrt{s} = 8$ TeV [51]. Before, only evidence for this process has been reported by the CMS and ATLAS collaborations for the $\sqrt{s} = 7$ TeV analyses [52, 53].

Throughout the rest of the thesis, the focus is on $t\bar{t}$ production only.

3.2. Top-Quark Decay

The top-quark decays via the weak interaction almost exclusively into a *W*-boson and a *b*-quark. Due to the heavy top-quark mass, the *W*-boson is produced as a real particle. The transition rate from a top-quark into a *b*-quark is described by the CKM-Matrix element V_{tb} [22, 23]. Assuming unitarity of the CKM-Matrix, V_{tb} is determined to be $V_{tb} = 0.999146^{+0.000021}_{-0.000046}$ [10]. Thus, two *b*-quarks are expected in the final state of a $t\bar{t}$ decay. The composition of this final

---

[a] In fact, the production cross-sections are of the same order of magnitude.

[b] A process that can be mistaken for a certain signal process because of the similar final state composition is called *background*.

[c] The behaviour of production cross-sections to decrease with the number of jets is known as 'Berends scaling' [50].

state depends on the decay of the two W-bosons. One distinguishes three final states, i. e. three decay channels:

- **fully hadronic:** Both W-bosons decay hadronically, producing in addition four jets from four quarks. With the two b-jets, this final state consists of six high energetic jets. Due to the colour factor, a hadronic decay of W-bosons is more likely than a decay into leptons, thus the fully hadronic channel has the largest branching ratio (BR) of about 46.2% [46]. It also has the poorest signal-to-background ratio caused by multijet production.

- **ℓ+jets:** This channel is also called the semileptonic decay channel where one of the W-bosons decays leptonically and one decays hadronically. A Feynman diagram for this process is shown in Fig. 3.6. The final state contains four jets, a charged lepton ℓ and the corresponding neutrino ν_ℓ which can only be recognised by missing transverse momentum[d], $\not{E}_T$, measured in the detector. Four high energetic jets, one charged lepton and $\not{E}_T$ give this decay channel a distinct signature that makes it distinguishable from background processes. With a BR of about 43.5% it is slightly less likely than the fully hadronic decay and is also called the 'golden channel' [46]. The analysis presented in this report uses this topology for the W-helicity measurement.

- **dileptonic:** Here, both W-bosons decay into leptons and their corresponding neutrinos. Therefore two b-jets, two charged leptons and large $\not{E}_T$ are expected in the final state. The two charged leptons discriminate against background processes. On the other hand, this channel has the lowest BR with about 10.3% [46]. Only one $\not{E}_T$ component can be measured but two neutrinos need to be reconstructed, which leads to an under-determined system of equations when reconstructing the full $t\bar{t}$ event.
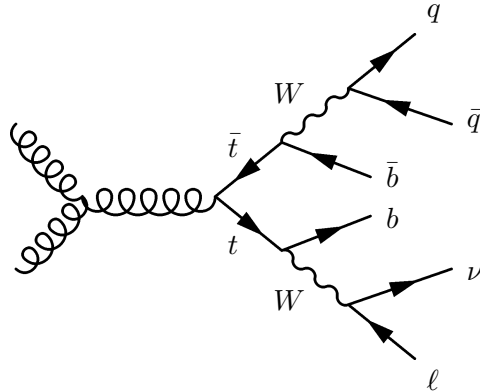
Figure 3.6.: Decay of a $t\bar{t}$ pair in the ℓ+jets channel. In this example, the W^+-boson from the top-quark decay decays into ℓ and ν while the other W-boson decays into two quarks $q\bar{q}'$.

It must be noted that the given BRs do not distinguish leptonic or hadronic decays of a tau-lepton. Its is simply included here as ℓ. In the actual analysis however, the term ℓ refers only to electron and muons (and therefore include leptonically decaying tau-leptons). This denotation is valid from now on.

---

[d] $\not{E}_T$ is recognised if the measured transverse momenta in the detector are not balanced, see Sect. 4.2.1.

3.3. Background Processes

In the following, the focus lies on the ℓ+jets channel and its topology. It has a distinct signature, but there exist other physics processes that have a similar signature and can be selected as a $t\bar{t}$ process. These non-$t\bar{t}$ processes are called background processes. In this analysis, the considered backgrounds are W+jets, Z+jets, diboson production containing two of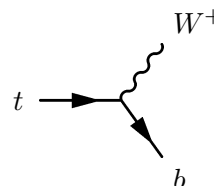 the weak gauge bosons (WW, ZZ and WZ), single top-quark and multijet production. These events can be selected because they contain reconstructed charged leptons, significant $\not{E}_T$ and ≥ 4 jets. Leptons can also be faked by jets (applies for multijet background), or one can lose a lepton because of imperfect reconstruction and acceptance effects. Non-genuine $\not{E}_T$ can be reconstructed due to noisy detector components or dead material in the detector, cosmic ray or beam halo muons that disturb the momentum balance of the measured events. These background contributions can be reduced by requiring certain criteria in the event selection to be fulfilled. The event selection will be discussed in Sect. 7.1. The dominant background after the selection in the ℓ+jets channel is the W+jets background. This background contributes if a W-boson is produced together with more than three jets and has a high production cross-section for low jet multiplicities (see Footnote c on page 14). Like in $t\bar{t}$ events, the charged lepton and genuine $\not{E}_T$ originate from a W-boson decay. Reduction of this background can be achieved by applying cuts on the transverse momenta of the jets and by requiring b-jets in the selection. However, it is important to care about the ratio of signal acceptance to background rejection when performing cuts. One can only gain statistically relevant results if enough signal is left to study.

3.4. The Helicity of the *W*-boson

As mentioned before, the measurement of the W-helicity fractions in top-quark decays allows to test the Wtb-vertex structure. Eq. 3.1 shows the concrete expression in the SM for this particular decay vertex. V_{tb} is the CKM-Matrix element and $\bar{b}$ and t denote spinors of outgoing b-quark and incoming t-quark, respectively. The vector minus axial-vector ($V - A$) character of the weak vertex can be seen explicitly by rearranging the expression for the product of γ^μ and the left-handed projector P_L:

$$\gamma^\mu P_L = \gamma^\mu 1/2(1 - \gamma^5) = 1/2(\gamma^\mu - \gamma^\mu \gamma^5)$$

The vector coupling shows up as γ^μ and the axial-vector coupling as $\gamma^\mu \gamma^5$. This structure implies that the weak interaction only couples to left-handed particles and right-handed anti-particles (due to the emerging left-handed projector P_L).

$$-\frac{ig_W}{\sqrt{2}} \bar{b} \gamma^\mu V_{tb} \frac{1}{2}\left(1 - \gamma^5\right) t W_\mu^- \tag{3.1}$$

This plays an important role for the possible helicity states of the W-boson in the top-quark decay. Top- and bottom-quarks are both fermions and carry spin $s = 1/2$, while the W-boson carries spin $s = 1$. In the rest frame of the top-quark, there are three possible helicity states for the real W-boson, which are depicted in Fig. 3.7. The thin arrows indicate the momentum direction of the W-boson and the b-quark, the thick arrows indicate the spin orientation. In the case of a right-handed W^+-boson, the b-quark has to be a right-handed particle as well. If one

neglects the b-quark mass compared to the top-quark mass, the case of a right-handed, approximately massless b-quark has to be excluded and thus the case of a right-handed W^+-boson has to be excluded. In fact, the b-quark is not a massless particle, so the fraction of events with a
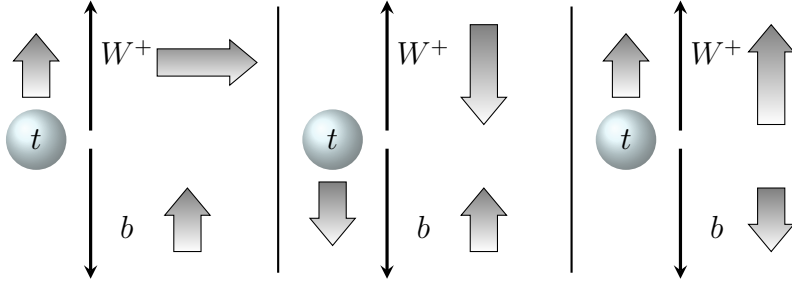

Figure 3.7.: Possible polarisation states of the W^+-boson in the top-quark decay: In the rest frame of the top-quark, the W^+-boson and the b-quark must have opposite momenta which are indicated by the thin arrows. Taking conservation of angular momentum into account results in the three possibilities seen above, where the thick arrows indicate the spin direction: Left: longitudinally polarised, Middle: left-handed and Right: right-handed W^+-boson.

right-handed W^+-boson originating from a top-quark decay is not zero, but suppressed. The fractions for longitudinally polarised, left-handed and right-handed W-bosons are denoted by F_0, F_L and F_R, where the indices $0, L$ and R stand for longitudinal, left-handed and right-handed, respectively. They are defined by the branching ratios:

$$F_0 = \frac{\Gamma(t \to W_0 + b)}{\Gamma}, \quad F_L = \frac{\Gamma(t \to W_L + b)}{\Gamma}, \quad F_R = \frac{\Gamma(t \to W_R + b)}{\Gamma}, \tag{3.2}$$

where Γ is the total decay width of the top-quark and $\Gamma(t \to W_i + b)$ is the partial decay width in a helicity state of $i = 0, L, R$. Accordingly, $\Gamma = \Gamma(t \to W_0 + b) + \Gamma(t \to W_L + b) + \Gamma(t \to W_R + b)$ and therefore $F_0 + F_L + F_R = 1$ applies. Calculations of the helicity fractions where terms of m_b^2/m_t^2 are neglected yield the following expressions [54]:

$$\begin{aligned} F_0 &\approx \frac{2m_W^2}{m_t^2 + 2m_W^2} \simeq 0.7, \\ F_L &\approx \frac{m_t^2}{m_t^2 + 2m_W^2} \simeq 0.3, \\ F_R &= 0 \,. \end{aligned} \tag{3.3}$$

In calculations not neglecting m_b and to orders of $\mathcal{O}(\alpha_s^2)$ (next-to-next-to-leading order, NNLO) the fractions are predicted to be [1]:

$$\begin{aligned} F_0 &= 0.687 \pm 0.005, \\ F_L &= 0.311 \pm 0.005 \\ F_R &= 0.0017 \pm 0.0001. \end{aligned} \tag{3.4}$$

Here, radiative corrections from gluon emissions are driving the plus-rate in F_R (compared to Eq. 3.3), more than the non-zero b-quark mass. The errors on the NNLO calculation originate dominantly from uncertainties on the top-quark mass (F_0 and F_L) and α_s and to a lesser degree

on m_b, the b-quark mass (F_R uncertainty). A precision measurement of the helicity fractions allows to test this SM prediction.

The most general[e] vertex structure of the Wtb vertex is represented by the Lagrangian $\mathscr{L}$ given in Eq. 3.5. P_L and P_R $\left(= \frac{1}{2}(1 \mp \gamma^5)\right)$ are the left-handed and right-handed projectors.

$$\mathscr{L} = -\frac{g_W}{\sqrt{2}}\bar{b}\gamma^\mu(V_L P_L + V_R P_R)tW_\mu^- - \frac{g_W}{\sqrt{2}}\bar{b}\frac{i\sigma^{\mu\nu}q_\nu}{m_W}(g_L P_L + g_R P_R)tW_\mu^- + h.c. \qquad (3.5)$$

V_L and V_R denote vector-like couplings. In the SM, V_R equals zero and V_L is the CKM-Matrix element V_{tb}. There are also tensor couplings, g_R and g_L, that show up in the term with the tensor $\sigma^{\mu\nu}$. The four-momentum q is $q = p_t - p_b$, where p_t and p_b denote the four-momenta of top- and bottom-quark, respectively. Again g_R and g_L are zero in the SM. A measurement of the fractions F_i $(i = 0, L, R)$ allows to constrain these anomalous couplings, V_R, g_R and g_L.

In the previous paragraphs, formulas are shown with respect to the decay of the top-quark. In the actual analysis, $t\bar{t}$ events are used which decay in the ℓ+jets mode to measure the helicity fractions and one does not distinguish between a W-boson coming from a top-quark or an anti-top-quark decay. If the possibilities for the polarisation of a W^--boson in an anti-top decay are considered, the picture of Fig. 3.7 reverses: we expect the fraction of left-handed W^--bosons to be suppressed, this is what CPT invariance implies. However, the terms of a right-handed W-boson as a suppressed case is kept for convenience. As will be discussed next, spin analysers give the same information in top-quark and anti-top-quark decays on the relevant quantities.

3.4.1. Spin Analysers

There are several variables that can be used in order to extract the W-helicity fractions in $t\bar{t}$ events. The most frequently used variable in analyses is the angular variable $\cos\theta^*$, which is also used in the analysis presented here. The angle θ^* is defined as the angle between the down-type fermion from the W-boson decay and the reversed direction of the b-quark in the rest frame of the W-boson. The angle is depicted in Fig. 3.8(a). The down-type fermion is the lepton ℓ [f]. Only the leptonically decaying W-boson is used to reconstruct $\cos\theta^*$, where the identification of the charged lepton as the down-type fermion is easiest. The differential expression for the number of events N with a certain $\cos\theta^*$ is given in Eq. 3.6, where F_0, F_L and F_R come in.

$$\begin{aligned}\frac{1}{N}\frac{\mathrm{d}N}{\mathrm{d}\cos\theta^*} =& \frac{3}{8}(1 - \cos\theta^*)^2 F_L + \frac{3}{4}\sin^2\theta^* F_0 + \frac{3}{8}(1 + \cos\theta^*)^2 F_R \\ =& \omega_- \cdot F_L + \omega_0 \cdot F_0 + \omega_+ \cdot F_R\end{aligned} \qquad (3.6)$$

The functional dependencies of F_0, F_L and F_R on $\cos\theta^*$ are given by the terms ω_0, ω_- and ω_+, respectively. The corresponding distributions for F_0, F_L and F_R are plotted in Fig. 3.8(b). From this plot the discrimination power of $\cos\theta^*$ is obvious, resulting in distinct curves for ω_0, ω_- and ω_+ which correspond to pure helicity states. The SM prediction is shown as the black curve. Considering the anti-top-quark decay, the curves belonging to left-handed and right-handed states are exchanged, this guarantees that we measure the same distribution for both top- and anti-top-quark decays. The angle θ^* can only be measured if the full event is reconstructed, this

---

[e] 'General' means mathematically possible structure without assuming the SM.
[f] In this case, the example of the W^+-boson decay is shown, therefore ℓ has a positive charge. For a W^- decay, the lepton is the negative charged one.
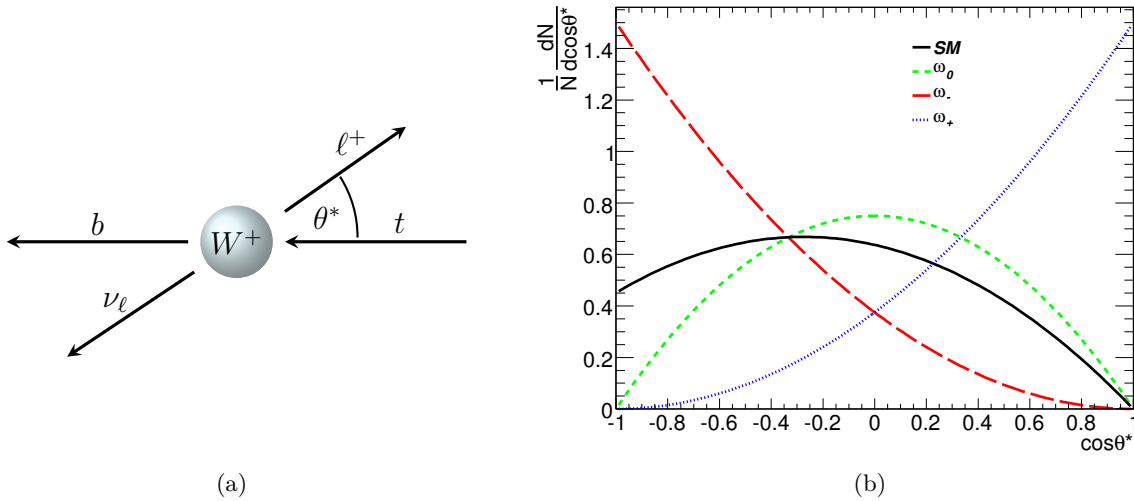
Figure 3.8.: (a): Angular variable θ^* used as spin analyser, description is given in the text. (b): Distributions of ω_0, ω_+ and ω_- as functions of $\cos\theta^*$ corresponding to the longitudinal polarised, right-handed and left-handed states, respectively (see Eq. 3.6). The SM prediction is shown as the black line.

is explained in Sect. 8.1.

A closely related variable to $\cos\theta^*$ is the invariant mass of the down-type lepton ℓ and the b-quark, denoted as $m_{\ell b}$. The squared of $m_{\ell b}$ can be calculated under the assumption of massless ℓ and b as follows:

$$
\begin{aligned}
m_{\ell b}^2 = (p_\ell + p_b)^2 = (E_\ell + E_b)^2 - (\vec{p}_\ell + \vec{p}_b)^2 &\approx 2E_\ell E_b(1 - \cos\theta_{\ell b}) \\
&= 2E_\ell E_b(1 + \cos\theta^*) \\
\Leftrightarrow \quad \cos\theta^* &\approx \frac{m_{\ell b}^2}{2E_\ell E_b} - 1.
\end{aligned}
$$

This variable has the advantage that it does not rely on the reconstruction of the full event, especially not on the reconstructed $\not{E}_T$. This variable has been used in [55].

A third variable that has been used in analyses performed at CDF and DØ at the TEVATRON is the transverse momentum p_T of the lepton [56, 57]. The lepton-p_T spectrum is a kinematic distribution that can be precisely measured and does not require any event reconstruction. The 'hardness'[g] of the p_T spectra differs for the different helicity states. For a right-handed W^+-boson the lepton tends to be emitted in the direction of flight of the W-boson. For a left-handed W^+-boson the lepton is predominantly emitted into the opposite direction of flight of the W-boson. This leads to a harder p_T spectrum coming from a right-handed W-boson than the one from a left-handed W-boson. The spectrum from a longitudinally polarised W-boson is of intermediate hardness and lies somewhere in between the other spectra. The advantage of this variable is the small influence of the jet energy scale (JES) on the spectra, albeit the distinction between the different polarisation states is less strong than in the case of $\cos\theta^*$.

---

[g] Property of a p_T spectrum to be shifted to higher values by a certain degree.

All the mentioned spin analysers have different dependencies on certain sources of systematic uncertainties. Therefore, a combination of these can be well considered in order to decrease systematic uncertainties on the measurement.

3.4.2. Experimental Status

ATLAS measurement

In the most recent publication of the measurement of the W-helicity by ATLAS [58] a template fit (see Sect. 8.2.2) has been performed to extract the helicity fractions from the data distribution in $\cos\theta^*$. The so-called 'asymmetry method' which also utilises the $\cos\theta^*$ distribution is described in [58]. Thus the results presented there are combinations of four different measurements using the template method and the asymmetry method in both the ℓ+jets and dileptonic channel. The analyses rely on a data set of $\int \mathcal{L}dt = 1.04\,\text{fb}^{-1}$ at a centre-of-mass energy of $\sqrt{s} = 7$ TeV. The obtained helicity fractions from the combined measurements are:

$$
\begin{aligned}
F_0 &= 0.67 \pm 0.03\,(\text{stat.}) \pm 0.06\,(\text{syst.}), \\
F_L &= 0.32 \pm 0.02\,(\text{stat.}) \pm 0.03\,(\text{syst.}), \\
F_R &= 0.01 \pm 0.01\,(\text{stat.}) \pm 0.04\,(\text{syst.}).
\end{aligned}
\tag{3.7}
$$

The results from the template method in the ℓ+jets channel only, were:

$$
\begin{aligned}
F_0 &= 0.57 \pm 0.06\,(\text{stat.}) \pm 0.09\,(\text{syst.}), \\
F_L &= 0.37 \pm 0.03\,(\text{stat.}) \pm 0.04\,(\text{syst.}), \\
F_R &= 0.07 \pm 0.03\,(\text{stat.}) \pm 0.06\,(\text{syst.}).
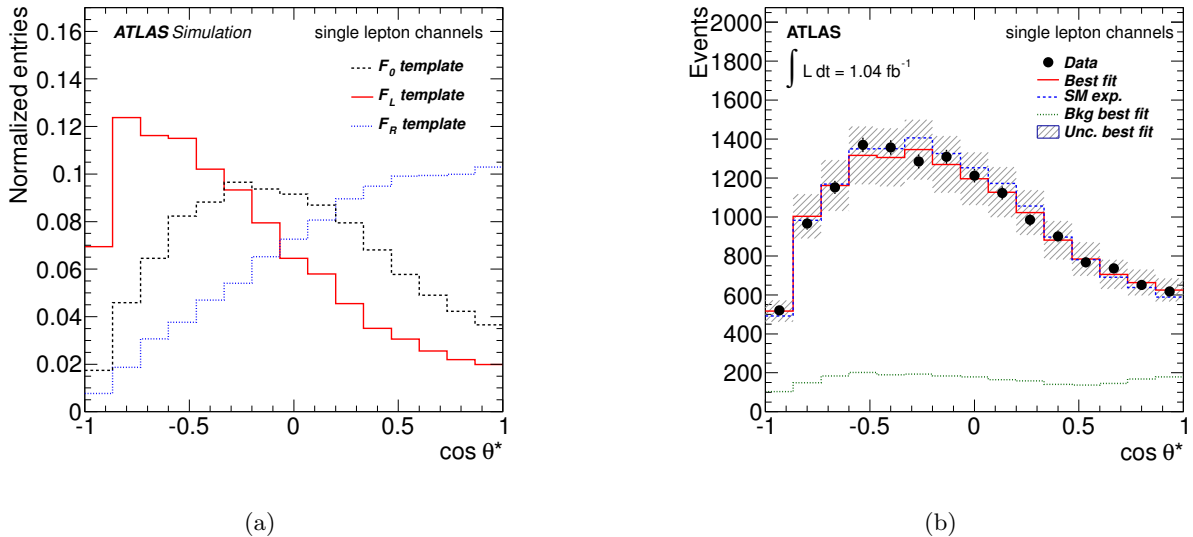\end{aligned}
\tag{3.8}
$$

(a)   (b)

Figure 3.9.: (a): Signal templates of the pure helicity states that were fitted to the data. (b): Result of the template fit to the data distribution. The best fit is shown with the data distribution and SM expectation. The background contribution is shown as well as the uncertainty band on the best fit. The plots are taken from [58].

All results are in agreement with the SM expectation. Fig. 3.9(a) shows the signal templates of the pure *W*-helicity fractions that were obtained from the PROTOS event generator [59]. Comparing these templates with the analytic forms of the fractions in Fig. 3.8 reveals some differences in the shapes. This is due to the imperfect detector resolution and acceptance and to the event selection which has an impact on the shape. Nevertheless, the templates show distinct shapes and are suited to apply the template method. Fig. 3.9(b) shows the result of the template fit in the ℓ+jets channel.

LHC combination

Recently, the LHC combination of ATLAS and CMS results of the *W*-boson polarisation has been made public [60]. The combination depends on several measurements corresponding to integrated luminosities of 35 pb^{-1} to 2.2 fb^{-1}. The *BLUE* method has been utilised to perform the combination accounting for correlations among the different measurements [61].
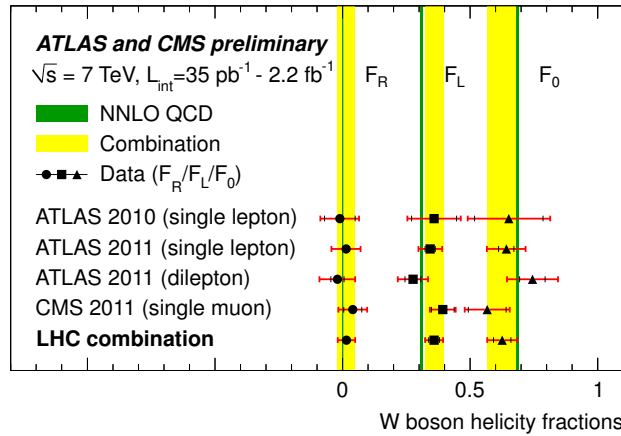

Figure 3.10.: Summary of the four included measurements by ATLAS and CMS and the LHC combination [60]. The inner error bars are the statistical uncertainty, the outer are the total uncertainty. The predictions from NNLO calculations [1] are the green lines.

$$F_0 = 0.626 \pm 0.034(\text{stat.}) \pm 0.048(\text{syst.}),$$
$$F_L = 0.359 \pm 0.021(\text{stat.}) \pm 0.028(\text{syst.}),$$
$$F_R = 0.015 \pm 0.034.$$

(3.9)

The results are depicted in Fig. 3.10 together with the NNLO prediction [1] and the included ATLAS and CMS results. The values can bee seen in Eq. 3.9. The fraction F_R has been deduced from the F_0 and F_L measurements assuming the sum of all fractions to be unity. The uncertainties could be further decreased with respect to Eq. 3.7. Also here, the result is in agreement with the NNLO QCD prediction. From this measurement, limits on the anomalous couplings g_R and g_L emerging in Eq. 3.5 can be derived. This can be done by using the formalism of effective field theories [62–64]. The limits derived in [60] assume V_R to be zero and the imaginary parts of g_R and g_L to vanish. Then the limits obtained are depicted in Fig. 3.11 in the $\Re(g_R)$-$\Re(g_L)$ plane. The region with non-zero $\Re(g_R)$ allowed here has been excluded by single top-quark cross-section measurements (predictions for large, non-zero $\Re(g_R)$ [65] in conflict with

measurement, e. g. in [66, 67]). Both couplings are compatible with zero. If further $g_L = 0$ is chosen, then $\Re(g_R)$ is determined to be:

$$\Re(g_R) = -0.10 \pm 0.06(\text{stat.})^{+0.07}_{-0.08}(\text{syst.}).$$
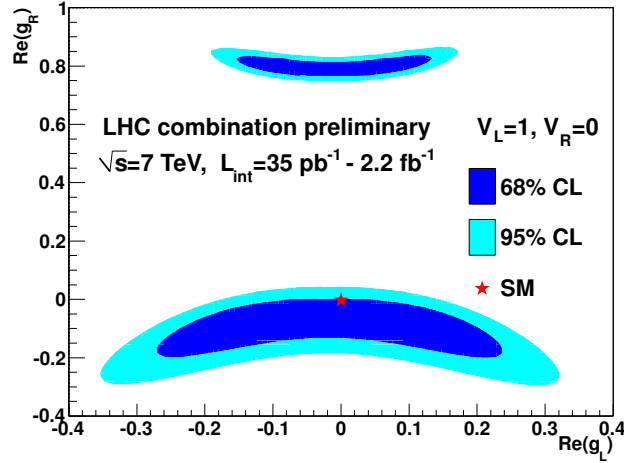
Figure 3.11.: Regions allowed on anomalous couplings from the LHC combination of the W-helicity fractions, assuming $V_L = 1, V_R = 0$. The 68% and 95% confidence levels are shown.

CMS measurement

Most recently, CMS has published their W-boson helicity measurement in the ℓ+jets channel with the full 2011 data set corresponding to $\int \mathcal{L}dt = 5.0\,\text{fb}^{-1}$ [68]. The helicity fractions have been extracted from data using a reweighting method that is also described in [68]. Their final results are:

$$\begin{aligned}
F_0 &= 0.682 \pm 0.030\,(\text{stat.}) \pm 0.033\,(\text{syst.}), \\
F_L &= 0.310 \pm 0.022\,(\text{stat.}) \pm 0.022\,(\text{syst.}), \\
F_R &= 0.008 \pm 0.012\,(\text{stat.}) \pm 0.014\,(\text{syst.}).
\end{aligned} \tag{3.10}$$

This measurement exceeds the precision of the LHC combination (Eq. 3.9) und is the most precise single measurement up to now. Again, the results are in agreement with SM predictions.

4. Experimental Setup

The data analysed in the *W*-helicity measurement has been recorded with the ATLAS [69, 70] detector at the Large Hadron Collider (LHC) [71] located at CERN (*Conseil Européen pour la Recherche Nucléaire*) near Geneva, Switzerland. A short introduction to the LHC and ATLAS and the analysed data is given in the following.

4.1. The Large Hadron Collider

The Large Hadron Collider is a proton-proton collider (built in the tunnel of the former Large Electron Positron collider LEP) with a circumference of about 27 km. The LHC ring lies on average 100 m underground. Before protons can be brought to collision at a centre-of-mass energy at the TeV scale, they have to be produced by ionising hydrogen atoms and pre-accelerated by a chain of linear and circular accelerators: After production, the protons are accelerated in the linear accelerator LINAC2 to energies of 50 MeV. Then the protons are injected into the circular accelerator BOOSTER and accelerated to an energy of 1.4 GeV. The BOOSTER then provides another synchrotron, the PS storage ring, with protons that are then further accelerated to 25 GeV before they enter the SPS, which is the largest pre-accelerator. The SPS then provides the LHC with protons of a start energy of 450 GeV. Bunches of protons are injected into the LHC in two different directions with a nominal bunch spacing of 50 ns. About 2808 bunches circulate in one beam and a bunch consists of roughly 10^{11} protons. Dipole magnets with a magnetic field of 8.6 T deflect the protons on their circular path and quadrupole as well as sextupole magnets serve for focusing the beams. The magnets and accelerating elements (cavities) are both super-conducting and are cooled down using liquid helium to temperatures of about 1.9 K. An important parameter is the luminosity $\mathcal{L}$ of an accelerator. The luminosity relates the event rate dN/dt to the cross-section σ of a certain process:

$$\frac{\mathrm{d}N}{\mathrm{d}t} = \sigma \mathcal{L}. \tag{4.1}$$

The total number of events N for a certain time interval is accordingly : $N = \sigma \int \mathcal{L} \mathrm{d}t$. The term $\int \mathcal{L} \mathrm{d}t$ denotes the *integrated luminosity*, this is the quantity that is of more interest than the *instantaneous luminosity* in Eq. 4.1, that is given in units of area^{-1}·time^{-1}. The instantaneous luminosity can be calculated via

$$\mathcal{L} = f \frac{N_b \cdot n_1 n_2}{4\pi \sigma_x \sigma_y}, \tag{4.2}$$

where f is the revolution frequency, N_b the number of bunches and n_1, n_2 the number of protons in the two colliding bunches. The beam spread, the cross-sectional area of the beam, is expressed by $4\pi \sigma_x \sigma_y$, where the spread in both x- and y-direction is assumed to be Gaussian. Thus, it is desired to have well focussed beams with small spread at the interaction point to ensure a high interaction rate.

ATLAS is one of four main experiments at the LHC, located at one of four interaction points. The other experiments are CMS (Compact Muon Solenoid) [72], ALICE (A Large Ion Collider Experiment) [73] and LHCb [74].
In 2010 and 2011, the centre-of-mass energy was 7 TeV and has been increased to 8 TeV in 2012. In early 2013, the LHC has been operated with proton-Pb collisions until the 6th of February, followed by a short period of *pp*-collisions until 14th of February, the last day of LHC Run I. The LHC shutdown will last for about two years, during which the accelerator and the experiments will be upgraded for the run with $\sqrt{s}$ =13-14 TeV.

The data analysed in this thesis were recorded by ATLAS in 2011 and correspond to an integrated luminosity of $\int \mathcal{L}\mathrm{d}t = 4.7$ fb^{-1}. In 2012 the LHC provided another 21.7 fb^{-1} that were recorded by ATLAS [75]. In Fig. 4.1, the development of the integrated (a) and instantaneous peak luminosity (b) are shown for the three years of operation. In both plots a clear increase over the years can be observed. Though, the design luminosity of 10^{34} cm^{-2}s^{-1} has not been reached, as well as the design centre-of-mass energy of 14 TeV, the LHC ran successfully and a lot of successful analyses have been performed using the large amount of data recorded by ATLAS, not to mention the Higgs-boson discovery.
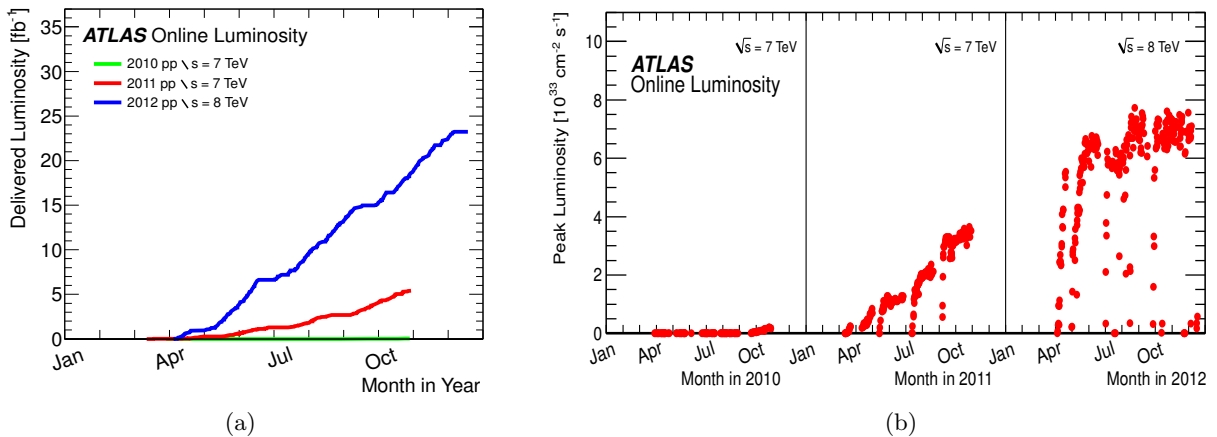
Figure 4.1.: (a): Integrated luminosity $\int \mathcal{L}\mathrm{d}t$ recorded by ATLAS in the years 2010, 2011 and 2012 as a function of time. (b) Instantaneous luminosity $\mathcal{L}$ as a function of time for 2010, 2011 [76] and 2012 [75] runs.

In the following, a description of the ATLAS detector with the used coordinate system and the various components is given.

4.2. The ATLAS Detector

With a length of 44 m, a diameter of 25 m and a weight of approximately 7 000 tons, the ATLAS experiment (A Toroidal LHC ApparatuS) is the largest collider experiment ever built [69, 70]. It is designed to investigate a wide range of particle physics topics, one of them being top-quark physics. The ATLAS detector has a forward-backward symmetric design around the interaction point and covers nearly the entire solid angle. The detector consists of four main components: the inner detector, electromagnetic and hadronic calorimeters, the muon spectrometer and the

magnet system containing solenoidal and air-cored toroidal magnets. These components can be seen in Fig. 4.2 which is a computer simulated cut-away view of the whole detector. All components will be described further in the following, after the necessary observables belonging to the coordinate system of the detector have been established.
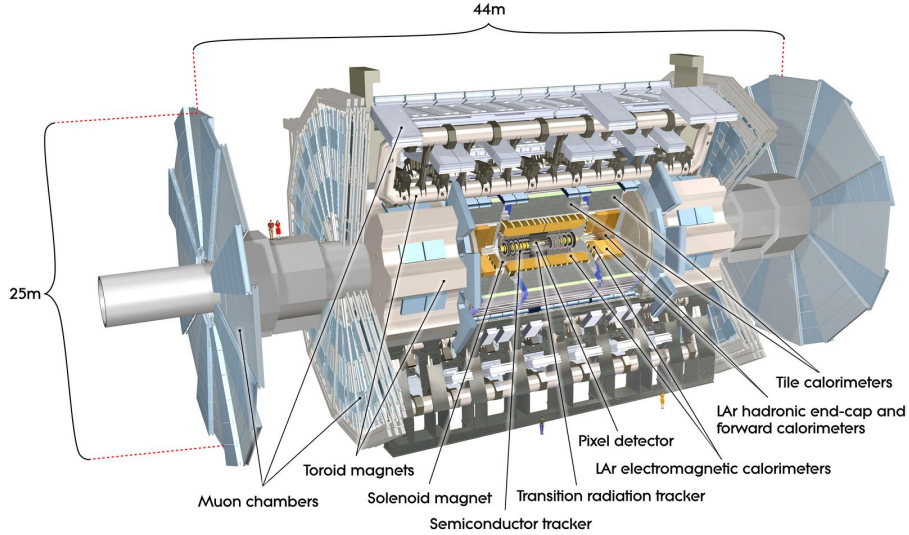

Figure 4.2.: Cut-away view of the ATLAS detector. The various components are indicated as well as the measures in length and diameter of the detector [70].

4.2.1. Coordinate System

In ATLAS, the measured variables of particles that traverse the detector are defined in a right-handed cartesian coordinate system. The origin lies in the interaction point, the z-axis points along the beam pipe, the x-axis points to the centre of the LHC-ring while the y-axis points vertically upwards. The x, y-plane is the so-called transverse plane in which the azimuthal angle ϕ is measured. The polar angle θ is the one between z-axis and momentum direction of the particle. Thus, the transverse momentum and energy are defined as $p_T = p \sin \theta$ and $E_T = E \sin \theta$, respectively. The magnitude of the measured momentum is $p = \sqrt{p_x^2 + p_y^2 + p_z^2}$ and E is the total energy measured in the calorimeters and the muon system[a]. Later on, the so-called *pseudo-rapidity* η will be used. It is defined as:

$$\eta = -\ln \left(\tan \left(\frac{\theta}{2} \right) \right).$$

An advantage of this variable is that differences in η are invariant under Lorentz boosts along the beam axis. The various detector components cover different regions in η. The transverse plane with $z = 0$ has $\eta = 0$, the beam pipes to both directions $\pm z$ exhibit a pseudo-rapidity of $\eta = \pm \infty$. Geometrical distances of objects are expressed using ΔR:

$$\Delta R = \sqrt{\Delta \eta^2 + \Delta \phi^2}.$$

---

[a] Momentum information is used for muons as they deposit only little of their energy in the calorimeters.

4.2.2. The Inner Detector

Track reconstruction of charged particles can be done by either measuring ionisation or scintillation signals, Cherenkov photons or photons from transition radiation. The goal of tracking is to determine the momentum of charged particles that are deflected in a magnetic field, the sign of the charge and the position itself to reconstruct vertices. This is crucial for determining the identity of long-lived particles that can travel a certain distance from the primary interaction point before they decay (e. g. *b*-tagging). Typically, the momentum resolution becomes worse for high p_T particles whose tracks are hardly bent, the relative uncertainty therefore increases with increasing momentum: $\sigma(p)/p \propto p$. Track reconstruction is done in ATLAS in the inner detector. For muons, it is also done in the muon chambers.

The inner detector (ID) is the first component that is traversed by particles that leave the interaction point. The ID is surrounded by a solenoid magnet that provides a magnetic field of 2 T. The ID covers the full azimuthal angle ϕ. The central part of the beam pipe consists of beryllium and has an inner diameter of 58 mm and a thickness of 0.8 mm ensuring minimal multiple scattering of the particles leaving the interaction vertex. Closest to the beam pipe is the pixel detector, the first pixel layer being 15.7 mm away from the beam pipe. The pixel detector consists of three layers. The pixel sensors are made of silicon and have a size of $50 \times 400 \ \mu m^2$. The semiconductor material is doped and possesses np-junctions. A charged particle traversing the depleted silicon sensor will create electron-hole pairs that will be measured on the electrodes and create a signal. The pixel detector exhibits a high granularity with about 80.4 million readout channels. As it is closest to the beam pipe it experiences the highest particle flux and therefore must be radiation hard. The pixel detector is followed by the semiconductor tracker
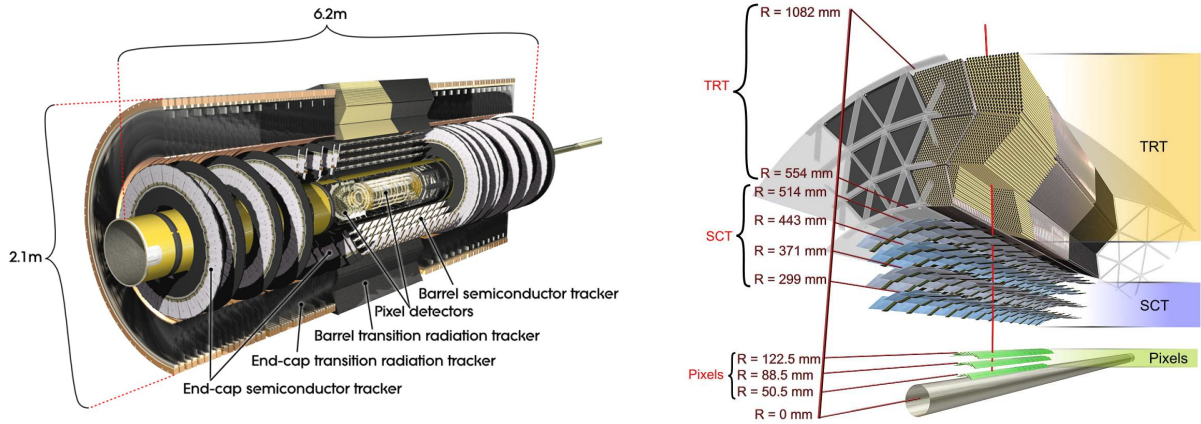
Figure 4.3.: View of the ID tracking detector [70]: Left: all three components of the ID are shown with barrel and end-cap components. Right: Transverse view of the ID illustrating a path of a traversing particle through the various layers (red line). The numbers given are distances to the beam axis.

(SCT) that consists of silicon microstrip sensors with a strip pitch of 80 μm. This component is larger than the pixel detector but has the same working principle. Both, pixel detector and SCT, consist of a barrel region with concentric, cylindrical layers around the beam pipe and two end-cap regions with disks perpendicular to the beam pipe. The SCT exhibits four double layers in the barrel region and therefore typically provides information from eight measured

space points for a track and contains about 6.3 million readout channels. Both, pixel detector and SCT, cover a region in pseudo-rapidity of $|\eta| < 2.5$. They are operated at low temperatures of about $-5°C$ to $-10°C$.

The third part of the inner detector is the transition radiation tracker (TRT) as the outermost component. It consists of straw tubes with a diameter of 4 mm that contain a gas-mixture of 70% Xenon, 27% CO_2 and 3% O_2. In the barrel region they are aligned parallel to the beam axis, in the end-caps they are arranged radially in wheels. It covers a region in η of $|\eta| < 2.0$. The TRT provides extended tracking information stemming from the measurement of drift time of a charge after ionisation of the gas content caused by charged particles. The TRT has 351 000 readout channels. Only R-ϕ spatial information is available. Nevertheless, it provides significant information for the momentum measurement due to the long lever arm and almost continuous track information. It also gives additional electron identification information via the detection of transition-radiation photons. Transition radiation occurres when a relativistic charged particle crosses the interface of two regions with different refraction indices, i. e. $n_1 \neq n_2$. The signal intensity depends on the γ-factor of the particle: the higher γ, the more transition radiation will be produced.

Fig. 4.3 shows two different cut-away views of the ID with its above described components. Length scales are also given.

4.2.3. The Calorimeters

Calorimeters are used to measure the energy E of particles created in a collision. One distinguishes between electromagnetic and hadronic calorimeters. The principle is the same for both types: the energy of the particle has to be converted into light or charge signals to be measured. Two main concepts for measuring the energy by stopping the particle exist: homogeneous and sampling calorimeters. Sampling calorimeters consist of a dense material to brake the particles and an active material that produces a light or charge signal that can be read out. These two materials are ordered in alternating layers. A homogeneous calorimeter consists of a single material that is able to stop particles and at the same time produces measurable signal output. The mechanism that stops particles is for both calorimeter types the same: electrons and photons lose energy via Bremsstrahlung and e^+e^--pair creation, respectively. This way showers evolve in the electromagnetic calorimeter where N secondary particles are produced. The shower stops, when the energy of the secondaries is too low to produce other particles. The energy of the shower is proportional to the number of secondary particles N. The same happens in a hadronic shower initiated by hadrons. The difference is, that here the particles are interacting strongly with the nuclei of the calorimeter material.

For sufficient stopping power of an electromagnetic (em.) calorimeter, the smallness of the so-called *radiation length* X_0 is a quality criterion: The behaviour of the remaining energy of a particle passing through the detector material is written as:

$$\langle E(x) \rangle = E_0 \cdot e^{-x/X_0},$$

where x is the travelled distance in the detector and E_0 is the initial energy of the particle. Thus, X_0 defines the average distance in which a particle loses the fraction $1/e$ of its original energy. The depth for total absorption of a particle grows logarithmically with the particle energy and X_0 is the length scale for an em. shower. Em. calorimeters have a length of several X_0 (about 20 X_0) and therefore X_0 should be a small number.

For hadronic showers, the interaction length for nuclear absorptions λ is a scale for the shower length. Hadrons lose their energy by inelastic scattering with nuclei of the detector material,

λ is typically bigger than X_0. Therefore, the hadronic calorimeters are bigger and are placed behind the em. calorimeters. The signal response of the hadronic calorimeter is lower compared to the response of the em. calorimeter. This is due to several reasons: the hadronic calorimeter is non-compensating, shower components such as neutrinos and muons from leptonic decays inside hadrons cannot be measured, thus they take away their energy fraction. Also, energy might get lost in nuclear reactions instead of being converted to scintillation light or charge. A hadronic shower will always contain an em. component due to the production of neutral π^0 mesons that decay immediately via $\pi^0 \to \gamma\gamma$. The response to em. and hadronic components of the calorimeter is different leading to a non-linear calorimeter response.

The energy resolution of calorimeters can be parameterised by[b]:

$$\frac{\sigma(E)}{E} = \frac{a}{\sqrt{E}} \oplus \frac{b}{E} \oplus c. \tag{4.3}$$

The first term multiplied by a is the stochastic term stemming from the Poissonian fluctuations of the particle number N in a shower ($\sqrt{N} \sim \sqrt{E}$). The second term with b comes from noisy detector components that disturb the signal. The constant term c accounts for energy leakage due to dead detector material (support structure, electronic readout), calibration uncertainties, non-uniformity and non-compensation of the calorimeter. In contrast to the momentum measurement in the track detectors, the relative energy resolution improves with higher energies of the particles, which can be seen from Eq. 4.3.
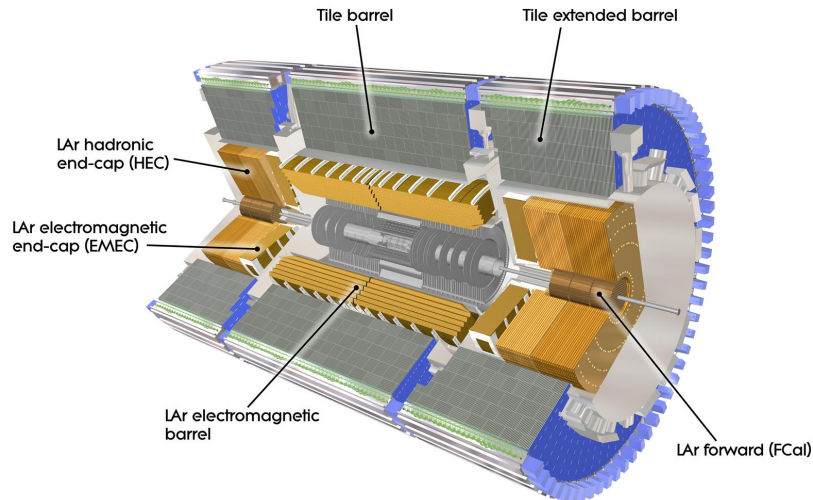
Figure 4.4.: Cut-away view of the electromagnetic and hadronic calorimeter that are located outside the solenoid magnet that houses the ID [70].

In Atlas, both em. and hadronic calorimeters are sampling calorimeters. The calorimeters exhibit high granularity which allows for a high spatial resolution. Thus, the calorimeter consists of *cells*. Adjacent calorimeter cells that have a signal are called a *cluster*. The calorimeter system is also divided into barrel and two end-cap regions. Additionally, forward calorimeters exist. Each component is placed in an individual cryostat. The calorimeter system of Atlas is

---

[b] The operator $\oplus$ means to add the terms in quadrature: $a \oplus b \to \sqrt{a^2 + b^2}$.

depicted in Fig. 4.4. The em. calorimeter is a lead and liquid Argon (LAr) sampling calorimeter with accordion-shaped Kapton electrodes for efficient stopping and fast response. Lead serves as passive absorber material and LAr produces signal via scintillation light. Both barrel and end-cap em. calorimeters cover the region $|\eta| < 3.2$. A forward em. copper/LAr calorimeter covers the region $3.2 < |\eta| < 4.9$ in addition.

Directly outside the em. calorimeter, the hadronic tile calorimeters are installed. They consist of steel as passive absorber material and scintillating tiles as active material. The barrel and the extended barrel tile calorimeter (see Fig. 4.4) cover the region with $|\eta| < 1.7$. Two sides of the scintillating tiles are read out by wavelength shifting fibres connected to two photomultiplier tubes. The central region with $\eta = 0$ extends to about $11 \cdot \lambda$ providing full containment of hadronic showers and avoiding punch-through effects into the muon system. The hadronic end-cap calorimeter is again a lead/LAr calorimeter that covers $1.5 < |\eta| < 3.2$. The very forward region with $3.2 < |\eta| < 4.9$ is covered by an additional hadronic tungsten/LAr calorimeter.

4.2.4. The Muon Spectrometer

The outermost part of the Atlas detector comprises the muon spectrometer. Only muons are expected to reach the muon chambers. Due to the character of high energetic muons to be minimum ionising particles, they deposit less energy in the calorimeter and leave the detector unabsorbed. They are then detected in the muon system consisting of *cathode strip chambers* (CSC) and monitored drift tubes (MDT). These components provide additional momentum information on the muons. The tracks are bent by toroidal magnets producing a peak magnetic field of about 4 T. The *thin gap chambers* (TGC) and *resistive plate chambers* (RPC) are two additional detector components that are mainly used for triggering muon events. All four components of the muon spectrometer cover in total a region of $|\eta| < 2.7$ in pseudo-rapidity. Fig. 4.5
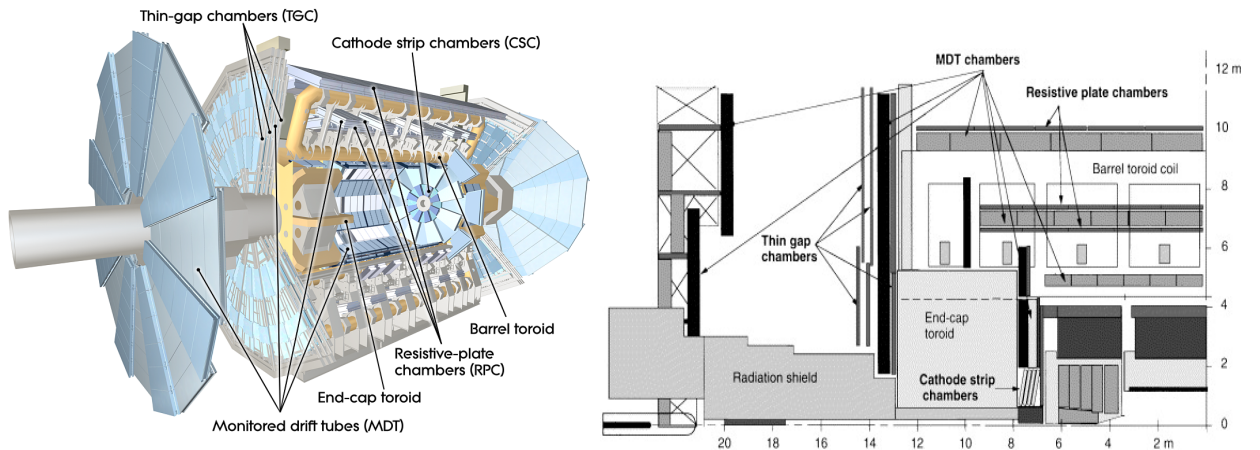
Figure 4.5.: Left: Cut-away view of the Atlas muon spectrometer system with indicated subsystems. Right: Same for the view in the y, z-plane showing one quadrant and length measures [70].

shows the Atlas detector with the focus on the muon system components. The right-hand side of this figure shows the fourth quadrant of the y, z-plane through the detector and the length scales are given in both directions. The CSCs are installed at $z = 7$ m in the forward region just in front of the end-cap toroid magnet. These are multi-wire proportional chambers filled with a Ar/CO_2 mixture (80%/20%). The muon tracks are thus measured by measuring the ionization

signal from the traversing muon. The MDT consists of aluminum wire tubes, filled with 93% Ar and 7% CO_2. The signal is created the same way as in the other three components. The drift time of the charge in the tubes is longer (about 700 ns) than the bunch spacing. In order to distinguish muons from different bunch crossings, timing information from the RPC is used. The RPC has a good timing resolution being composed of two plates filled with gas (capacitor) having a distance of about 2 mm from each other. It is installed in the barrel region and used to trigger muon events and measure the azimuthal angle ϕ. To trigger muon events in the forward region, the TGCs are used that are also multi-wire proportional chambers. The TGCs also provide ϕ information.

4.2.5. Performance Goals

The performance goals of all tracking and calorimeter components of ATLAS with respect to the resolution are shown in Tab. 4.1. The resolution power of the several detectors is illustrated, where the discussed resolution behaviours are followed; for the energy resolution, noise terms are omitted. The given values may differ from those actually achieved, nevertheless, the tendencies are visible. The energy measurement is more precise for em. calorimetry than for hadronic calorimetry, where the reasons were discussed in Sect. 4.2.3.

Crucial for the momentum measurement of charged particles is the magnet system, that will be briefly discussed next.

Detector Component	Required Resolution
Tracking (ID)	$\sigma_{p_T}/p_T = 0.05\% p_T \oplus 1\%$
EM calorimetry	$\sigma_E/E \ = 10\%/\sqrt{E} \oplus 0.7\%$
Hadronic calorimetry:	
barrel and end-cap	$\sigma_E/E \ = 50\%/\sqrt{E} \oplus 3\%$
forward	$\sigma_E/E \ = 100\%/\sqrt{E} \oplus 10\%$
Muon spectrometer	$\sigma_{p_T}/p_T = 10\%$ at $p_T = 1$ TeV$/c$

Table 4.1.: Performance goals of the different detector components. The units for E and p_T are in GeV and GeV$/c$, respectively [69].

4.2.6. The Magnet System

Both the solenoid and the air-cored toroidal magnets work with super-conduction technologies. While the solenoid magnet bends the tracks in the ID, the toroid magnets provide the relevant bending field for the muon spectrometer. The toroid system has one barrel and two end-cap components. Each of these consist of eight toroids that are assembled with an eight-fold azimuthal coil symmetry around the calorimeters (for the barrel region; for end-cap: behind the calorimeter). The end-cap toroids are rotated with respect to the barrel toroids (see Fig. 4.6) to ensure radial overlap and optimise the bending power at the interface of the systems. The usage of toroidal coils leads to a rather complicated, non-uniform magnetic field at the position of the muon chambers. However, the advantage of this system is, that the air-cored toroidal coils instead of an iron return yoke for the solenoidal field outside the calorimeters lead to less multiple scattering which leaves muon tracks almost undisturbed.
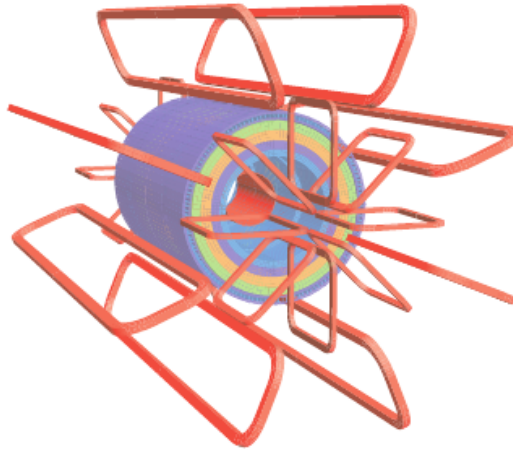
Figure 4.6.: Geometry of barrel and end-cap toroidal windings (red). In the center, the solenoid is displayed with the tile calorimeter plus outside return yoke. The different colours illustrate different magnetic properties of the tile calorimeter.

4.2.7. The Trigger System

For peak instantaneous luminosities of the order of 10^{34} cm^{-2}s^{-1}, it is unavoidable to make use of a trigger system: the expected collision rate of 40 MHz can neither be fully recorded nor fully reconstructed for analyses in time. To reduce the amount of data to be finally analysed, ATLAS uses a *three-level trigger system* that only chooses events of interest that are permanently stored on disk. Most of the time, low-momentum scattering processes that do not produce new particles will take place in the *pp* collisions. These events do not have to be stored and can be discarded. Therefore, the level-1 trigger L1 searches for high-p_T muons, electrons, photons, jets, hadronically decaying τ-leptons as well as large transverse energy and large missing transverse momentum, $\not{E}_T$, which are characteristic for interesting events. The L1 trigger only uses a subset of the available detector information to make fast decisions while keeping events in less than 2.5 µs. L1 is completely hardware-based: the information on high-p_T muons is gathered from the trigger chambers TGC in the end-cap region and the RPCs in the barrel region. Information on electrons, photons, jets, total energy and $\not{E}_T$ is provided by the calorimeter. The calorimeter selection relies on reduced-granularity information. The L1 trigger then defines so-called regions of interest (ROI) that exhibit a special feature and passes the information of the kind of feature and the region in η-ϕ space to the high-level trigger. The L1 trigger reduces the event rate to about 75 kHz. The high-level trigger is software-based and divided into L2 trigger and Event Filter. The L2 trigger checks the ROIs and accesses the full granularity information from all detector components to reconstruct the events. The L2 has an event processing time of about 40 ms. It is able to reduce the event rates further to 3.5 kHz, mainly due to more precise momentum measurements and to certain requirements on energy clusters in the calorimeter. Finally the Event Filter (EF) computing farm processes the events in about 4 s per event. It reconstructs and analyses the data with high precision algorithms. More complex reconstructions of certain objects is done and eventually the event rate is further reduced to 200 Hz. The data acquisition system (DAQ) finally stores events that passed the EF permanently and provides the data for physics analyses.

5. Object Definition

The analysis of $t\bar{t}$ events in the ℓ+jets channel requires the identification of electrons, muons, jets and missing transverse momentum due to a neutrino. Therefore, these four objects are introduced in the following. All detector components described in Sect. 4.2 need to be fully operational to provide the required information on these objects. Trigger and reconstruction efficiencies are ideally close to 100%. They must be estimated in both data and MC. In most of the cases, the so-called *tag-and-probe method* is used, that is described e.g. in [77–80].

5.1. Electrons

Electrons are identified and reconstructed from track information in the ID and an electromagnetic cluster in the calorimeter. The transverse energy is calculated by

$$E_T = \frac{E_{\text{cluster}}}{\cosh\left(\eta_{\text{track}}\right)}.$$

Electromagnetic clusters are built with the help of the *sliding window* algorithm [79] that combines calorimeter cells to clusters using seed clusters with energy depositions of $E_T > 2.5$ GeV. The transverse energy has to be larger than 25 GeV. At least one track in the ID has to be matched to the em. cluster. Due to the coverage of the detector components in pseudo-rapidity, electrons have to fulfil $0 \leq |\eta_{\text{cluster}}| \leq 2.47$. The transition region between barrel and end-cap calorimeter is not well instrumented and thus called *crack region*. Therefore, the region of $1.37 \leq |\eta_{\text{cluster}}| \leq 1.52$ is excluded. Furthermore, the impact parameter z_0 with respect to the primary vertex of an event has to hold: $|z_0| < 2$ mm. Electrons can be classified as 'loose', 'medium' and 'tight' according to different requirements on the track and calorimeter isolation. Isolation criteria are quantified by building a cone of a certain size ΔR around the electron direction and requiring that the energy deposition/transverse momentum in this cone is not larger than a certain value. Jets that lie inside a cone of $\Delta R = 0.2$ around the electron are removed. If, after this jet overlap removal, jets with $p_T > 20$ GeV are present within $\Delta R = 0.4$, the electron is discarded. During the 2011 data taking period, there has been a malfunction of readout boards of the LAr calorimeter, which is referred to as LAr hole in a certain $\eta \times \phi$ region. This hole could be reproduced in the simulation and therefore no additional requirements are needed.

5.2. Muons

Muons can be reconstructed in several ways. In this analysis, the combined reconstruction of muons in the ID and the MS is performed. Therefore, tracks in the ID have to be matched to hits in the MS. Not only the $\eta \times \phi$ regions have to be matched but also the measured momenta have to be compatible. Muons must have $p_T > 20$ GeV (plateau of trigger efficiency, close to 100%). According to the relevant detector components, muons have to fulfil: $|\eta| < 2.5$. To ensure that one considers prompt muons from the hard process and not from heavy flavour

decays inside a jet, also here isolation criteria are applied: the energy deposition in $\Delta R < 0.2$ around the muon direction has to be smaller than 4 GeV, the measured p_T within $\Delta R = 0.3$ has to be smaller than 2.5 GeV. If a jet lies within $\Delta R = 0.4$ to a muon, the muon is discarded. Moreover, the impact parameter z_0 also has to fulfil $|z_0| < 2$ mm. Also muons can be classified as loose, medium and tight, they have to fulfil certain hit requirements in the layers of the pixel, SCT and TRT detectors. Cosmic muons have to be rejected, therefore one requires a cut on the impact parameter d_0 with respect to the beam spot: $|d_0| < 0.5$ mm.

5.3. Jets

Jets are reconstructed using the anti-k_t jet clustering algorithm [81]. The algorithm uses $\Delta R = 0.4$ which is the minimum distance between two jet axes. Topological clusters from the calorimeter are built and matched to tracks in the ID. Calorimeter cells with a signal-to-noise ratio of $S/N > 4$ are used as seeds for the clustering. Surrounding cells that have $S/N > 2$ are added to the cluster. The measured energy has to be calibrated to both electromagnetic and hadronic scales. The correction factors depend on the η and p_T of the jets. Also, the uncertainty on the jet energy scale (JES) calibration is η- and p_T-dependent. The JES calibration is different in MC samples for full and fast detector simulation. Jets need to have $p_T > 25$ GeV and $|\eta| < 2.5$. Jets with $7 \leq p_T \leq 20$ GeV are considered as *soft-jets* and are important for the $\not{E}_T$ calculation (see Sect. 5.4). To discriminate against jets coming from pile-up[a], requirements are applied on the *jet vertex fraction*, JVF. It is defined as the fraction of all summed track p_T of a jet belonging to the particular primary vertex. For 2011 data analyses, JVF > 0.75 is required. After the full event selection a 'jet cleaning' is applied to remove events that contain a 'bad' jet. These jets have $p_T > 20$ GeV and are fake jets due to calorimeter noise or beam halo or cosmics induced activity in the detector. Jet cleaning is applied to both data and MC events.

5.3.1. *b*-tagging

In top-quark analyses, the identification of jets originating from a *b*-quark is crucial. Identifying a jet as a *b*-jet with the help of certain algorithms is called *b-tagging*. These algorithms make use of the rather long lifetime of mesons containing *b*-quarks which is of the order 1 ps and implies a travel distance from the primary vertex, where they are created, of about 1 mm. This way a secondary vertex with a certain impact parameter w.r.t. the primary vertex can be observed. The applied *b*-tagging algorithm is the MV1 tagger, which is used at the 70% operating point which is the efficiency ε of tagging *b*-jets [82, 83]. The probability to tag non *b*-jets by mistake is 1/134. The MV1 tagging algorithm is based on a neural network that uses inputs from several different taggers. These are SV0, IP3D and JetFitterCombNN [82]. The SV0 tagger relys on the reconstruction of secondary vertices, IP3D uses the impact parameter, the JetFitterCombNN uses several topological variables to discriminate against non-*b*-jets. The MV1 combines all the outputs to one single weight for each jet. At the 70% working point, the cut on this weight is applied at 0.602. The various *b*-tagging algorithms have to be calibrated as the MC simulation not fully describes the detector performance. The *b*-tag calibration will be explained in Sect. 9.1.2.

---

[a] Jets that stem from a different hard interaction that can be due to the same bunch crossing (in-time) or to interactions in neighbouring bunch crossings (out-of-time pile-up).

5.4. Missing Transverse Momentum

An important feature of ℓ+jets events is the occurrence of missing transverse momentum $\not{E}_T$ in the event due to an escaping neutrino. This $\not{E}_T$ stems from a momentum imbalance in the detector: momentum conservation requires the vector sum over all p_T to vanish, if this is not the case, $\not{E}_T$ is non-zero. The missing transverse momentum is calculated by [84]:

$$\not{E}_T = \sqrt{\not{E}_x^2 + \not{E}_y^2} \tag{5.1}$$

$$\text{with} \quad \not{E}_{x,y} = \not{E}_{x,y}^{\text{calo}} + \not{E}_{x,y}^{\text{muon}}. \tag{5.2}$$

As for the energy measurement, the $\not{E}_T$ information is composed of information from the calorimeters and from the muon chambers as is indicated in Eq. 5.2. The calorimeter term, denoted by 'calo' is determined by:

$$\not{E}_x^{\text{calo}} = -\sum E_i \sin\theta_i \cos\phi_i,$$
$$\not{E}_y^{\text{calo}} = -\sum E_i \sin\theta_i \sin\phi_i.$$

The sum is calculated over all calorimeter cells i that registered energy depositions, where θ_i and ϕ_i are the associated polar and azimuthal angle, respectively. The $\not{E}_T$ term reconstructed in the muon system (denoted by 'muon') is calculated via the negative vector sum of measured momenta p^μ:

$$\not{E}_{x,y}^{\text{muon}} = -\sum_{\text{muons}} p_{x,y}^\mu.$$

The energy measurement in the calorimeter is calibrated to certain physics objects in the order: electrons, photons, hadronically decaying τ-leptons, jets and muons. Calorimeter cells associated to one of these objects are reweighted by using the respective calibration scheme obtained from Monte Carlo (MC) simulations validated by extensive test beam measurements. If energy deposits of calorimeter cells cannot be associated to a physics object, then a global calibration scheme is used. The term is added as a so-called 'cell-out' term to the $\not{E}_T$ calculation and influences the $\not{E}_T$ resolution [84]. Finally, the calorimeter term of $\not{E}_T$ is composed of:

$$\not{E}_{x,y}^{\text{calo}} = \not{E}_{x,y}^{\text{electron}} + \not{E}_{x,y}^{\text{photon}} + \not{E}_{x,y}^{\tau} + \not{E}_{x,y}^{\text{jets}} + \not{E}_{x,y}^{\text{softjets}} + \left(\not{E}_{x,y}^{\text{calo}\mu}\right) + \not{E}_{x,y}^{\text{cell-out}},$$

where the soft-jet term refers to the soft-jets defined in Sect. 5.3. The $\not{E}_{x,y}^{\text{calo}\mu}$ is embraced because of the mentioned smallness of energy deposits from muons in the calorimeter.

6. Monte Carlo Simulation

Many analyses in particle physics rely heavily on the input of Monte Carlo (MC) event generators. This is also true for this analysis and therefore a short overview over basic principles of MC generators is given in this chapter. The first section (Sect. 6.1) introduces the concepts of MC techniques and MC event generation in general, including some remarks on detector simulation. The second section (Sect. A.1) describes the used MC samples for the W-helicity analysis.

6.1. Overview

The quantum mechanical nature of physics processes in high energy physics makes it impossible to predict the outcome of a certain interaction. The theory can predict processes and how probable it is that they occur. Thus, only ensembles of measurements can be compared with theoretical expectations. To model the theoretical expectation in particle collisions, MC techniques are devised that provide at first hand the possibility to compare experiment and theory. Further, with the help of MC simulations possible backgrounds for analyses can be predicted, detector and trigger designs can be optimised, the feasibility of physics studies can be estimated, analysis strategies devised etc. The next sections give a short overview over the working principles of MC generators.

6.1.1. Monte Carlo Integration

To calculate measurable quantities like cross-sections and differential cross-sections of a certain process, one encounters integrals that cannot be solved analytically. In this case, numerical integration can be performed. The best method to do so, is to use MC integration techniques. MC integration techniques use (pseudo) random numbers as input. Pseudo random numbers are random numbers generated according to a certain distribution. These are used to perform *importance sampling* of a function (see e. g. [85]). The hit-and-miss method is followed combined with the importance sampling to evaluate the integral of a function. The advantage of this method compared to other numerical methods (Simpson rule, trapezoidal rule) is, that the error on the integral scales with $1/\sqrt{N}$, N being the number of sampling points, independent of the dimension d. Other MC integration algorithms exist.

6.1.2. Event Generation

Being able to calculate integrals makes it now also possible to generate whole events. True random variables are used by MC generators as input as they represent quantum mechanical choices. Based on random numbers calculations can be done, but the matrix element (ME) and phase space are not the only ingredients of an event occurring in particle collisions. At a hadron collider, modelling of particle collisions is a complex task: Fig. 6.1 gives an impression of the tasks that have to be carried out in one single event simulation: the partons of two protons can produce new particles in a hard process. This can be calculated by using ME and PDFs of the incoming protons. Further, the produced particles will undergo QCD Bremsstrahlung if they are gluons

or quarks, a *parton shower* (PS) has to be modelled. Additional hard interactions can occur (multiple parton interactions, MPI), the showered particles will form hadrons (hadronisation) that may decay further. Eventually, one ends up with hundreds of particles in the final state, each of them having about 10 degrees of freedom. In MC generators, the steps from hard process to final state are handled in a probabilistic way. Parton shower and hadronisation have to be modelled, as they take place in a non-perturbative regime, where calculations are difficult. Several generators exist that handle different stages of event generation differently. The three general purpose generators are PYTHIA [86], HERWIG [87] and SHERPA [88]. Basic principles for all generators are the usage of *DGLAP* [89–91] evolution for PDFs and parton showers. The DGLAP equations deal with the splitting probability of colour charged particles at a certain scale Q^2. Also the concepts of *Sudakov form factors* [92] is utilised when developing showers. The hadronisation is modelled differently in the various generators. Two basic models exist for performing the hadronisation: the *string fragmentation* model [93] (implemented in PYTHIA) and the *cluster fragmentation* model [94] (implemented in HERWIG and SHERPA). After hadronisation and decay of the instable hadrons, detector simulation takes over.
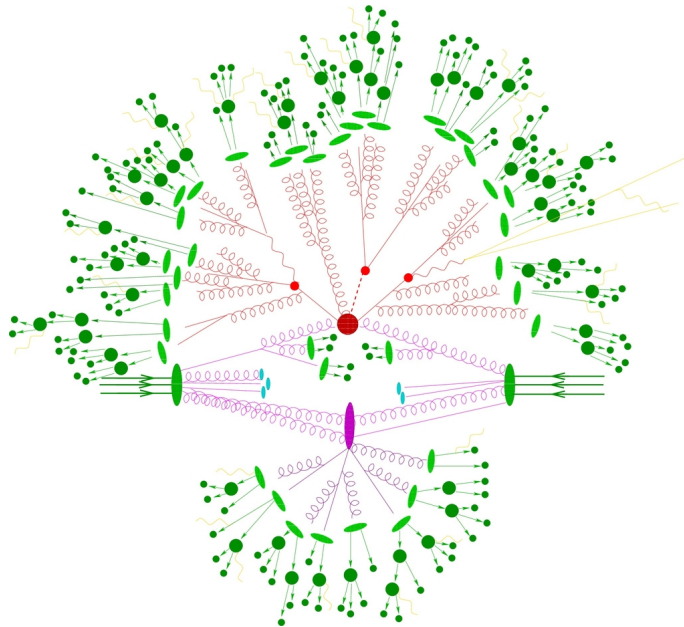

Figure 6.1.: Illustration of typical processes in hadron collisions: the hard process is indicated by the dark red blob, in this case $t\bar{t}H$ production. The three unstable particles decay (red blobs) and produce secondary particles. Another hard interaction can occur (purple blob). Parton shower, hadronisation and decay of hadrons and photon radiation is also indicated in this figure. Figure taken from [88].

6.1.3. Detector Simulation

The full physics simulation of particle collisions is done in the previously described MC event generation. The final states of the event are described on particle level (hadrons, leptons, photons). This has to be taken further to the detector level, to be able to compare actual measurements with MC outputs. Therefore, a detector simulation needs to be performed, which is done in ATLAS via the GEANT4 toolkit [95] or via the ATLFAST II simulation tool [96]. The step of simulating the passage of produced particles through the experimental apparatus is called 'MC

radiation transportation', or simply detector simulation. It requires the most computation time. While the physics within the MC generators is the same for all experiments at a collider, the detector simulation is individual for each experiment, beginning from the beam pipe to the end of the cavern, the detector is located in. Detector simulation is non-deterministic, meaning that random numbers are used as input to reproduce distributions instead of solving equations. The geometry of a detector and the material used must be modelled. When transporting a particle through the detector one has to simulate Bremsstrahlung, pair creation, multiple scattering etc. Particles are transported through the detector until their energy (E_{kin}) falls below a certain threshold, where the simulation is over. Not only energy deposits, electric and magnetic field effects and the creation of new particles are modelled, but also the electric current and voltage signals, thus the detector response is simulated. Thereby, the same reconstruction chains can be used which are later on applied to real data.

When performing detector simulation one has to find a compromise between low CPU time and accuracy of the modelling: not too detailed physics models and detector geometry can be included (e. g. screws, cables etc. can never be modelled).

6.2. Monte Carlo Samples

For the W-helicity measurement, signal and background processes except for the multijet background are simulated with MC generators. The centre-of-mass energy in all MC samples is assumed to be $\sqrt{s} = 7$ TeV. All event yields predicted from the MC generators are normalised to the luminosity of the data sample ($\int \mathcal{L} \mathrm{d}t = 4.7$ fb^{-1}).

The $t\bar{t}$ signal process is generated with PROTOS (PROgram for TOp Simulations), which is a LO Monte Carlo generator [59]. The cross-section is normalised to the exact NNLO (next-to-next-to leading order) QCD prediction including next-to-next-to leading logarithmic (NNLL) soft gluon terms, calculated with top++2.0 [97–102]. The cross-section amounts to $\sigma_{t\bar{t}} = 177.3^{+10.1}_{-10.8}$ pb^{-1} and the uncertainties include scale uncertainties, α_s uncertainties and PDF uncertainties. The used PDF set is the leading order CTEQ6L1 set [103]. PROTOS is the only generator at hand that is able to generate pure helicity states of the W-boson of F_0, F_L and F_R. The details concerning the PROTOS samples are summarised in Tab. A.1 in Sect. A.1. Further $t\bar{t}$ signal generators are used for the evaluation of systematic uncertainties (see Sect. 10.2). The default top-quark mass assumed is $m_t = 172.5$ GeV/c^2 for all generators.

The background processes are modelled by various generators: Single top-quark production is modelled with ACERMC [104] (t-channel production) and MC@NLO [105] (s-channel and associated production), diboson events are produced with HERWIG [87]. Z+jets and W+jets events were simulated using ALPGEN [106]. Both backgrounds have separate light flavour and heavy flavour samples, where heavy flavour samples are $W/Z + b\bar{b} + n$ partons, $W + c\bar{c} + n$ partons, $W + c + n$ partons. As well as samples with different parton multiplicity can overlap, also light and heavy flavour samples can overlap. For the former MLM [107] matching is applied, for the latter a heavy flavour overlap removal tool is devised to avoid phase space overlap between the different samples. The normalisation of the W+jets background is taken from data, the procedure is described in Sect. 7.2.1. Information on the background samples regarding the generator, showering, PDF sets and cross-sections and available statistics can be drawn from Tab. A.2, A.3, A.4 and Tab. A.5 in Appendix A.1.

All MC simulations have been interfaced to GEANT4 [95] for performing the detector simulation, except for the PROTOS samples that were processed by the ATLFAST II simulation tool [96].

7. Event Selection, Data Sample and Background Processes

This chapter gives an overview over the event selection performed, both in data and MC. It can be applied once the objects belonging to a certain event are identified. In this case, the standard $t\bar{t}$ selection in the ℓ+jets channel that is described in Sect. 7.1 is applied. The required background estimation for this particular event selection is described in Sect. 7.2. The data sample is described in Sect. 7.3. Relevant MC corrections for the 2011 data sample are briefly introduced in Sect. 7.4.

7.1. Event Selection

In the ℓ+jets channel, at least four jets, a charged lepton and $\not{E}_T$ are required. The charged lepton is either a muon or an electron. Leptonically decaying τ-leptons are included. The hadronic tau-decay is excluded and is included in the estimation of the multijet background (Sect. 7.2.2). The standard $t\bar{t}$ selection in the ℓ+jets topology performed in the ATLAS top physics group is as follows:
Requirements are:

- the appropriate single-electron or single-muon trigger has fired,

- exactly one isolated, high p_T electron or muon,

- the reconstructed lepton has to be matched to the trigger object fulfilling ΔR(offline lepton, trigger lepton)< 0.15,

- a good primary vertex with at least five associated tracks,

- no shared ID tracks of combined muon with a good electron,

- no bad jet,

- at least four jets with $p_T > 25$ GeV and $|\eta| < 2.5$ and JVF > 0.75,

- at least one b-tagged jet (70% working point, WP).

Further criteria depend on the lepton. The e+jets and μ+jets have the following, varying selection criteria:

e+jets channel:

- the electron p_T has to fulfil: $p_T > 25$ GeV,

- the pseudo-rapidity has to be $|\eta| < 2.47$, the crack region with $1.37 < |\eta| < 1.52$ is excluded,

- the missing transverse momentum is $\not{E}_T > 30$ GeV,

- the transverse mass of the W-boson[a] is required to be $m_T(W) > 30$ GeV.

μ+jets channel:

- the muon p_T has to fulfil: $p_T > 20$ GeV,

- the pseudo-rapidity has to be $|\eta| < 2.5$,

- the missing transverse momentum is $\not{E}_T > 20$ GeV,

- a triangular cut is performed: $\not{E}_T + m_T(W) > 60$ GeV.

Events that pass these criteria are kept as $t\bar{t}$ candidate events in the ℓ+jets channel. One can see that the cuts performed in the e+jets channel are tighter than for the μ+jets channel. This is intentional to keep the multijet background under control in the e+jets channel, where jets can easily be mistaken for electrons. In the next section, the estimation of the various background contributions to the selected data sample is discussed.

7.2. Background Estimation

Not only true $t\bar{t}$ events may be selected by the above described criteria. As discussed in Sect. 3.3, also background events enter the selected sample. These background events are estimated either from Monte Carlo simulation or from data-driven methods or a combination of both. The single top-quark, diboson and Z+jets events are estimated from MC predictions only. The shape of the W+jets background for various distributions is taken from MC, but the normalisation is derived using a data-driven method. The multijet background is estimated entirely from data. Both data-driven techniques are briefly described in the following.

7.2.1. W+jets Background

The estimation of the W+jets background is performed via the *charge asymmetry method*. This method exploits the fact that W^+- and W^--bosons are not equally produced at the LHC. The LHC is a *pp*-collider which leads to a higher production of W^+-bosons due to the PDFs of the proton that were described in Sect. 3.1: The main production mechanism of W-bosons is given by:

$$u + \bar{d} \to W^+ \quad \text{and} \quad \bar{u} + d \to W^-.$$

The valence quarks involved are the u- and the d-quark. Fig. 3.3 indicates that the momentum density of up-quarks is higher than the one of down-quarks, leading to $u + \bar{d} \to W^+$ being the process with the higher cross-section.

Other than the W+jets production, $t\bar{t}$, Z+jets and diboson production are charge symmetric processes, meaning an equal production of positively and negatively charged leptons. Also, the chance to misidentify jets as positively or negatively charged leptons should be the same. Since single top-quark production is also charge asymmetric, this process has to be subtracted from the event yields. Then, one can approximate:

$$N_{W^+} - N_{W^-} \approx D^+ - D^-.$$

---

[a] The transverse mass $m_T(W)$ of the W-boson is defined as: $m_T(W) = \sqrt{\vec{p}_T^2 - E_T^2}$. This term transfers to $m_T(W) = \sqrt{2p_T^\ell \not{E}_T (1 - \cos(\phi^\ell - \phi^\nu))}$ for the leptonic decay of the W and neglecting lepton masses.

N_{W^+} and N_{W^-} are the number of W^+- and W^--boson events in the signal sample and D^+ and D^- are the events with positively and negatively charged leptons in the signal sample. Using the well known ratio $r_{MC} = \frac{\sigma(pp \rightarrow W^+)}{\sigma(pp \rightarrow W^-)}$ and transforming $r_{MC} = \frac{N_{W^+}}{N_{W^-}}$ leads to:

$$N_{W^+} + N_{W^-} = \frac{r_{MC} + 1}{r_{MC} - 1}(N_{W^+} - N_{W^-})$$
$$\approx \frac{r_{MC} + 1}{r_{MC} - 1}(D^+ - D^-).$$

The left-hand side is the desired number of W+jets background events in the signal region. From this procedure, scale factors are derived to be multiplied with the yields from MC generators. The scale factors are derived for different regions with different jet and b-tag multiplicities.

W+heavy flavour jets

The above described procedure only determines the normalisation of the W+jets background but not the heavy flavour composition. The theoretical uncertainty on the fraction of $W + b\bar{b}$+jets, $W + c\bar{c}$+jets and $W + c$+jets and W+light jets is high and therefore again scale factors are derived from data to obtain the relative contributions to the overall yield. Dedicated methods are devised to obtain these four scale factors, selecting a phase space region, where the W+jets contribution is assumed to be dominant (at most two jets). The scale factors are derived there from data and extrapolated to the $t\bar{t}$ signal region. The method is described in [108].

7.2.2. Multijet Background

The name 'multijet background' implies that this background contains just jets. Jets can be mistaken for electrons due to a similar detector signature. Additionally, non-prompt muons originating from heavy quark decays inside a jet might be mistaken for prompt muons. To reject this background, certain quality criteria[b] are applied to lepton candidates which are sorted in categories. In this case, 'tight' criteria are applied to ensure that the lepton candidates are prompt leptons from direct boson decays. Nevertheless there is still a probability that jets and non-prompt leptons pass the selection criteria. This background is difficult to model with MC and therefore it is entirely derived from data using the so-called Matrix Method. Two event categories are defined, where the one is the signal region (N^{tight}) and the other is different only by requiring 'loose' lepton selection criteria instead of tight criteria (N^{loose}, it is expected to contain mainly misidentified leptons). The tight sample will be a subset of the loose sample, since it only differs by applying tighter cuts on isolation criteria. Then one can write:

$$N^{\text{loose}} = N^{\text{loose}}_{\text{real}} + N^{\text{loose}}_{\text{fake}},$$
$$N^{\text{tight}} = \epsilon_{\text{real}} N^{\text{loose}}_{\text{real}} + \epsilon_{\text{fake}} N^{\text{loose}}_{\text{fake}}.$$
(7.1)

In this system of equations $N^{\text{loose}}_{\text{real}}$ and $N^{\text{loose}}_{\text{fake}}$ are the numbers of events containing real and fake leptons that pass the loose selection criteria. The efficiency for real loose leptons to also pass the tight selection criteria is ϵ_{real}, the one for fake loose leptons is ϵ_{fake}. They are defined as

$$\epsilon_{\text{real}} = \frac{N^{\text{tight}}_{\text{real}}}{N^{\text{loose}}_{\text{real}}} \quad \text{and} \quad \epsilon_{\text{fake}} = \frac{N^{\text{tight}}_{\text{fake}}}{N^{\text{loose}}_{\text{fake}}}.$$
(7.2)

---

[b] The quality criteria include track and cluster criteria, isolation requirements etc., see e. g. [109].

Plugging the efficiencies of Eq. 7.2 into Eq. 7.1 and solving for the number of fake lepton events that pass the tight selection criteria, thus that enter the signal region, yields:

$$N_{\text{fake}}^{\text{tight}} = \frac{\epsilon_{\text{fake}}}{\epsilon_{\text{real}} - \epsilon_{\text{fake}}} \left(\epsilon_{\text{real}} N^{\text{loose}} - N^{\text{tight}} \right). \tag{7.3}$$

The efficiencies are obtained in control regions (for ϵ_{real} $Z \to \ell\ell$ events are used, for ϵ_{fake} multijet enriched control regions are used). Event weights can be calculated from Eq. 7.3 and applied to the loose and tight selections. The weight for the loose sample is obtained substituting $N^{\text{loose}} = 1$ and $N^{\text{tight}} = 0$:

$$w_{\text{loose}} = \frac{\epsilon_{\text{fake}}\epsilon_{\text{real}}}{\epsilon_{\text{real}} - \epsilon_{\text{fake}}}.$$

The tight event weights are obtained from Eq. 7.3 by substituting $N^{\text{loose}} = 1$ and $N^{\text{tight}} = 1$:

$$w_{\text{tight}} = \frac{\epsilon_{\text{fake}}(\epsilon_{\text{real}} - 1)}{\epsilon_{\text{real}} - \epsilon_{\text{fake}}}.$$

The tight weight w_{tight} will always be negative and w_{loose} is always positive. Applying these weights to selected data events thus allows to also model the multijet background shape and not only the normalisation as it is obtained in Eq. 7.3.

7.3. Data Sample

The analysed data has been collected by ATLAS in 2011 with a centre-of-mass energy of 7 TeV. The LHC delivered integrated luminosity is 5.5 fb^{-1} for 2011, the recorded luminosity is 5.25 fb^{-1} [76]. The data analysed in this thesis correspond to $\int \mathcal{L}\mathrm{d}t = 4.7$ fb^{-1}, reduced due to certain quality requirements on the recorded data and the respective beam conditions. Runs with stable beam conditions and good quality data are put on so-called *GoodRunLists* and these runs are finally considered for the analysis. The uncertainty on the luminosity amounts to 1.8% [76]. An information loss due to an electronics failure (LAr hole) in the 2011 run occurred where front-end boards (FEBs) were not accessible. They could be recovered later on. The missing FEBs could be appropriately simulated by MC. The mentioned phenomenon of pile-up can be quantified by the number of primary vertices in a single bunch crossing and the number of interactions per bunch crossing, which is denoted as μ. For 2011, the average number of interactions per bunch crossing was $\langle \mu \rangle = 9.1$ [75].

7.4. Monte Carlo Corrections

MC simulations have to be corrected to be able to describe actual data. First, the energy and momentum resolutions in the MC have to match the actual resolution in the data. This is done by 'smearing' the MC four-vectors accordingly. When smearing, the energy and momentum are convolved by a correction resolution function, the invariant mass of the particles has to stay the same. No smearing in MC for jets is needed, as the MC resolution matches the one in data. The described jet cleaning has to be applied, both in data and MC. The LAr hole has been well reproduced by MC simulations, so no events need to be cut away with jets lying in the LAr hole region. In addition to smearing, scale factors have to be applied (vastly p_T and η dependent). The efficiencies for b-tagging, lepton identification, reconstruction, trigger and isolation are different in MC and data and therefore the MC is corrected by applying scale

factors, which are the ratio of efficiency in data over efficiency in MC. Lepton energy scale offsets are corrected, this is done differently in GEANT4 and ATLFAST II processed samples. Muon efficiency scale factors depend on the run period and the smearing of combined muons is done separately in ID and MS measurement and then averaged over. All smearing, scale factor application and calibration has to be propagated to the $\not{E}_T$ variable afterwards. Finally, the MC has to be reweighted to match the average number of interactions $\langle \mu \rangle$ in data to account for pile-up.

7.5. Event Yields

Tab. 7.1 shows the event yields for the introduced standard $t\bar{t}$ event selection after all necessary corrections to the MC prediction have been applied. The contributions from all considered processes are shown for the e+jets and μ+jets channels. The total event prediction is compared to the observed number of events in data. The last row of the table shows the ratio of signal over background (S/B). The uncertainties on the MC predictions include statistical, luminosity, cross-section (for W+jets the uncertainty on the data-driven scale factors), JES, jet energy resolution (JER), b-tagging, lepton scale factor uncertainties and uncertainties related to the $\not{E}_T$ measurement (cell-out and pile-up). It can be observed that the MC prediction in the e+jets

	e+jets		**μ+jets**	
Process	Events	Uncertainty	Events	Uncertainty
$t\bar{t}$ (PROTOS)	18 469	2 424	28 010	3 508
Single top	1 204	165	2 005	247
W+jets	2 337	567	4 907	1 117
Z+jets	452	250	488	257
Diboson	47	12	74	17
Multijet	838	419	1 830	367
Total predicted	23 346	2 542	37 315	3 717
Observed	21 770		37 645	
S/B	3.79		3.01	

Table 7.1.: Number of events per process for e+jets and μ+jets channel for the standard $t\bar{t}$ selection (≥ 4 jets and ≥ 1 b-tag). The prediction is compared with the observed data. The ratio signal over background (S/B) is also shown.

channel overshoots the data, while the prediction in the μ+jets channel is close to the observed number of events. Nevertheless, the numbers are compatible with data in both channels within the uncertainties. The ratio S/B has a higher value for the e+jets channel, which means that this sample is purer, containing about 79% $t\bar{t}$ events while the μ+jets channels contains about 75% $t\bar{t}$ events. A higher purity also leads to fewer selected events. This is due to the tighter cuts applied in the e+jets channel event selection as described in Sect. 7.1 (e. g. higher p_T cut, tighter $\not{E}_T$ cut). Dileptonic $t\bar{t}$ events are included here and thus considered as signal rather than background. This is because these events also contain information on the W-helicity fractions.

7.5.1. Kinematic Distributions

In Fig. 7.1 and Fig. 7.2, kinematic distributions are shown for the e+jets and μ+jets channel, respectively. The MC predictions are compared to data, the ratio plots at the bottoms show the ratio of simulation over data. The yellow band contains statistical, cross-section (normalisation), luminosity, JES, JER, b-tagging and lepton scale factor uncertainties. The overshoot of MC in the e+jets channel is clearly visible in the distributions in Fig. 7.1, though the differences in normalisation are vastly covered by systematic uncertainties. This normalisation problem cannot be observed in the μ+jets channel. Apart from the normalisation, also shape modelling problems occur in both channels: the jet η and lepton η distributions are narrower in MC than in data. This is a known problem of LO generators and is not observed for the default $t\bar{t}$ sample from POWHEG+PYTHIA (see Fig. A.1 and Fig. A.2 in the appendix). The lepton E_T distribution is also badly described by MC for the high E_T region. There, the MC overshoots the data in both channels. Another modelling issue is related to the b-tag multiplicity. All $t\bar{t}$ generators reveal problems in describing this distribution. The MC shape does not match the data well, but deviations are covered by systematic uncertainties. Conclusively, it can be stated that there are modelling issues concerning the normalisation in the e+jets channel, lepton E_T modelling, lepton and jet η modelling and the b-tag multiplicity. Nevertheless, deviations to data are not dramatical, the data is understood well enough to perform the analysis and known systematic uncertainties can explain the observed discrepancies.
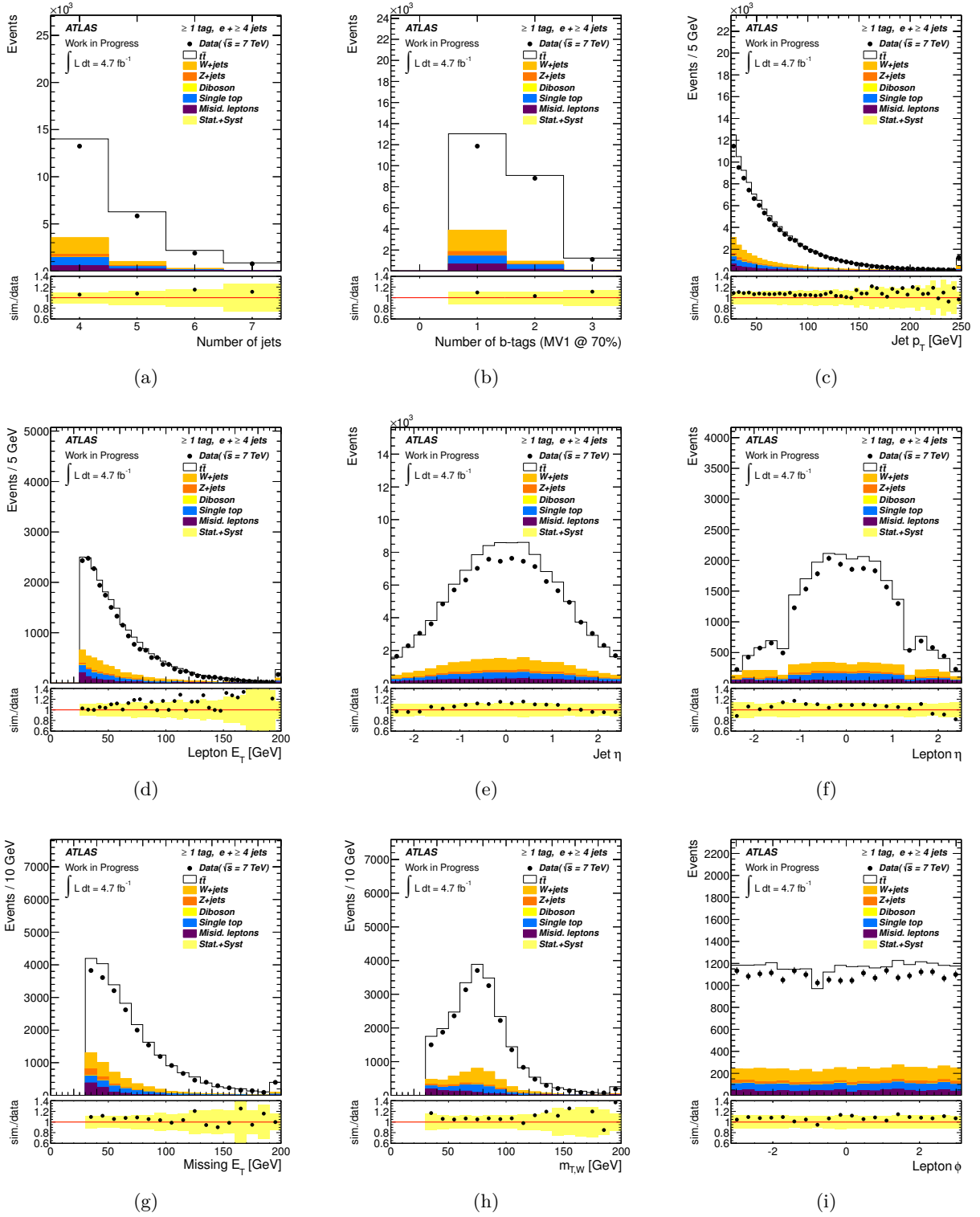
Figure 7.1.: Kinematic distributions in the e+jets channel for standard $t\bar{t}$ selection with PROTOS $t\bar{t}$ simulation. The uncertainty band in the ratio plots includes statistical, cross-section, luminosity, JES, JER, b-tagging, lepton scale factor uncertainties.
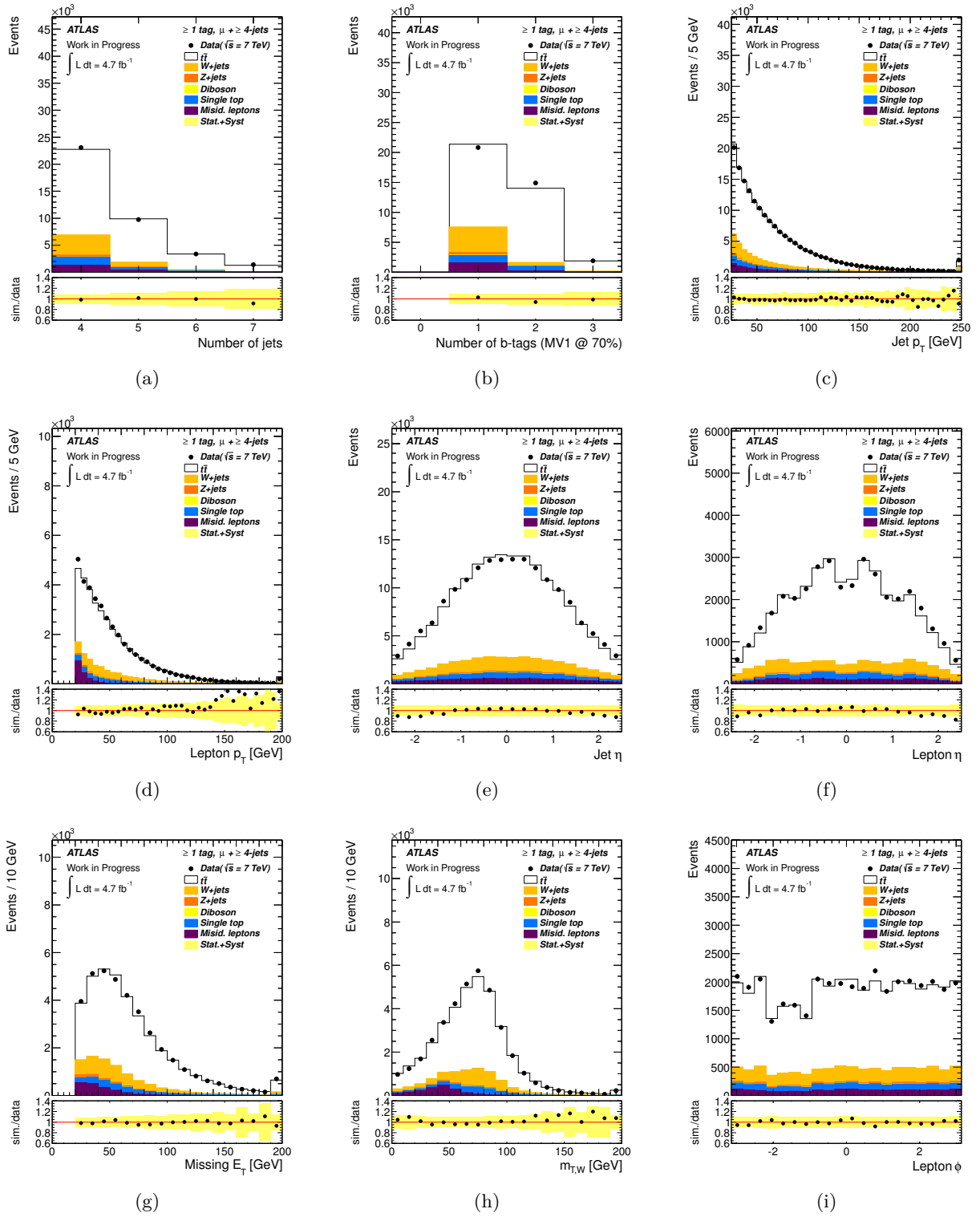
Figure 7.2.: Kinematic distributions in the μ+jets channel for standard $t\bar{t}$ selection with PROTOS $t\bar{t}$ simulation. The uncertainty band in the ratio plots includes statistical, cross-section, luminosity, JES, JER, b-tagging, lepton scale factor uncertainties.

8. Analysis Strategy

This chapter describes the analysis strategy to measure the W-helicity fractions in data. After the event selection, the full $t\bar{t}$ event is reconstructed using a kinematic likelihood fitter, described in Sect. 8.1. A template method is used to extract the helicity fractions from the reconstructed $\cos\theta^*$ distribution as described in Sect. 8.2.2. Crucial for a precision measurement is the evaluation of uncertainties. Two ways to evaluate systematic uncertainties are described in Sect. 8.3.1 and Sect. 8.3.2, respectively. Both methods will be used to perform the full analysis and will be compared to each other.

8.1. Event Reconstruction with the Kinematic Likelihood Fitter

After the event selection, the $t\bar{t}$ pairs have to be fully reconstructed in order to determine the angular variable $\cos\theta^*$. In the ℓ+jets channel, this means to reconstruct all four-momenta of the four quarks, the lepton and the neutrino, and to correctly associate the decay products to the leptonic and hadronic top-quark. Therefore, a kinematic likelihood approach is used which is implemented in the Kinematic Likelihood Fitter package (KLFitter) [110, 111]. The KLFitter takes as input the four hardest jets[a] of an event and assumes that other present jets originate from soft gluon radiation (initial state radiation or underlying event activity). These four leading jets have to be associated to the four quarks coming from the $t\bar{t}$ decay, where two of these jets are expected to be b-jets and the others to be light jets from a W-boson decay. Thus, from combinatorics, there are 24 possibilities to associate the four jets to the four quarks. As no distinction is made between the two light jets from the W-boson, twelve possibilities remain. The KLFitter now calculates the likelihood, seen in Eq. 8.1, and takes the permutation that maximises this likelihood as the correct permutation.

$$
\begin{aligned}
L = \ & \text{BW}(m_{q\bar{q}'}|m_W, \Gamma_W)\text{BW}(m_{\ell\nu}|m_W, \Gamma_W) \\
& \cdot \text{BW}(m_{q\bar{q}'b_{\text{had}}}|m_t, \Gamma_t)\text{BW}(m_{\ell\nu b_{\text{lep}}}|m_t, \Gamma_t) \\
& \cdot \text{W}\left(\tilde{E}_{\text{jet}_1}|E_{b_{\text{had}}}\right) \text{W}\left(\tilde{E}_{\text{jet}_2}|E_{b_{\text{lep}}}\right) \text{W}\left(\tilde{E}_{\text{jet}_3}|E_q\right) \\
& \cdot \text{W}\left(\tilde{E}_{\text{jet}_4}|E_{\bar{q}'}\right) \text{W}\left(\tilde{\slashed{E}}_x|p_{x,\nu}\right) \text{W}\left(\tilde{\slashed{E}}_y|p_{y,\nu}\right) \\
& \cdot \left\{ \begin{array}{ll} \text{W}\left(\tilde{E}_\ell|E_\ell\right), & \text{electron channel} \\ \text{W}\left(\tilde{p}_{T,\ell}|p_{T,\ell}\right), & \text{muon channel} \end{array} \right\}
\end{aligned}
\tag{8.1}
$$

The likelihood L takes the following into account: As can be seen from Fig. 3.6, the invariant mass of two jets originating from q and $\bar{q}'$ has to correspond to the W-boson mass. Accordingly, the Breit-Wigner functions of the W-boson mass m_W and the width Γ_W from the W-boson propagator enter the likelihood, where the term $\text{BW}(m|m_i, \Gamma_i)$ expresses the probability to measure an invariant mass m, when the mother particle has a mass m_i and a decay width Γ_i. The same applies to the lepton ℓ and the neutrino ν whose invariant mass $m_{\ell\nu}$ has to be Breit-Wigner distributed around the W-boson mass. This constraint gives information on the neutrino p_z

---

[a] If the four hardest jets do not include a b-jet, then the hardest b-jet is taken instead of the fourth leading jet.

momentum component that cannot be measured. After reconstructing the W-bosons from the decay, the hadronic and leptonic top-quark are built simultaneously by requiring the invariant masses of hadronic b-jet (b_{had}) and hadronic W-boson to be Breit-Wigner distributed around the top-quark mass and the same for the leptonic top-quark of the $t\bar{t}$ event. In this analysis the KLFitter is used with a fixed top-quark mass of 172.5 GeV.

The next part of the likelihood contains so-called transfer functions W. These functions take the finite detector resolution into account and describe the probability of measuring an energy $\tilde{E}$ when the truth energy of an object was E. These transfer functions were derived using a sample simulated with the MC@NLO generator and are parameterised by double Gaussians depending on $\Delta E = (E_{\text{truth}} - E_{\text{reco}})/E_{\text{truth}}$ for different p_T and η regions [111]. It is assumed that the azimuthal angle ϕ and pseudo-rapidity η are measured precisely. For the missing energy the x- and y- components are compared to the neutrino p_x and p_y components. For the muon channel the p_T of the muon is used in the respective muon transfer function.

Finally, a b-tag weight $w_{b\text{-tag}}$ is multiplied to the *event probability* to take information of b-tagging into account. The event probability is calculated by dividing the likelihood of a certain permutation by the sum of L for all permutations. The b-tag weight is constructed such that it favours solutions for which the jets associated to b-partons are actually b-tagged and associated light jets are not b-tagged. It disfavours solutions with the assignments where a non-b-tagged jet takes the place of a b-parton and a b-tagged jet takes the place of a light quark. Thus, the tagging efficiency ε and the rejection rate R [b] enter the weight $w_{b\text{-tag}}$ that takes the form

$$w_{b\text{-tag}} = \left\{ \begin{array}{c} \varepsilon, \text{ if } b_{\text{had}} \text{ is } b\text{-tagged} \\ (1-\varepsilon), \text{ if } b_{\text{had}} \text{ is not } b\text{-tagged} \end{array} \right\} \cdot \left\{ \begin{array}{c} \varepsilon, \text{ if } b_{\text{lep}} \text{ is } b\text{-tagged} \\ (1-\varepsilon), \text{ if } b_{\text{lep}} \text{ is not } b\text{-tagged} \end{array} \right\} \times$$
$$\left\{ \begin{array}{c} 1/R, \text{ if } q \text{ is } b\text{-tagged} \\ (1-1/R), \text{ if } q \text{ is not } b\text{-tagged} \end{array} \right\} \cdot \left\{ \begin{array}{c} 1/R, \text{ if } \bar{q}' \text{ is } b\text{-tagged} \\ (1-1/R), \text{ if } \bar{q}' \text{ is not } b\text{-tagged} \end{array} \right\}.$$

To maximise L the logarithm $\ln L$ is maximised. The best permutation found from the likelihood maximisation gives the correct jet parton assignment in about 70% of the cases. This has been studied using truth information of the MC samples [111].

After the reconstruction of all four-momenta of the partons present in the ℓ+jets channel it is possible to calculate $\cos\theta^*$. Therefore the four-momenta of ℓ and ν are added to give the four-momentum of the leptonically decaying W-boson. Then the four-momenta of the leptonic b-quark and the lepton ℓ can be Lorentz-transformed to the rest frame of the leptonic W-boson. Finally $\cos\theta^*$ is calculated by determining the angle between the lepton direction and the negative b-quark direction (see Fig. 3.8(a)). The same can be done for the hadronically decaying top-quark. In this analysis, only the calculated angle from the leptonic system is used as no distinction between up- and down-type quarks from the hadronically decaying W-boson is made.

8.2. Statistical Tools

This section introduces the relevant statistical concepts for the W-helicity analysis. The *template method* is utilised to determine the helicity fractions from data. It relies on the *maximum likelihood method* and incorporates prior information on background contributions. The maxi-

---

[b] $1/R$ is the probability to tag non-b-jets, for the MV1 tagger R is 134.

mum likelihood method is briefly introduced in the following. The template method is described in more detail in Sect. 8.2.2.

8.2.1. Maximum Likelihood Method

The maximum likelihood method is a way to estimate unknown parameters from a certain dataset[c]. The method is ascribed to R. A. Fisher, 1912 [112, 113] (not knowing of groundwork by C. F. Gauß). Assume a dataset with $\boldsymbol{x} = \{x_1, x_2, \ldots x_N\}$ from N measurements is given. The set of the unknown parameters to be estimated is denoted by $\boldsymbol{\xi} = \{\xi_1, \xi_2 \ldots\}$. The different x_i are statistically independent and distributed according to a parent distribution (probability density function, pdf) $P(x_i|\boldsymbol{\xi})$. The likelihood $\mathcal{P}$ is then defined as the product of the pdf's of each x_i:

$$\mathcal{P}(\boldsymbol{x}|\boldsymbol{\xi}) = \prod_{i=1}^{N} P(x_i|\boldsymbol{\xi}). \tag{8.2}$$

Thus, Eq. 8.2 represents the probability for a certain set of $\boldsymbol{\xi}$ to explain the measured data $\boldsymbol{x}$. The best estimate for $\boldsymbol{\xi}$ is given by $\hat{\boldsymbol{\xi}}$ which maximise the likelihood $\mathcal{P}$. In complex cases, the expression in Eq. 8.2 may be difficult to handle by computing tools and therefore often the negative logarithm of the likelihood is used, that contains sums rather than products:

$$-\ln \mathcal{P}(\boldsymbol{x}|\boldsymbol{\xi}) = -\sum_{i=1}^{N} \ln P(x_i|\boldsymbol{\xi}). \tag{8.3}$$

Here, the expression in 8.3 needs to be minimised to find the best parameter estimate $\hat{\boldsymbol{\xi}}$. The minimisation is often carried out numerically by tools like MINUIT [114].

8.2.2. The Template Method

In this analysis, the W-helicity fractions F_0, F_L and F_R are extracted from the $\cos\theta^*$ distribution by performing a template fit to the data distribution.

Let $\cos\theta^*$ be the variable x, whose distribution is filled into a histogram with n_b bins with a width of Δx_j. The distribution consists of unknown contributions from i different processes. In our case, these processes are the three signal processes F_0, F_L and F_R, and three background processes. The W+jets and the multijet background are regarded as separate processes whereas the backgrounds from single top-quark, diboson and Z+jets production are merged into one process that is called 'remaining background'. The goal is now to estimate the contributions to the x distribution for these six considered processes. The contribution is expressed by the model parameter N_i^p for each process i. Each process has a probability density $f_i(x)$ depending on x that is obtained by frequency distributions from Monte Carlo. These are normalised to unity and are referred to as *templates*. The expectation value N_j for each bin j is calculated as seen in Eq. 8.4, where n_p is the number of processes [115]:

$$N_j = \sum_i^{n_p} N_i^p \int_{\Delta x_j} f_i(x)\mathrm{d}x. \tag{8.4}$$

---

[c] The maximum likelihood method can also be utilised for hypothesis testing besides parameter estimation.

This term can be rewritten separating the expectation values into signal and background. For the signal templates the different selection efficiencies ϵ_i have to be taken into account to get the original amount of signal events before applying any cuts. Thus, Eq. 8.4 transforms to:

$$N_j = \sum_{i=0,L,R} N_i^p \cdot \epsilon_i \int_{\Delta x_j} f_i(x)\mathrm{d}x + \sum_{i=\mathrm{bkg}} N_i^p \cdot \int_{\Delta x_j} f_i(x)\mathrm{d}x. \qquad (8.5)$$

The first term of Eq. 8.5 describes the signal and the second term the background contribution, indicated by $i = \mathrm{bkg}$.

The observed number d_i in each bin is assumed to fluctuate around the expected value N_i according to a Poisson-distribution, where the bins are assumed to be independent. Thus, the likelihood $\mathcal{P}$ to be fitted to the data is formed to be

$$\mathcal{P}\left(\vec{N}\right) = \prod_i^{n_b} \frac{N_i^{d_i}}{d_i!} \cdot \mathrm{e}^{-N_i}, \qquad (8.6)$$

where $\vec{N} \equiv \{N_i\}$. The likelihood in Eq. 8.6 is a product of Poisson-terms for each bin. No prior knowledge about $N_i^p \int f_i(x)\mathrm{d}x$ is assumed for the helicity fractions as these are the parameters of interest. For the background contributions a Gaussian prior is assumed, where $N_{\mathrm{B},j}$ and $N_{\mathrm{B,exp},j}$ are the observed and expected number of events for the background j, respectively and $\sigma_{\mathrm{B,exp},j}$ is the expected uncertainty on the former number. The final likelihood modifies to:

$$\mathcal{P}\left(\vec{N}\right) = \prod_{i=1}^{n_b} \frac{N_i^{d_i}}{d_i!} \cdot \mathrm{e}^{-N_i} \cdot \prod_{j=1}^{n_{\mathrm{bkg}}} \frac{1}{\sqrt{2\pi}\sigma_{\mathrm{B,exp},j}} \exp\left(\frac{(N_{\mathrm{B},j} - N_{\mathrm{B,exp},j})^2}{2\sigma_{\mathrm{B,exp},j}^2}\right); \qquad (8.7)$$

the Gaussian constraint on the background contributions shows up in the second product. The best model parameters, $\hat{N}_i$, are extracted by maximizing the likelihood in Eq. 8.7. The helicity fractions are obtained by

$$F_i = \frac{\hat{N}_i}{\hat{N}_0 + \hat{N}_L + \hat{N}_R}, \quad \text{for} \quad i = 0, L, R. \qquad (8.8)$$

The template fit is performed based on the MINUIT package [114] within the ROOT framework [116]. MINUIT provides the statistical uncertainties on the fitted parameters. They are calculated via the *Hesse* algorithm[d]. As can be seen from Eq. 8.8, the parameters N_i are correlated: N_L and N_R are highly correlated while the pairs N_L, N_0 and N_R, N_0 are highly anti-correlated. This correlation has to be taken into account to calculate the final statistical uncertainties on the fitted fractions. The correlations amongst the variables can be obtained by performing ensembles tests and plotting the quantities N_i as functions of each other. The ensemble testing procedure is explained in Sec. 8.3.1. In this analysis, the correlation matrix is provided by MINUIT. Then, a covariance matrix can be calculated:

$$V = \begin{pmatrix} \sigma_{N_L}^2 & \sigma_{N_0}\sigma_{N_L}\varrho(N_0, N_L) & \sigma_{N_R}\sigma_{N_L}\varrho(N_R, N_L) \\ \sigma_{N_L}\sigma_{N_0}\varrho(N_L, N_0) & \sigma_{N_0}^2 & \sigma_{N_R}\sigma_{N_0}\varrho(N_R, N_0) \\ \sigma_{N_L}\sigma_{N_R}\varrho(N_L, N_R) & \sigma_{N_0}\sigma_{N_R}\varrho(N_0, N_R) & \sigma_{N_R}^2 \end{pmatrix}.$$

---

[d] The Hesse algorithm relies on the Hesse-matrix consisting of second derivatives of the likelihood w.r.t. the fitted parameters. The inverse Hesse-matrix is the covariance matrix used for error propagation.

The matrix elements of V have to be multiplied by derivatives $\partial F_i / \partial N_k$ from both sides to obtain the final statistical uncertainty from the template fit:

$$\sigma_{F_i}^2 = \sum_k \sum_l \frac{\partial F_i}{\partial N_k} \frac{\partial F_i}{\partial N_l} \sigma_{N_k} \sigma_{N_l} \varrho(N_k, N_l) \quad \text{for} \quad i = 0, L, R. \tag{8.9}$$

The sum is calculated with $k, l = 0, L$ and R.

8.3. Evaluation of Systematic Uncertainties

With the above described template method, one is able to determine the helicity fractions and the statistical uncertainty on these. The statistical uncertainty will also contain the uncertainties on the background normalisation. The goal of the analysis is to decrease the total uncertainty and therefore improve the precision compared to previous measurements that have been shown in Sect. 3.4.2. Compared to the previous ATLAS measurement (Eq. 3.7), the data set is increased by more than a factor of four and therefore the statistical uncertainty is expected to decrease. To decrease the systematic uncertainties, techniques have to be developed and refined in order to understand the various systematic sources and to be able to decrease the impact of these sources on the measurement. In the analysis in [58] (ATLAS), systematic uncertainties were estimated by performing *ensemble tests*. The next section will describe this procedure. A promising method to estimate and decrease systematic uncertainties is performing a *profile likelihood fit*. The method of 'profiling' will be described in Sect. 8.3.2.

8.3.1. Ensemble Tests

For the evaluation of systematic uncertainties via ensemble tests, pseudo-data sets are created. In general, pseudo-data sets are derived by adding the contributions of background and signal processes predicted by Monte Carlo generators, or in case of the W+jets and multijet background by adding the yields from the data-driven methods. Pseudo-data sets for systematic sources are created by varying the MC prediction by the uncertainty of the source by one standard deviation up $(+1\sigma)$ and one standard deviation down $(-1\sigma)^{\mathrm{e}}$. From the obtained pseudo-data, *ensembles* are created by fluctuating the bin contents within Poissonian probability. Single fits for each ensemble are performed and the fitted parameter values are written into a histogram. Thus, by performing ensemble tests, one obtains parameter distributions around a mean value with a Gaussian shape. The W-helicity fractions are then calculated by:

$$F_i = \frac{\langle N_i \rangle}{\langle N_0 \rangle + \langle N_L \rangle + \langle N_R \rangle}, \quad \text{for} \quad i = 0, L, R. \tag{8.10}$$

$\langle N_i \rangle$ is the mean of the parameter distribution of $N_i, i = 0, L, R$ for the various ensembles. The differences between the calculations with nominal ensembles and $\pm 1\sigma$ systematic varied ensembles is taken as the systematic uncertainty due to the systematic source. If the differences are asymmetric, the larger value is taken as overall systematic uncertainty. An example of this procedure is illustrated in Fig. 8.1: The source of systematic uncertainty considered here is the jet energy scale (JES) envelope. The influence on the fit is clearly visible in Fig. 8.1, where a higher JES leads to a larger N_0 and a lower JES leads to a lower N_0 compared to the nominal mean value. These systematic influences are propagated to the W-helicity fractions according to Eq. 8.10.

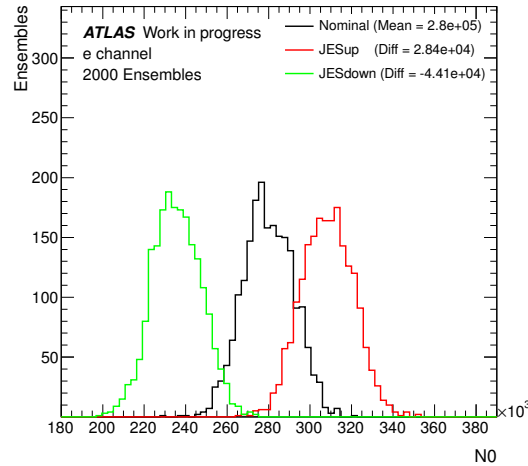e Also, sometimes just two different MC predictions are compared. Details are given in Sect. 10.2

Figure 8.1.: Example for the evaluation of systematic uncertainties via $2\,000$ ensemble tests: Shown is the parameter distribution for N_0 for ensemble tests with nominal pseudo-data and 1σ up and down varied pseudo-data from the JES systematic samples.

8.3.2. Profile Likelihood Method

The procedure of performing a profile likelihood fit is more dynamic than the above described ensemble testing method. Basically, the profile likelihood fit is a template fit that incorporates additional *nuisance parameters k*, that account for influences from systematic sources. Eq. 8.11 shows the negative logarithm of the profile likelihood.

$$-2\ln(\mathcal{P}) = 2\sum_{m=1}^{n_b}\left(N_m - d_m \cdot \ln(N_m)\right) + \sum_{i=1}^{n_{\text{bkg}}}\frac{(N_{B,i} - N_{B,\exp,i})^2}{\sigma^2_{N_{B,\exp,i}}} + \sum_{j=1}^{N_{\text{prof}}}k_j^2 + \text{const.} \qquad (8.11)$$

Comparing this expression to Eq. 8.7, the first sum on the right-hand side turns out to come from the product of Poisson-terms and the second sum is due to the Gaussian constraint on the background. The last sum is new and is the one, which includes the nuisance parameters k. In the likelihood function, these are implemented in a Gaussian term with a mean of 0 and a standard deviation of 1. The intention is to describe a 'template morphing' due to systematic uncertainties with the help of the parameters k. The number N of entries in a certain bin and a certain template becomes a function of k, $N \equiv N(k)$. Thus, in the profile likelihood fit, the fit is able to adjust the shape of the templates according to the data. The profiling procedure tries to extract the information about systematic influences from the data itself. Only continuous systematics are suited for a profile likelihood fit and correlations among different systematics have to be understood. For the template morphing, each template and each bin of the $\cos\theta^*$ distribution have to be considered separately. A systematic variation of $+(-)1\sigma$ is associated to $k = +(-)1$, the nominal value is associated to $k = 0$. The situation is illustrated in Fig. 8.2. The number of entries in a certain template in a certain bin is shown as a function of k. The black curve shows a certain interpolation that has to be performed between the three points in order to describe a continuous morphing of the templates. The green histograms show an example for such a morphing depending on k. In the case of three known points, often a *quadratic inter-*
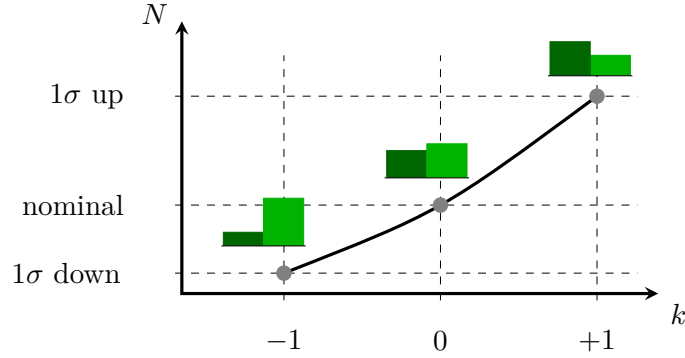
Figure 8.2.: Illustration of the procedure of 'template morphing'. Explanation is given in the text. Adapted from [117].

polation is performed between these. Thereby the nominal value $N(0)$ is fixed (no uncertainty on this value) and a parabola is fitted that goes through all three points. Beyond $|k| > 1$ a linear extrapolation is used where the slope of $N(|k| = 1)$ is adapted to the linear function. The information from $\pm 1\sigma, \pm 2\sigma$ and $\pm 3\sigma$ variations due to systematic sources may in some cases be also available. In this case, seven points characterise $N(k)$. Studies have shown that the best interpolation method then is the quadratic fit [118]. The nominal entry is fixed and a parabola is fitted to all points. An example for this procedure is shown in Fig. 8.3. Again, the jet energy scale is taken as the example systematic component. In Fig. 8.3(a) the F_0 template is shown for the nominal sample (black) and the JES systematic varied samples for $\pm 1\sigma$, $\pm 2\sigma$ and $\pm 3\sigma$ in the e+jets channel. As described before, each bin is considered separately, here bin 12 is shown in Fig. 8.3(b). The number of entries from the different samples is now a function of k by the respective association of the samples to a k value. Different interpolation methods are shown. The ratio plots show the agreement of the MC data points with the fitted curves. The red curve belongs to the quadratic fit, which is utilised in the case of systematic variations up to $\pm 3\sigma$. This interpolation method is the only one that takes the information of all seven points into account and describes these points best, as can be seen in the ratio plots in Fig. 8.3(b).

It is expected that the evaluation of systematic uncertainties via a profile likelihood fit will decrease some uncertainties on the measurement as the profiling method is able to adjust these uncertainties to the measured data in a dynamic way. The profile likelihood fit will be sensitive to a certain nuisance parameter if the respective systematic source causes a shape variation in $\cos \theta^*$. This sensitivity can be directly seen from the fit output that would exhibit a standard deviation of k below one. The profile method is not static, relying on the input from discrete $\pm 1\sigma$ variations like the ensemble testing. Of course, performing a profile likelihood fit introduces a lot of more degrees of freedom in the template fit, which may cause instabilities in the fit results. This is checked by performing ensemble tests with pseudo-data. A possible bias in the method can be identified by producing so-called 'calibration curves'. These are obtained from plotting output parameters as a function of input parameters that are varied in a certain range. If the slope of the curve is compatible with 1 and the intercept is compatible with 0, then no bias is detected and no further calibration is needed.

The method validation is performed in [118] and will be discussed here in one case: The final profile likelihood analysis as presented in Sect. 10.3 includes 29 nuisance parameters into the
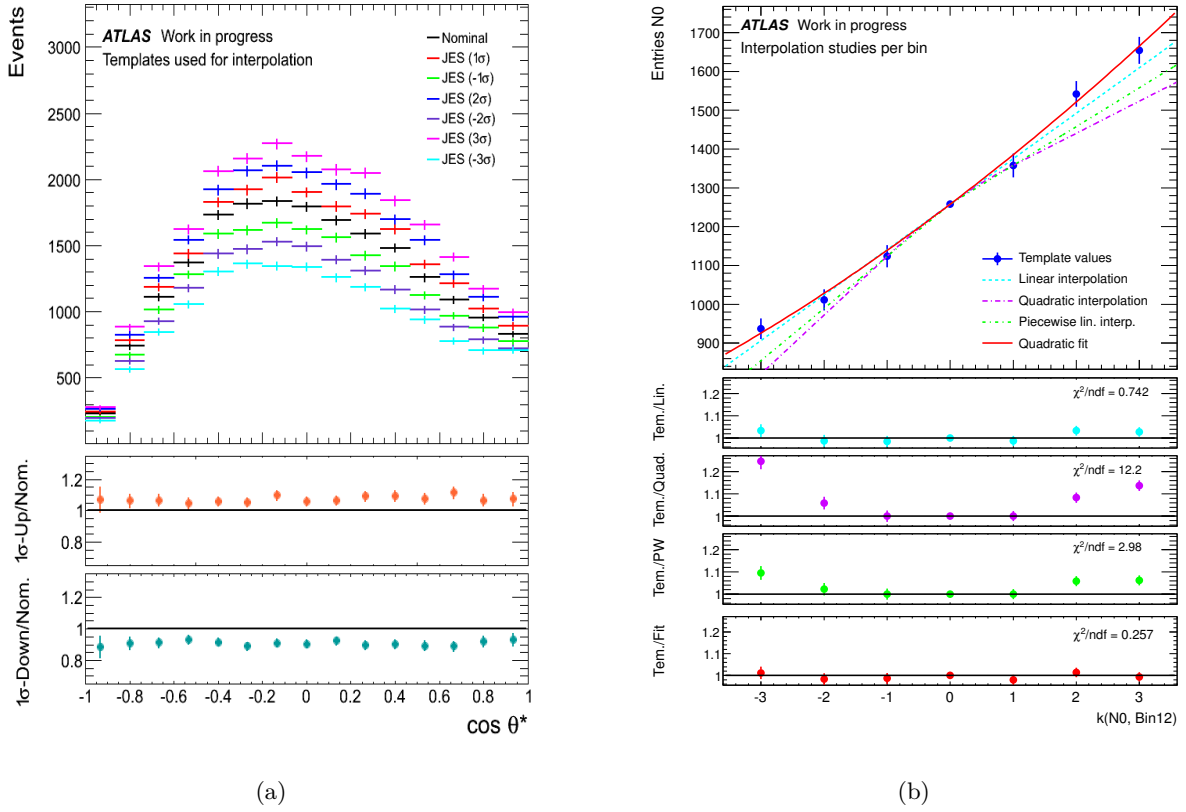
(a)

(b)

Figure 8.3.: Example for interpolation strategies for profiling for the global JES uncertainty and the F_0 template. (a) shows the F_0 template for the nominal sample and JES systematic varied samples (e+jets channel). (b) shows bin 12 of distribution (a) and several interpolation methods for $N(k)$. The reduced χ^2 values indicate that the quadratic fit describes the given points best.

data fit. Calibration curves for this setup are obtained by producing pseudo-data with varying input values F_0. F_R is fixed to zero and F_L varies with $1 - F_0$. Always $2\,000$ ensembles are created for pseudo-data sets with $F_0 = 0.5, 0.6, 0.7, 0.8$ and 0.9. The resulting output helicity fractions are obtained according to Eq. 8.10. They are plotted as a function of the input F_0 in Fig. 8.4. A linear fit to the F_0 data points is shown as well. The fitted intercept and offset are in agreement with the expectation. The bottom plot of Fig. 8.4 shows the difference between the input and output helicity fractions. Small deviations from zero are observed but are at most 0.3%. No further calibration of the profile likelihood analysis is needed.
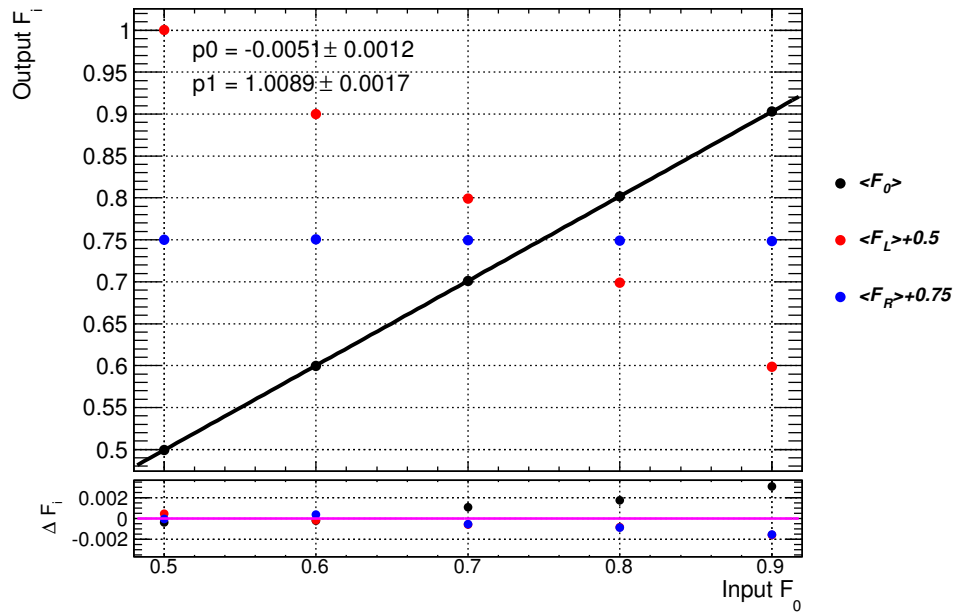
Figure 8.4.: Calibration curves for a profile likelihood fit with 29 nuisance parameters to pseudo-data. The data points were obtained from 2 000 ensemble tests to the pseudo-data from the input values F_i. F_R is fixed to zero, F_0 varies between 0.5 and 0.9, F_L is always $1 - F_0$. A linear curve is fitted to the F_0 data points, the fitted intercept (p0) and slope (p1) are displayed in the plot.

9. Optimisation Studies

In this chapter, optimisation studies are presented that should lead to a more precise measurement of the W-helicity fractions. The studies comprise the use of a profile likelihood fit as well as general changes in the fit setup. Studies dealing with statistical uncertainties are shown in Sect. 9.1. The treatment of systematic uncertainties is presented in Sect. 9.2.

9.1. Statistical Uncertainties

The limited statistics in data and MC samples play an important role for both, the evaluation of statistical uncertainties of the template fit and systematic uncertainties. First, studies of the influence of the binning of the $\cos\theta^*$ distribution on the statistical uncertainty in the template fit are presented, then a setup that is able to decrease the statistical uncertainty of the estimators in the likelihood fit is presented.

9.1.1. Binning of the $\cos\theta^*$ Distribution

The template fit as performed in the latest ATLAS publication [58] used 15 bins in $\cos\theta^*$ with equal bin widths. The signal templates are shown in Fig. 3.9(a). These templates have shapes that can be easily identified with the analytical curves in Fig. 3.8(b) for pure helicity states $F_i, i = 0, L, R$. The templates are a little bit distorted due to acceptance effects from the event selection and imperfect detector resolution (performed studies shown in [119]). The binning of the angular distribution has an influence on the statistical uncertainty of the likelihood estimators. Less bins meaning less shape sensitivity is expected to lead to a higher statistical uncertainty of the fit. For a profile likelihood fit, it is important that the relative statistical uncertainty per bin ($\Delta N/N$) is reasonably small. Otherwise, one might parameterise statistical fluctuations of the bin contents as $N(k)$ and not real systematic effects. To illustrate this effect, an example in Fig. 9.1 is shown with the original binning with 15 bins. The relative statistical uncertainty per bin are shown for the F_0 template in the e+jets channel as the black line. This belongs to the nominal template. In Fig. 9.1, the relative deviations of the systematic varied templates is shown as coloured lines. The relative deviation is defined as:

$$\text{relative deviation} = \frac{\text{bin entry(syst.)} - \text{bin entry(nominal)}}{\text{bin entry(nominal)}}.$$

The systematic sources shown are the *flavour composition* (Fig. 9.1(a)) and *single-particle-high-p_T* (Fig. 9.1(b)), which are both components of the jet energy scale. For the flavour composition, the systematic deviations from the nominal template are almost always larger than the relative statistical uncertainty per bin, whereas for the single-particle-high-p_T component all deviations are covered by the relative statistical uncertainty. They are thus likely to be statistical fluctuations only. In this case, it is not sensible to profile this component. An approach to decrease the relative statistical uncertainty per bin and to clearly identify systematic sources that contribute real systematic effects on $\cos\theta^*$ is to change the binning of the $\cos\theta^*$ distribution. The goal is to find a trade-off value for the relative statistical uncertainty that is undershot by each bin in
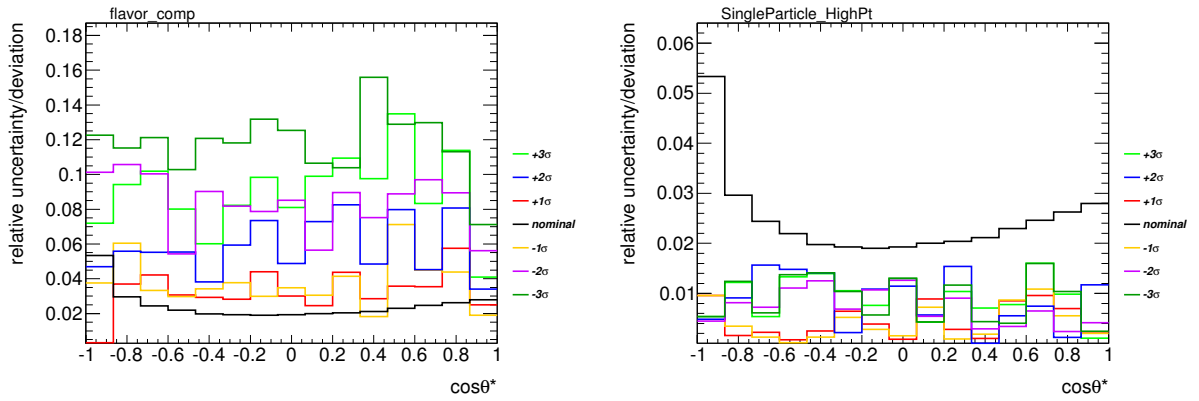
Figure 9.1.: Comparison of relative uncertainty per bin (black line) with the relative deviation of systematic varied samples to the nominal sample for the F_0 template (only absolute values for the relative deviation were calculated here). The left side shows the flavour composition, the right side the 'single-particle-high-p_T' component.

each template. This value is chosen to be 5%. It is a compromise between decreasing relative uncertainties from the MC samples and increasing the statistical uncertainty on the likelihood estimators in the data fit. The binning is adjusted such that the 5% criterion is matched by each bin in each template. In a first approach, the bin number is decreased to eight. Studies have shown that the limiting factor is the W+jets template in the e+jets channel which suffers from low template statistics. The relative statistical uncertainty per bin for this template is shown in
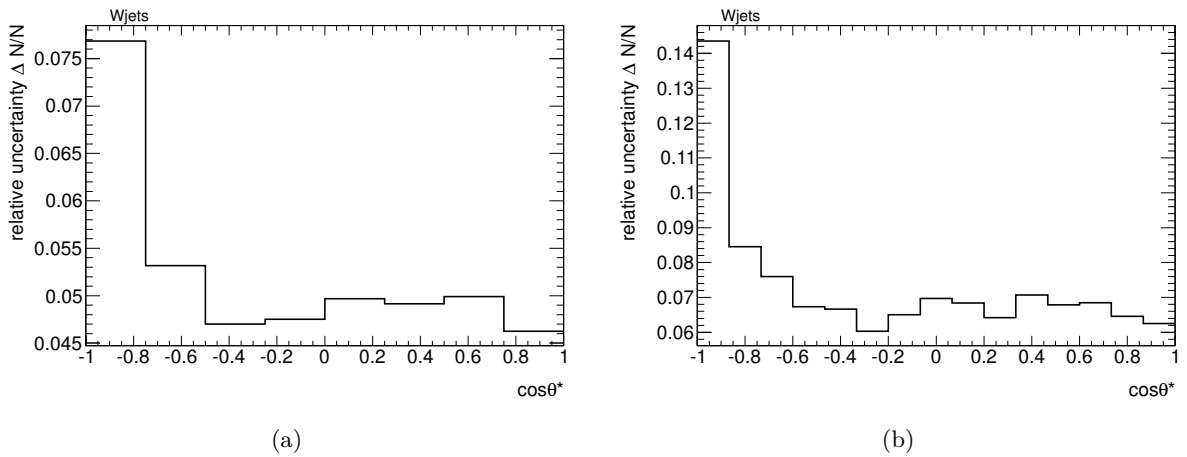

(a)

(b)

Figure 9.2.: Relative statistical uncertainty per bin of the W+jets template for eight bins with equal bin width (a) and 15 bins with equal bin width.

Fig. 9.2 for eight bins (a) and 15 bins (b). Compared to 15 bins, the eight bins have significantly reduced uncertainties, but the first bin exceeds 5%. For this reason, the first two bins have been merged into one bin that has now twice the width of the other bins. The respective plots for all templates in e+jets and μ+jets channel are shown in Fig. 9.3 and Fig. 9.4. The multijet template is also shown, but the relative statistical uncertainties are irrelevant here, because this
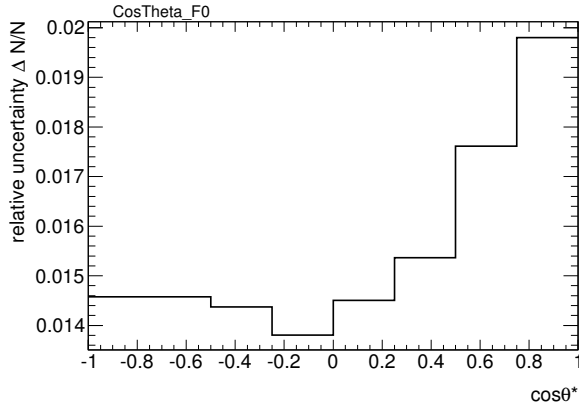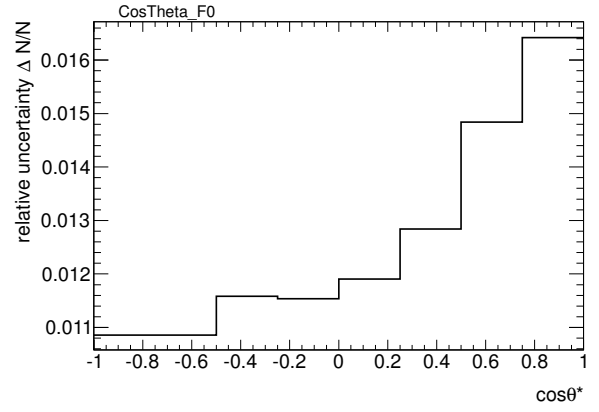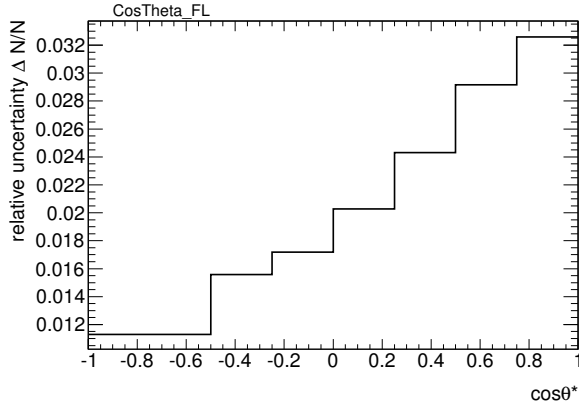
(a) F_0 template, e+jets

(b) F_0 template, μ+jets

(c) F_L template, e+jets
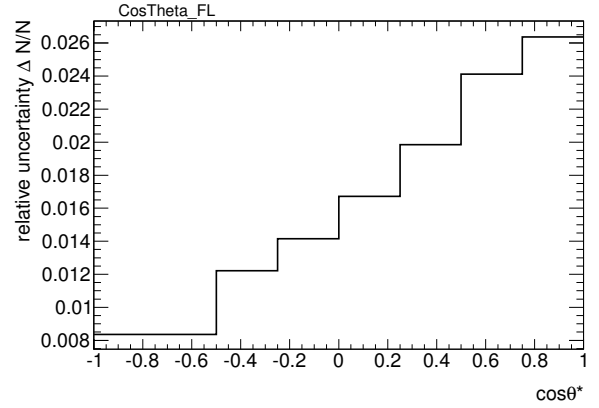
(d) F_L template, μ+jets
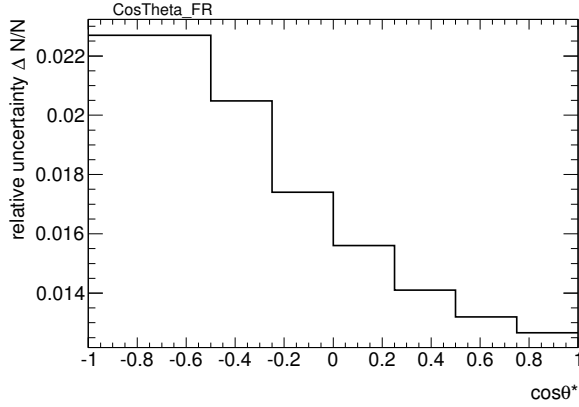
(e) F_R template, e+jets
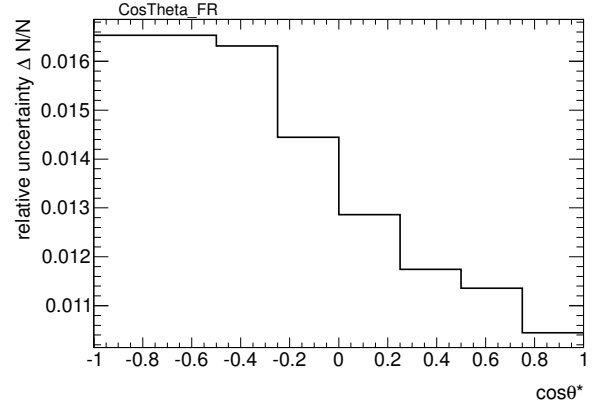
(f) F_R template, μ+jets

Figure 9.3.: Relative uncertainty per bin for the signal templates. The binning is with seven bins in total. The first bin has twice the width of all other bins. On the left side, the relative uncertainties in the e+jets channel are shown, on the right they are shown for the μ+jets channel.
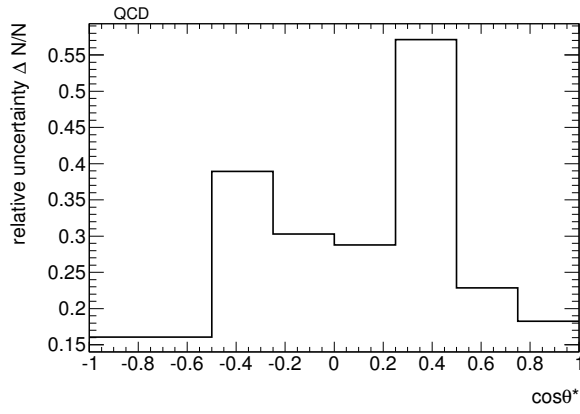
(a) multijet template, e+jets
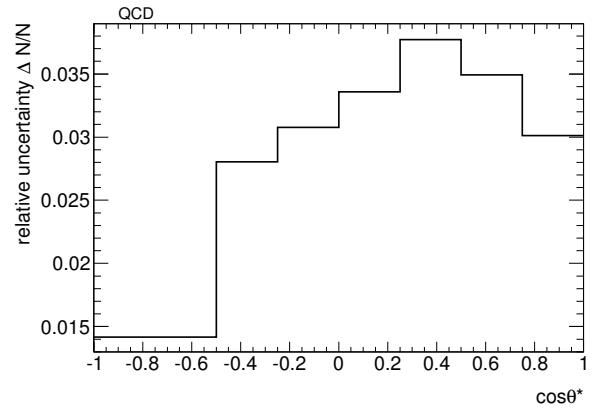
(b) multijet template, μ+jets
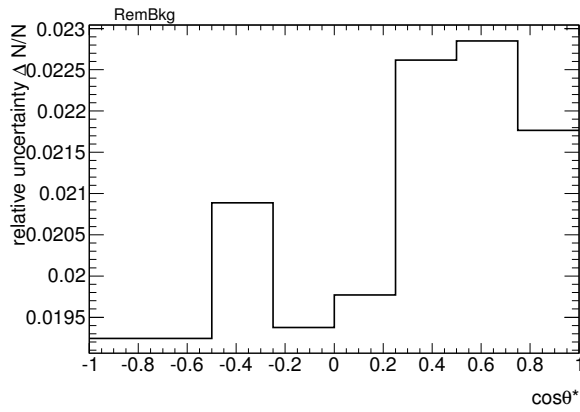
(c) RemBkg template, e+jets
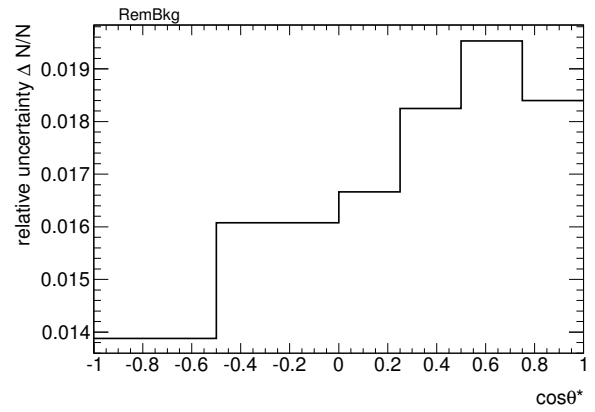
(d) RemBkg template, μ+jets
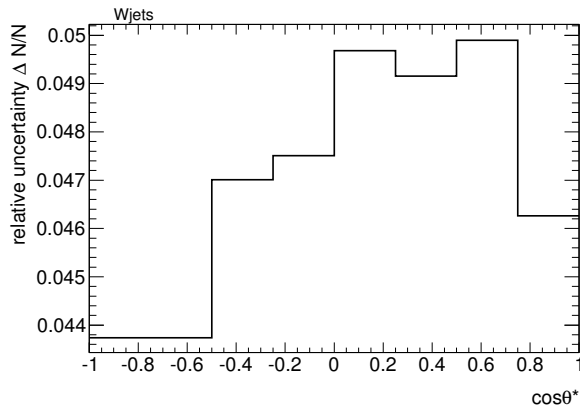
(e) W+jets template, e+jets
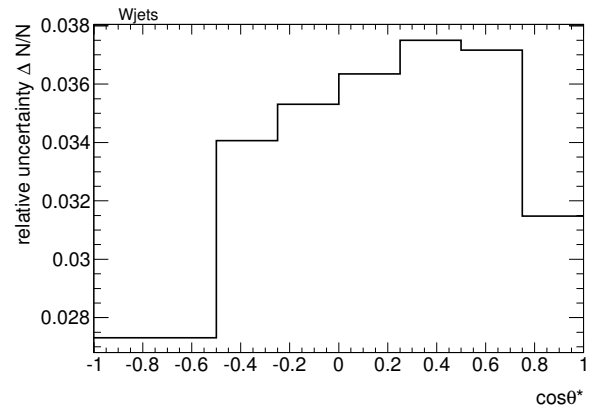
(f) W+jets template, μ+jets

Figure 9.4.: Relative uncertainty per bin for the background templates. The binning is with seven bins in total. The first bin has twice the width of all other bins. On the left side, the relative uncertainties in the e+jets channel are shown, on the right they are shown for the μ+jets channel (RemBkg stands for 'remaining background').

template will not be changed in a profile likelihood fit. Systematics affecting this background will be evaluated via ensemble tests. For all other relevant templates with seven bins in total now, the 5% criterion is fulfilled. It was stated that this criterion is a compromise. The expected increase on the statistical uncertainties of the estimators has to be studied. This has been done by looking at the uncertainty as a function of the number of bins. The following studies have been performed with fixed background (just signal templates fitted, background priors with a width of zero) and a template fit to data without nuisance parameters. The behaviour of the
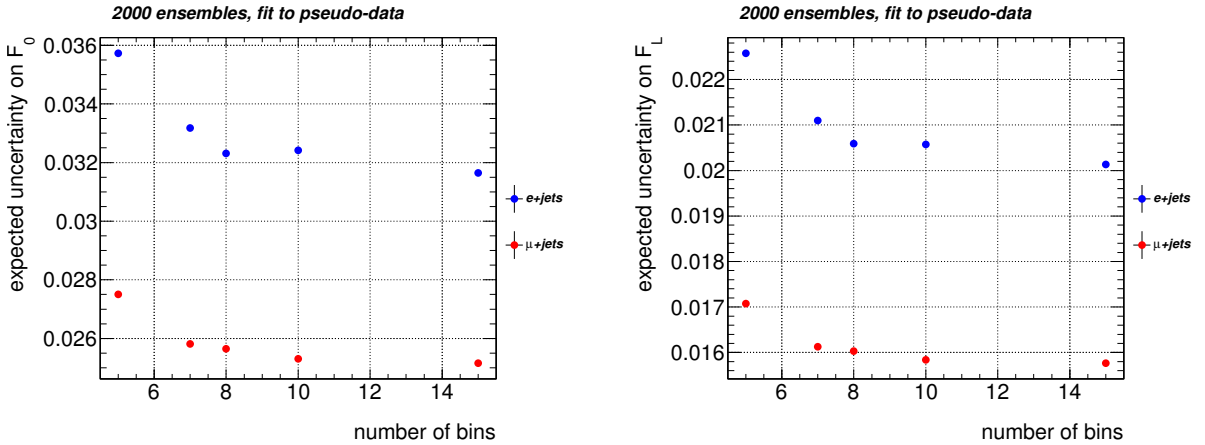

Figure 9.5.: Expected statistical uncertainty on F_0 (left) and F_L (right) as a function of number of bins. The background was fixed in the template fit.

statistical uncertainty depending on the number of bins (equal bin width) is shown for F_0 and F_L in Fig. 9.5 (F_R uncertainty shown in Fig. A.8). The uncertainties from fits in the e+jets channel are always higher than for the μ+jets channel due to the tighter selection criteria that lead to a smaller data sample. As expected, the uncertainty decreases with increasing bin number due to sensitivity gain to the shape of the $\cos\theta^*$ distribution. The sensitivity loss for a binning with seven bins only leads to a slightly increased uncertainty by about 0.001 ($\hat{=}5\%$) compared to 15 bins. Finally, the non-equidistant binning described here (visible in Fig. 9.3 and Fig. 9.4) is chosen and applied throughout the full analysis. The resulting templates can be seen in Fig. 9.6 for both the signal and the background templates (all normalised to unity) in the e+jets channel. The signal shapes still show distinct features while the background templates are rather flat in $\cos\theta^*$. The templates for the μ+jets channel can be found in Fig. A.5.

9.1.2. Combined Likelihood Fit

The amount of data that was collected by the ATLAS experiment has lead to many physics analysis that are not dominated by statistical uncertainties but rather by systematic uncertainties. For the W-helicity analysis it has been observed that the statistical uncertainty on the helicity fractions is still a dominant uncertainty, also after the evaluation of the full 2011 data set. In the present case, the estimated uncertainty is not purely of statistical nature but includes the uncertainties on the background normalisation. Therefore, an approach to reduce this uncertainty is to include a control region into the fit, namely a region that requires exactly zero b-tags, all other selection criteria stay the same. This region is expected to be dominated by the W+jets background. This is confirmed by performing such a selection. Control plots and event yields for
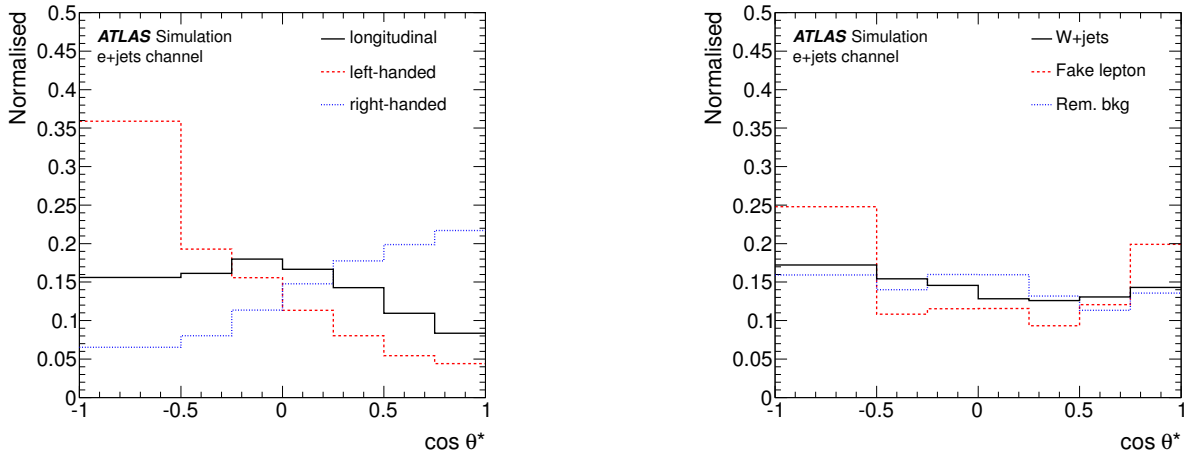
Figure 9.6.: Signal (left) and background (right) templates with seven bins for the e+jets channel with standard $t\bar{t}$ selection.

the 0 exclusive b-tag region can be found in the appendix (Fig. A.3, Fig. A.4 and Tab. A.7). The goal is then to fit in several channels simultaneously: thereby the W+jets background can be constrained through the information of the control region. The different channels are the e+jets and μ+jets channels splitted into different b-tag multiplicities. A simultaneous or *combined* fit means that the templates and data in $\cos\theta^*$ are coupled for all considered channels. The three signal templates for F_0, F_L and F_R are then merged, building three templates over all channels. The background templates can be treated differently: they can be also merged over all channels or kept separately in all channels.

First, a fit setup of six channels has been studied: 0 exclusive, 1 exclusive and 2 inclusive b-tag channels (short 0excl, 1excl and 2incl), 15 bins each (old binning). One setup contained 11 templates: all processes were merged into one template but the multijet background. This is kept independent in each channel. This is due to different modelling strategies in the different channels that would need to be independent in a template fit to have enough freedom to adjust to the data, because the multijet background template will never be modified in a profile likelihood fit. This leads to six multijet templates. A different setup included 21 templates: here all background templates are treated independently over the six channels. A fit to pseudo-data for

Fit setup	σ_{F_0}	σ_{F_L}	σ_{F_R}
11 templates	0.0210	0.0132	0.0103
21 Templates	0.0204	0.0129	0.0098

Table 9.1.: Expected uncertainties from 2 000 ensemble tests to pseudo-data. A combined fit in six channels (e+jets and μ+jets 0excl, 1excl and 2incl b-tags each) has been performed with different numbers of templates (explanation given in the text). The number of bins in $\cos\theta^*$ is 15.

both setups revealed an improving precision compared to a setup, where only the e+jets and μ+jets channel are combined to a two channel fit (see values in first row in Tab. 9.2). Tab. 9.1 shows the expected uncertainties from 2 000 ensemble tests to pseudo-data on the helicity frac-

tions for the two six channel setups. It can be observed that the uncertainties are of similar size. This fact leads to the question, if the 0excl b-tag control region is really necessary to constrain the backgrounds, or if it is sufficient to just split the 1 inclusive b-tag sample into 1excl and 2incl b-tag bins. Another setup was tested, where the 0excl b-tag control region was removed from the fit, thus a combined fit in four channels was performed. Tab. 9.2 compares the expected uncertainties from 2 000 ensemble tests to pseudo-data for three different setups: e-μ, 1incl b-tags denotes the standard $t\bar{t}$ selection, where the combined fit is performed in the two channels e+jets and μ+jets. The denotation e-μ, 1excl, 2incl b-tags stands for the mentioned fit in four channels. This setup is obtained by splitting into 1excl and 2incl b-tag bins. Finally, the six channel fit setup is denoted by e-μ, 0, 1excl, 2incl b-tags. Here, all setups allow the different multijet background contributions to float separately within their uncertainties. The priors on the fitted backgrounds include statistical, normalisation (cross-section and scale factor uncertainties) and luminosity uncertainties. The multijet background has an uncertainty of 50% in the e+jets channels. In the μ+jets channel, the uncertainty is 20% except for the 2incl b-tag channel where the uncertainty is 40%.

The observed numbers for a template fit with fitted background lead to the conclusion: Splitting the sample into b-tagging categories allows to constrain the background so that the uncertainties on the F_i are significantly reduced. The inclusion of a control region with 0excl b-tags does not lead to a further significant reduction of the uncertainties.

Fit setup	fixed background			fitted background		
	σ_{F_0}	σ_{F_L}	σ_{F_R}	σ_{F_0}	σ_{F_L}	σ_{F_R}
e-μ, 1incl b-tags	0.02111	0.01340	0.01009	0.03363	0.01784	0.01910
e-μ, 1excl, 2incl b-tags	0.02032	0.01295	0.00968	0.02226	0.01430	0.01063
e-μ, 0, 1excl, 2incl b-tags	0.02019	0.01286	0.00962	0.02220	0.01419	0.01037

Table 9.2.: Expected uncertainties from 2 000 ensemble tests to pseudo-data. Three different setups are compared for both fitted backgrounds and fixed backgrounds. The new binning with seven bins in $\cos\theta^*$ was adopted. All templates are merged except for the multijet background templates.

A remaining question is, to what extend exactly the high statistical uncertainties on F_i are caused by the background uncertainties. This can be studied by performing the same tests with a fixed background. The corresponding uncertainties for the three setups are listed in Tab. 9.2 in the first three columns. The uncertainties are smaller than for a fitted background. But still, the uncertainties are relatively high. This leads to the conclusion that the dominant part of the statistical uncertainty of the likelihood estimators is due to the statistical uncertainty of the data themselves. The background uncertainties do contribute but not as much as can be seen from the values in the table. The uncertainties for the fitted background are only slightly higher than for the fixed background fits (last two rows in Tab. 9.2).

These studies lead to the decision on a preliminary setup to be used in the analysis: extraction of the helicity fractions via a combined likelihood fit in four channels, namely e+jets and μ+jets channel with 1excl and 2incl b-tag bins. This setup is simpler than the six channel setup and thus preferred. Still, the six channel setup is considered to perform cross checks and to be able to decrease uncertainties when systematic uncertainties like b-tagging related uncertainties are considered. All templates but the multijet background templates are merged, which leads to

nine templates in the four channel setup. The required freedom in a template fit for different channels of the same template can be ensured by the possibility to profile these templates.

b-tag Multiplicity

When splitting into different *b*-tag bins, the data description of the *b*-tag multiplicity by the MC has to be considered. Here the PROTOS event generator (so do other $t\bar{t}$ generators) reveals some problems in describing the data correctly. Figure 7.1(b) and Fig. 7.2(b) show the *b*-tag multiplicity in MC and data. Discrepancies are visible in both e+jets and μ+jets channels. For the MC weighting to match the data[a], p_T and η dependent scale factors are derived that are multiplied to single jet weights. These scale factors are defined as [83, 120]:

$$k_{\varepsilon_b}^{\text{data/sim}}(p_T, \eta) = \frac{\varepsilon_b^{\text{data}}(p_T, \eta)}{\varepsilon_b^{\text{sim}}(p_T, \eta)}, \qquad k_{\varepsilon_l}^{\text{data/sim}}(p_T, \eta) = \frac{\varepsilon_l^{\text{data}}(p_T, \eta)}{\varepsilon_l^{\text{sim}}(p_T, \eta)}.$$

The variables $\varepsilon_b^{\text{data}}$ and $\varepsilon_b^{\text{sim}}$ are the efficiencies for *b*-tagging in data and simulated events, respectively. The probability to tag a non *b*-jet is ε_l (*l* for light jet), which is called mis-tag rate. Again, these are measured both for data and simulation. How these quantities are obtained is explained in detail in [120], where different data sets than for this analysis are used. Finally, an overall *b*-tag scale factor that is multiplied to the event weight is obtained by multiplying the jet scale factors from the jets present in the event. No application of the *b*-tag scale factors has been studied but revealed no improvement in the description of the data. Nevertheless, in order to perform a fit in splitted *b*-tag bins, this issue needs to be handled carefully. Here again, profiling the *b*-tag scale factors may lead to an improved description of the data: a profiling fit should be able to reweight the *b*-tag bins such that they match the data best.

9.2. Systematic Uncertainties

This section deals with the analysis optimisation by reducing systematic uncertainties. The procedure of selecting systematic sources to be included in a profile likelihood fit will be described in the following. The inclusion into the actual fit will be explained in Sect. 9.2.2 and a test with pseudo-data will be compared to the evaluation with ensemble tests (Sect. 9.2.3).

9.2.1. Selection of Relevant Systematic Sources

It has been pointed out in Sect. 9.1.1 that it only makes sense to profile systematic sources, if the deviations caused by $\pm 1\sigma$ variations is larger than the statistical uncertainty in MC in a certain bin in $\cos\theta^*$. Otherwise, statistical fluctuations are parameterised and profiled, leading to artificially increased uncertainties. To find out which components are suited for profiling, such as introduced in Sect. 8.3.2, the relevant systematic sources are considered and a criterion is applied: if more than 20% of all bins in all channels and templates (except for the multijet background template) have relative deviations larger than the statistical uncertainty of the nominal bin entry, then the systematic is suited for profiling (in the following denoted as '20% criterion'). A set of relevant systematics to be considered is introduced in the following.

---

[a] A calibration of *b*-tagging algorithms is necessary as the MC simulations do not fully describe the detector performance.

Jet Energy Scale

The jet energy scale (JES) is the uncertainty on the energy measurement of jets in the calorimeter and it is η and p_T dependent. The JES is a dominant uncertainty in the W-helicity measurement (e. g. [58, 119]). The JES uncertainty is determined by dedicated measurements (in-situ measurements, test beam measurements [121, 122]). The JES calibration often makes use of p_T balanced di-jet systems or jets recoiling against a Z-boson or γ [121, 122]. The uncertainty decreases with higher p_T and the measurement in the central calorimeter region is more precise than in regions with higher $|\eta|$ values. The uncertainty for jets with $|\eta| < 1.2$ and $55 < p_T < 500$ GeV is minimal and less than 1% [121]. For lower p_T values the uncertainty goes up to 3%. The largest uncertainty is 6% for low p_T jets at $|\eta| = 4.5$. Additional contributions to the JES depend on the event topologies and are between 0.5% and 3%. The JES is composed of 21 components: it contains eleven nuisance parameters related to the in-situ calibrations. An additional uncertainty is related to b-jets, the b-JES, that contributes up to 2.5% uncertainty [121]. In a multijet environment such as the ℓ+jets topology of $t\bar{t}$ events, uncertainties from close-by jets, flavour composition (light jets, b-jets) of the sample and the response of the calorimeter to that are taken into account. An intercalibration between different $|\eta|$ regions is performed that contributes two sources to the global JES uncertainty. Uncertainties from pile-up, quantified via $\langle\mu\rangle$ and the number of primary vertices, are apparent as well as a term for high p_T jets beyond 1 TeV. The dedicated JES analyses were performed with a certain MC 2011 production ('MC11b'). This needs to be taken care of when using different MC production samples and thus a non-closure term relative to the MC11b samples is added to the JES.

(a) (b)

Figure 9.7.: Comparison of relative deviation to relative statistical uncertainty of the nominal F_R template in the e+jets, 1 excl. b-tag channel: (a) nuisance parameter used for the in-situ calibration, (b) flavour composition component.

Not all of these 21 components may influence the shape of the $\cos\theta^*$ distribution. The relevant components for the profiling are selected by using the introduced 20% criterion. Fig. 9.7 shows examples for two JES components and their relative deviation to the nominal F_R template in the e+jets, 1excl b-tag channel. The yellow band indicates the relative statistical uncertainty per bin. The coloured lines are the deviations stemming from $\pm 1\sigma$ shifts of the respective JES component. The deviation of the shown nuisance parameter component is fully contained in the

yellow band. This systematic uncertainty turns out to be not suited for profiling. The flavour composition component shows real systematic shifts in $\cos\theta^*$ that cannot be covered by the statistical uncertainty. It is also visible that the deviations are not entirely flat over $\cos\theta^*$ and thus will produce shape variations. This component is suited for profiling.

b-tagging

b-tag scale factors (SF) were introduced in Sect 9.1.2. One approach to evaluate the uncertainties of these SFs on the helicity fractions is to vary efficiencies and mis-tag rates within their uncertainties. This may not take correlations among these factors properly into account. Therefore, another method is to use the eigenvectors of an uncertainty matrix for the SFs. This constructs nine *b*-tag SF components whose influences on $\cos\theta^*$ can be investigated. Fig. 9.8 shows two of these components that are numbered from 0 to 8 and the induced deviations on the F_0 template in the e+jets, 2incl. *b*-tag channel. The component labelled *break0* (Fig. 9.8(a)) does not fulfil the 20% criterion, the fluctuations stay within the statistical uncertainties. The only *b*-tag SF component that contributes a systematic shift is the *break8* (Fig. 9.8(b)) component. It is rather flat in $\cos\theta^*$. This component is suited for profiling and is able to shift single *b*-tag bins in a profile fit to match the data best.

(a)   **(b)**
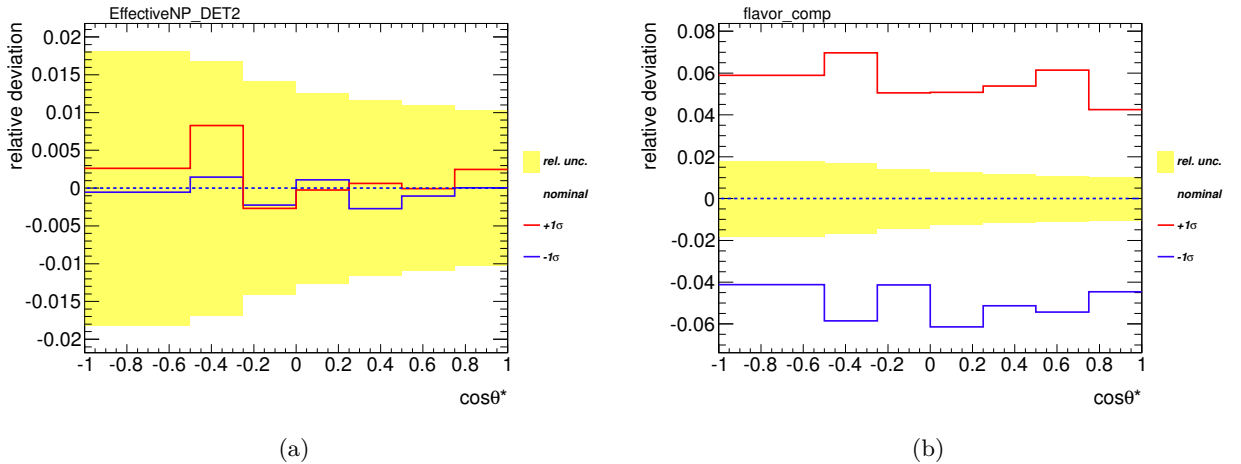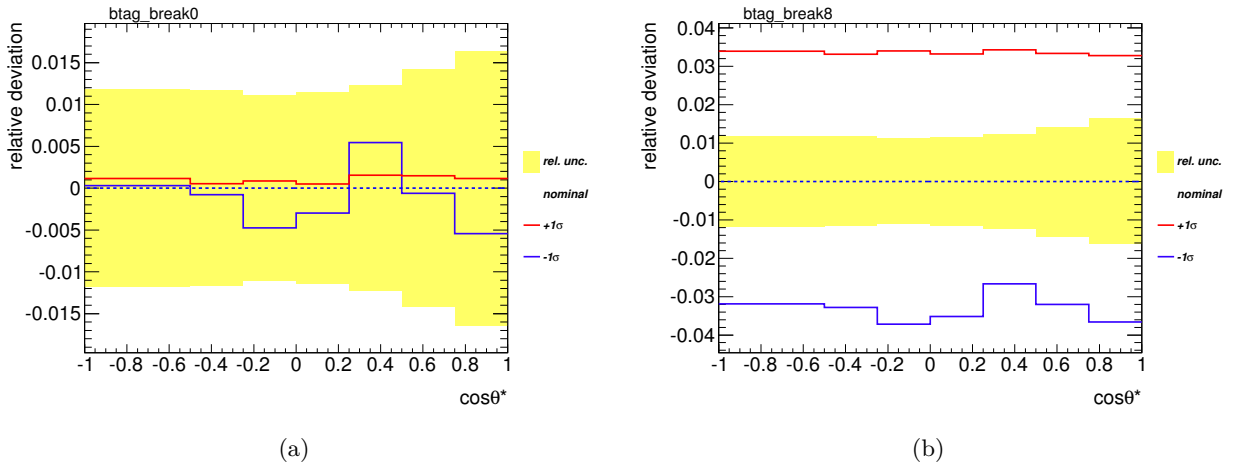
Figure 9.8.: Comparison of relative deviation to relative statistical uncertainty of the nominal F_0 template in the e+jets, 2 incl. *b*-tag channel: (a) *b*-tag SF component *break0*, (b) *b*-tag SF component *break8*.

Jet Energy Resolution

The influence of the jet energy resolution (JER) is determined by smearing the jet momenta in MC with a Gaussian resolution function. This is done according to a 10% uncertainty, the relative difference of the JER in data and MC [123]. This uncertainty is one-sided as it is not possible to improve the resolution of the jet energy after simulation. The influence of the JER variation of 1σ on the F_R and remaining background template is shown in Fig. 9.9 for the e+jets, 1excl *b*-tag channel. The deviations cause shape variations in $\cos\theta^*$ not covered by statistical uncertainties. The JER fulfils the 20% criterion and is considered for profiling and expected to be constrained by the profile fit. The one-sided variation is symmetrised for the profiling (see Sect. 10.2).

(a)　　　　　　　　　　　　　(b)
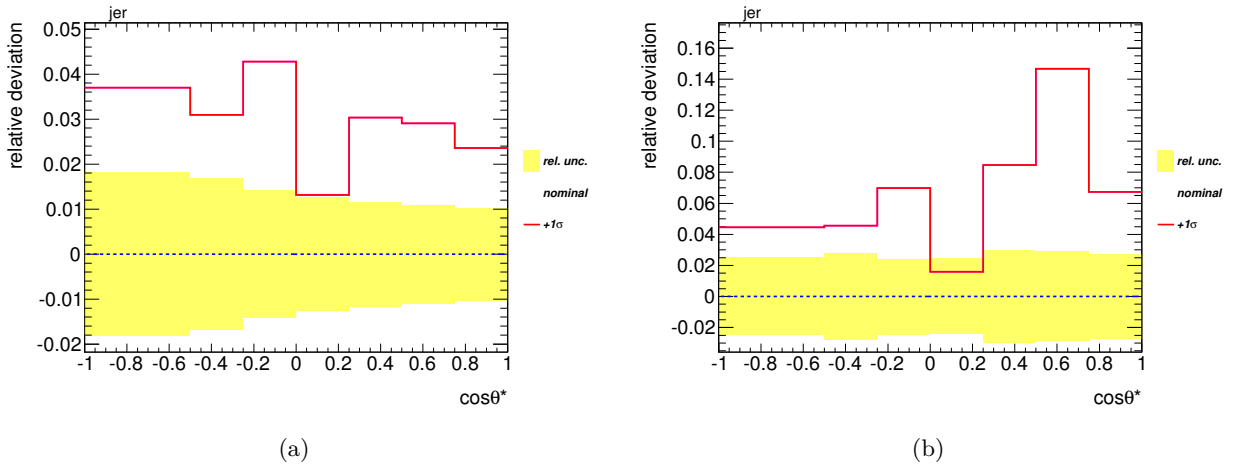
Figure 9.9.: Comparison of relative deviation from JER to relative statistical uncertainty of the nominal F_R (a) template and remaining background template (b) in the e+jets, 1excl b-tag channel.

Lepton Scale Factors

Lepton identification, reconstruction and trigger efficiencies give rise to scale factors that correct the MC description to match the efficiencies in data. The electron SFs only influence the e+jets channels and the muon SF only influence the μ+jets channels. The SFs can be varied within their uncertainties up and down. Fig. 9.10 shows the variation in the F_L, 1excl b-tag

(a)　　　　　　　　　　　　　(b)
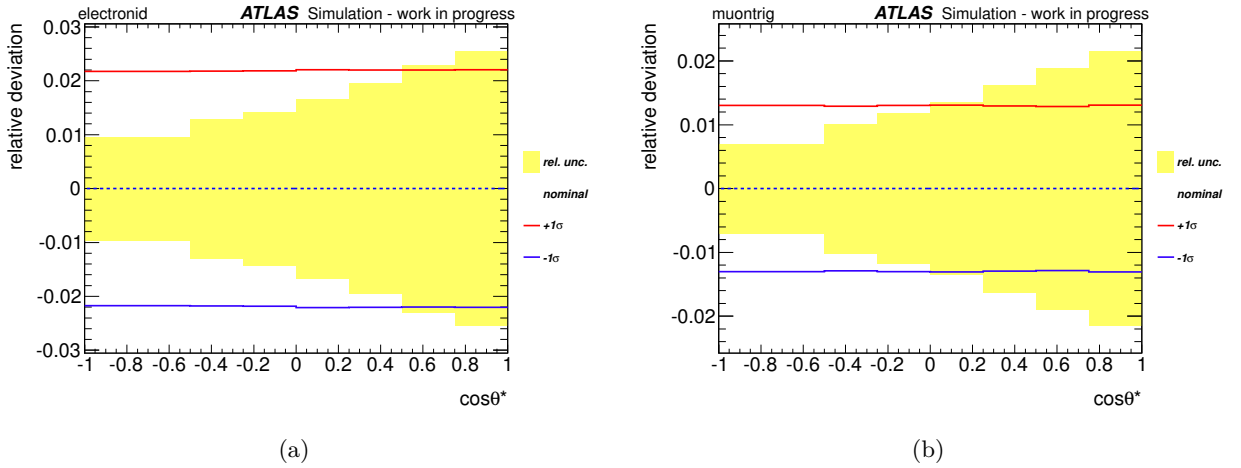
Figure 9.10.: Comparison of relative deviation from electron id SF (a) and muon trigger SF (b) to relative statistical uncertainty of the nominal F_L template, 1excl b-tags.

template for both e+jets (a) and μ+jets (b) channels from varying the respective lepton SFs. The electron SF shown is the identification (id) SF, the muon trigger SF is shown in Fig. 9.10(b). Both SFs are the only ones whose relative deviations are larger than the statistical uncertainties of the nominal templates. Both SFs variations are flat in $\cos\theta^*$. They are suited as nuisance parameters in the profile likelihood fit.

The shown systematic components are not all that are considered for profiling. An exhaustive list will be given in Sect. 10.2.

9.2.2. Inclusion in Profile Likelihood Fit

The above described procedure of selecting relevant systematic components as nuisance parameters for the profile fit is applied to all considered systematic sources. The systematics that fulfil the 20% criterion are included as usual nuisance parameter in the profile fit. For the profiling, only $\pm 1\sigma$ systematic variations are taken into account and therefore the quadratic interpolation method is utilised. From 21 JES components only seven components are considered for the usual profiling and only one component of the b-tag SF uncertainty. The other components are nevertheless considered in the analysis: a so-called *acceptance profiling* is applied. They are also included as nuisance parameters but the systematic templates are modified: the nominal templates in each channel are scaled with the integral of the systematic templates. In this way the normalisation of single channels can change, but the shape per channel stays the same. It is expected that these nuisance parameters only have an influence on the uncertainty of the fitted helicity fractions rather than the helicity fractions themselves. Acceptance profiling is applied to each systematic that fails the 20% criterion. If the combined likelihood fit shows no changes in the fitted quantities after including the acceptance components, they will be omitted from the fit.

9.2.3. Test with Pseudo-Data

The following test shows how much precision is gained moving from an ensemble test evaluation of systematic uncertainties to a profile likelihood analysis. The test is performed using the four channel combined fit setup with nine templates in total (multijet background separately in four channels). The profile likelihood fit includes nuisance parameters from JES and b-tagging SF components. Including 30 (including acceptance components) or only eight nuisance parameters (shape changing nuisance parameters) reveals no difference in the fitted quantities. The ensemble test evaluation builds pseudo-data with the single variations and fits ensembles to these. The uncertainties are then added in quadrature. Tab. 9.3 shows the outcome of the two analyses. It can be observed that the uncertainties from the profile fit are smaller than the ones from the ensemble tests. This confirms the expectation that the profile likelihood analysis is able to decrease systematic uncertainties. The uncertainties of the ensemble test evaluation are almost twice as large as the uncertainties from the profiling: $\sigma(F_0)$ is larger by a factor of 1.8, $\sigma(F_L)$ is larger by a factor of 1.5 and $\sigma(F_R)$ is larger by a factor of 2.1 for the ensemble test analysis. This test shows explicitly the power of profile likelihood analyses and their advantage compared to conservative ensemble test evaluations in this particular W-helicity analysis.

Uncertainty	Profiling	Ensemble Test
$\sigma(F_0)$	0.0253	0.0463
$\sigma(F_L)$	0.0152	0.0231
$\sigma(F_R)$	0.0134	0.0279

Table 9.3.: Expected uncertainties from a combined profile likelihood fit to pseudo-data (second column) compared to the expected uncertainties from ensemble tests (2 000 ensembles each). The JES and b-tagging SF uncertainties are considered only.

10. Results

This chapter presents the results of the W-helicity measurement using $t\bar{t}$ events in the ℓ+jets channel with the template method. Results from the simple template fit without systematics, without nuisance parameters, are presented in Sect. 10.1. The emphasis is on the statistical uncertainty. The treatment of systematic uncertainties will be discussed in Sect. 10.2. The final results from a combined likelihood fit to data are presented in Sect. 10.3. The profile likelihood analysis results are discussed in Sect. 10.3.1. A comparison to an analysis that evaluates all systematic uncertainties via ensemble tests is made in Sect. 10.3.2. Limits from the profile likelihood analysis on anomalous couplings are derived in Sect. 10.4.

10.1. Statistical Uncertainty

The statistical uncertainty of the W-helicity fractions is obtained by a simple template fit to data without including nuisance parameters. The sample is split into four channels according to the lepton flavour and the b-tag multiplicity. Nine templates as described in Sect. 9.1.2 are used. The result is shown in Fig. 10.1.

Figure 10.1.: Template fit result in four channels with nine templates: the red line is the best fit result, the black points are the data. The blue area is the fitted background contribution, the hashed bands give the statistical uncertainty of the fit. The reduced χ^2 and probability of the fit are also given.

The best fit result is shown as the red line. The hashed uncertainty bands in the actual and the ratio plot contain the statistical uncertainty on the fit only. The black points are the data, the blue area is the fitted background and the dashed line describes the SM expectation. The

fitted numbers of background events are lower than the ones from the MC prediction. The MC background prediction was used to display the SM expectation in Fig. 10.1. This explains why the SM prediction is higher in the 1excl *b*-tag bins than the best fit result that follows the data points. The fitted values and statistical uncertainties can be found in Tab. 10.1 in the second row. The fitted helicity fractions are taken as input for building pseudo-data sets.
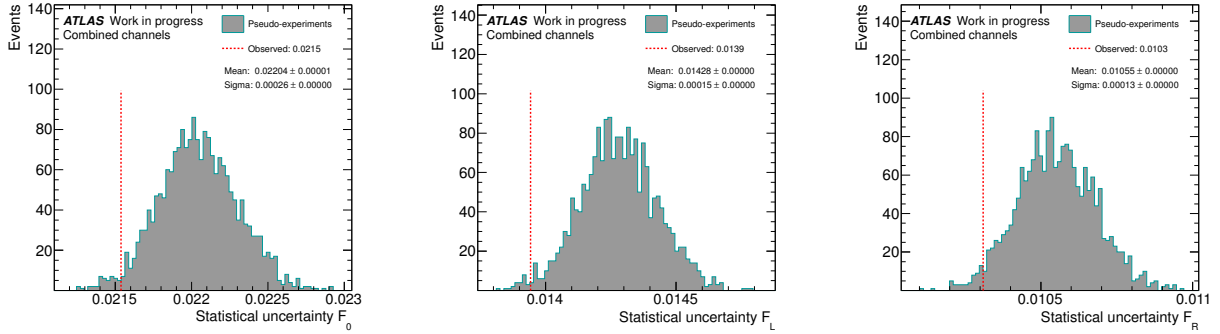
Figure 10.2.: Comparison of expected uncertainty (mean value of pseudo-data distribution) with uncertainty from data fit output (dashed line) for the four channels fit with nine templates. 2 000 ensembles were created from the data fit output fractions for F_0, F_L and F_R.

Ensembles are created by fluctuating the pseudo-data bin contents with Poissonian probability (as described in Sect. 8.3.1). Ensemble tests with 2 000 ensembles are then performed and the output distribution of the statistical uncertainties are compared with the one from the single data fit. This can be seen in Fig. 10.2. The dashed red line indicates the data fit uncertainty and the grey distribution stems from the described ensemble tests. The values are in agreement, though it can be noted that the fitted value is always smaller than the expected value. The

Fit setup	F_0	F_L	F_R
e-μ, 1excl, 2incl *b*-tags	0.605±0.022	0.343±0.014	0.052±0.010
e-μ, 0, 1excl, 2incl *b*-tags	0.605±0.023	0.353±0.015	0.042±0.011

Table 10.1.: Comparison of fitted helicity fractions with their statistical uncertainties from data fit in four (*e*-μ, 1excl, 2incl *b*-tags) and six (*e*-μ, 0, 1excl, 2incl *b*-tags) channels.

same simple template fit is performed with the six channel fit setup (including events with 0 *b*-tags) and eleven templates. The fit result can be seen in Fig. 10.3. The fitted helicity fractions and their statistical uncertainty can be found in the last row of Tab. 10.1. The fitted values are similar to the four channel fit, the statistical uncertainties are slightly higher. Also, for the six channel fit, pseudo-data has been created from the fitted helicity fractions and ensemble tests have been performed to compare expected uncertainties with observed uncertainties in the data fit. The comparison is shown in Fig. 10.4. The expected uncertainties (the mean values of the ensemble test distributions) are similar to the ones from Fig. 10.2 for the four channel fit. Here, the observed statistical uncertainties are always slightly higher than the expected uncertainties.

A template fit in four channels that allows all background contributions to float independently

in the different channels is shown in the appendix (Sect. A.4.1). Fitted values and uncertainties are listed in Tab. A.8 and are compatible with the values in Tab. 10.1 discussed here.
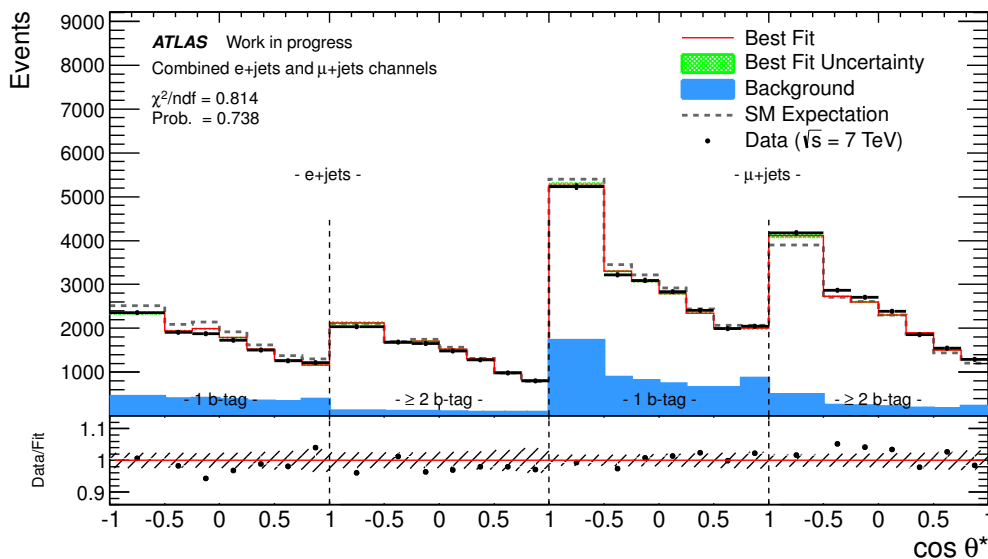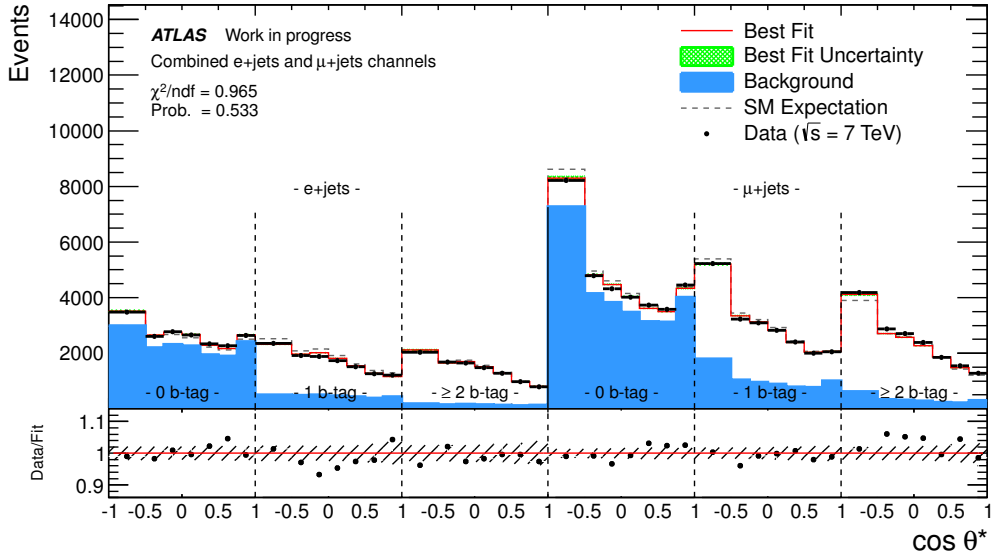

Figure 10.3.: Template fit result in six channels with eleven templates: the red line shows the best fit result, the black points the data. The blue area is the fitted background contribution, the hashed bands give the statistical uncertainty of the fit. The reduced χ^2 and probability of the fit are also given.
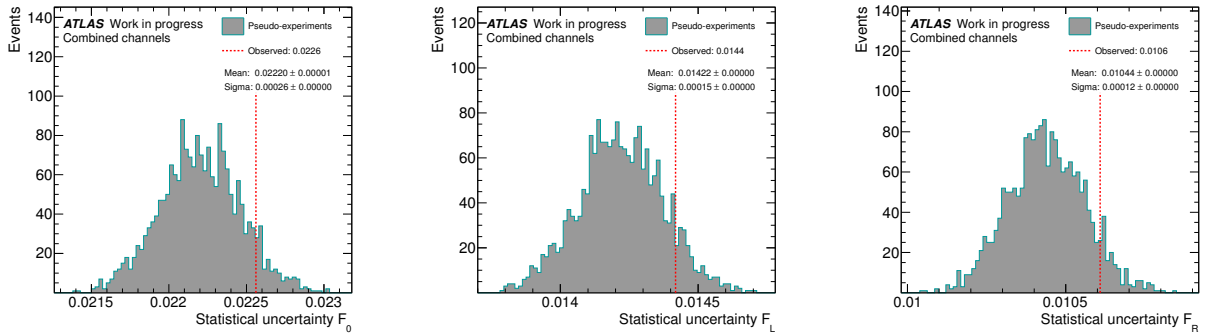
Figure 10.4.: Comparison of expected uncertainty (mean value of pseudo-data distribution) with uncertainty from data fit output (dashed line) for the six channels fit with eleven templates. 2 000 ensembles were created from the data fit output fractions for F_0, F_L and F_R.

10.2. Systematic Uncertainty

This section deals with sources of systematic uncertainties that are relevant for this analysis. The evaluation of each source will be explained in the following. Four categories of sources of systematic uncertainties are considered: the signal and background modelling, the detector modelling and the method-specific uncertainties.

10.2.1. Signal Modelling

The category of signal modelling only affects the $t\bar{t}$ process modelling. In this case, the term *modelling* refers to MC related uncertainties. These uncertainties are generally considered to be discrete systematics and therefore cannot be profiled. They are all evaluated via ensemble tests, as described in Sect. 8.3.1. If not stated otherwise, $2\,000$ ensembles are produced to evaluate the systematic uncertainties. They are described in the following.

Choice of Monte Carlo Generator

A dominant uncertainty used to be the one due to the choice of MC generators (e. g. [58, 119]). Different physics models are compared here: NLO to LO generators, different shower, hadronisation and decay models used within different MC generators. The respective uncertainty is not suited for profiling as it is discrete[a]. Pseudo-data sets from different $t\bar{t}$ generators are created and ensemble tests are performed. Always two generators are compared: the full difference in F_i is taken as systematic uncertainty. In this analysis, the MC@NLO generator and ALPGEN+HERWIG were compared (full detector simulation). They are both showered by HERWIG. To take differences in shower modelling into account, samples created with POWHEG+PYTHIA and POWHEG+HERWIG were compared (fast detector simulation). This uncertainty is quoted as parton shower uncertainty. No comparisons between POWHEG and other generators were made due to a bug in the τ-polarisation in POWHEG that leads to a modified $\cos\theta^*$ distribution and differences to other generators would overestimate the uncertainty. Uncertainties from MC generator and parton showering are added in quadrature.

Initial/Final State Radiation

The amount of additional jets in an event produced by initial or final state radiation can be influenced by tuning the strong coupling α_s both in the ME generation and the parton shower. This is done simultaneously in the ALPGEN+PYTHIA samples that are used for the systematic evaluation. The variation in α_s can be translated into a variation in Λ_{QCD} via Eq. 2.4. Increasing Λ_{QCD} by a factor of two in both ME and parton shower leads to an increase in initial and final state radiation (ISR/FSR). Reducing Λ_{QCD} by a factor of 0.5 leads to a decrease in ISR/FSR and means less additional jets in an event. The $2\cdot\Lambda_{\mathrm{QCD}}$ and $0.5\cdot\Lambda_{\mathrm{QCD}}$ variations in ALPGEN+PYTHIA are compared via ensemble tests. The full difference in F_i is divided by two and taken as systematic uncertainty due to ISR/FSR. The corresponding pseudo-data distributions can be seen in Fig. 10.5. The events in the 1 excl. *b*-tag channels are reduced by more ISR/FSR due to a migration into the higher *b*-tag multiplicity region due to the additional jets that can contribute *b*-jets.

---

[a] One can argue that it is possible to profile the MC uncertainty because the differences in MC generators are mainly caused by different tuning parameters, different kinematic cuts that can be considered continuous. However, no other pure helicity samples are provided by other generators and therefore this uncertainty has to be evaluated via ensemble tests.
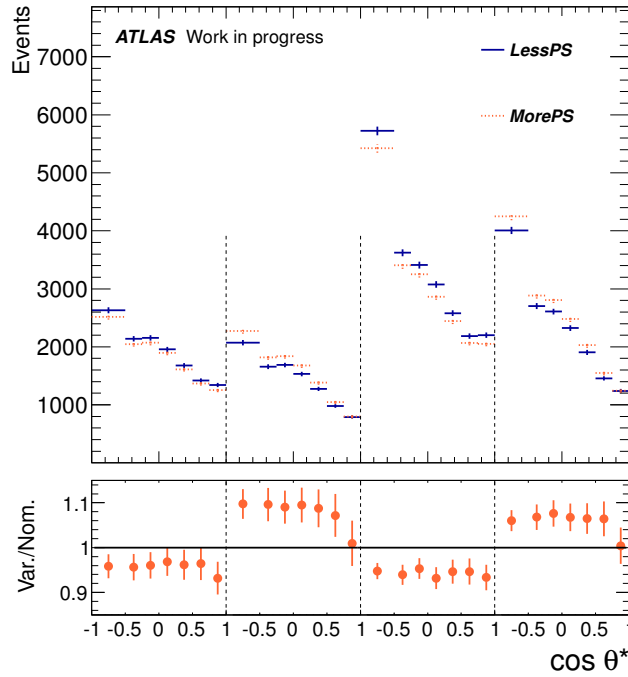
Figure 10.5.: Variations in the pseudo-data distribution due to ISR/FSR up (more PS) and down variations (less PS). The four channels can be distinguished as (e+jets, 1 excl. b-tag), (e+jets, 2 incl. b-tags) and (μ+jets, 1excl. b-tag), (μ+jets, 2 incl. b-tags) from left to right. The migration of events from the 1 excl. channels to the 2 incl. b-tag channels can be clearly observed and is expected.

Underlying Event, Renormalisation/Factorisation Scale

Underlying events are soft-scale events originating from multiple parton interactions. Certain parameters in the MC can be tuned to data to describe the underlying event (UE) activity appropriately. The uncertainty due to different UE modellings is estimated by producing pseudo-data from POWHEG+PYTHIA with differing tunes concerning the UE activity. Ensemble tests are then performed and the full difference is symmetrised and taken as systematic uncertainty. The differences due to varying renormalisation/factorisation scales (μ_R^2/μ_F^2) between different MC generators is evaluated by using the MC@NLO generator and varying this scale up and down. Also here the full difference from ensemble tests to pseudo-data with differing scales is taken as systematic uncertainty. The variation of the pseudo-data in $\cos \theta^*$ for both UE and renormalisation/factorisation scale is very small.

Top-Quark Mass

The influence of the top-quark mass on the helicity fractions is determined by performing ensemble tests to pseudo-data sets with top-quark masses varying from $m_t = 167.5 \, \text{GeV}/c^2$ to $m_t = 177.5 \, \text{GeV}/c^2$ in steps of 2.5 GeV/c^2. In total, five different top-quark masses are considered where the mass of 172.5 GeV/c^2 is the MC default. The dependence of the fractions F_i on m_t are considered: F_i is plotted as a function of m_t and a linear curve is fitted. The fitted slope is used to evaluate the variation of F_i: this is the corresponding variation when varying m_t by 1.4 GeV/c^2, which is the uncertainty on the current LHC combination on the m_t mea-

surement [124]. The dependencies of the F_i can be seen in Fig. 10.6. The m_t variation samples are produced using the Powheg generator. The dependence of F_0 on m_t is much weaker than the dependence of F_L and F_R on m_t. For the latter fractions, the top-quark mass is a dominant systematic uncertainty. This behaviour can be explained by looking at the pseudo-data for the
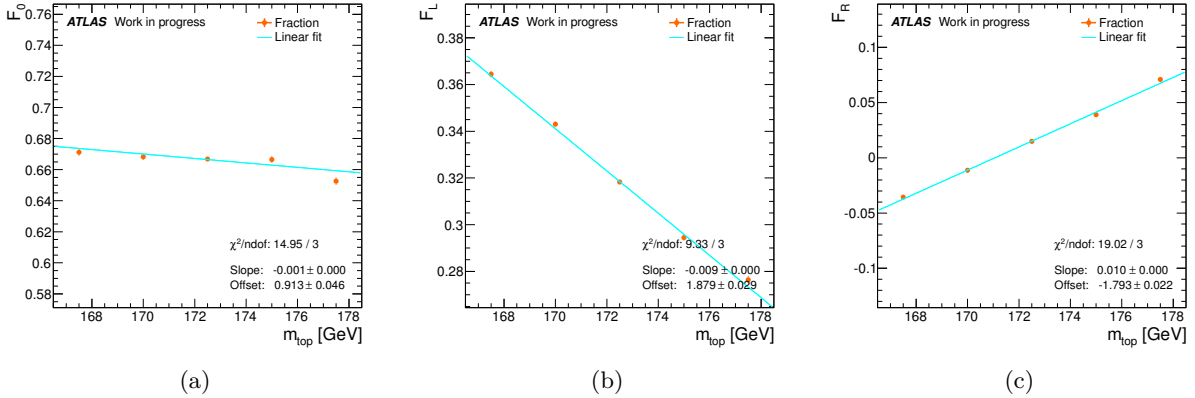

(a) (b) (c)

Figure 10.6.: Dependence of F_0 (a), F_L (b) and F_R (c) on m_t and fitted linear curves. The slope and the offset of the fit is given in the plots.

different top-quark masses. The respective plots are shown in Fig. 10.7. The normalised distribution in Fig. 10.7(b) clearly shows how the distributions tend to higher $\cos \theta^*$ values with increasing top-quark mass, and thus the F_R rate is enhanced and the F_L rate is decreased while the F_0 rate is hardly influenced. A $\cos \theta^*$ of nearly unity translates into an angle of $\theta^* = 0°$, which means that the lepton and the top-quark in the rest-frame of the W-boson are anti-parallel. This translates back into a stronger boost of the W-boson in the t-quark rest frame which is expected for higher top-quark masses.

PDF Uncertainty

The uncertainty related to the choice of PDF sets is evaluated by reweighting the signal Protos $t\bar{t}$ samples with NLO PDF sets[b], namely CT10 [43], MSTW2008nlo68cl [125] and NNPDF20 [126]. A new event weight is calculated via:

$$w_{\text{new}} = \frac{\text{PDF}(x_1, f_1, Q) \cdot \text{PDF}(x_2, f_2, Q)}{\text{CTEQ6L1}(x_1, f_1, Q) \cdot \text{CTEQ6L1}(x_2, f_2, Q)}.$$

The variables x_i and f_i denote the momentum fractions and flavours of the incoming partons; Q is the scale of the respective event. The weights are provided by the LHAPDF tool [127]. CTEQ6L1 is the original LO PDF distribution devised in the Protos samples. The PDF sets include a number of *error sets*, thus events are reweighted and pseudo-data is created for 52 CT10 sets, 40 MSTW sets and 100 NNPDF20 sets. Ensemble tests are performed to the pseudo-data. First, intra-PDF uncertainties are derived and finally an envelope uncertainty over all PDF sets is determined. The intra-PDF uncertainties depend on the PDF set: For CT10 and MSTW the Hessian error formalism is followed: the error PDF sets were produced by varying the best fit PDF variables within uncertainties derived from error propagation using the inverse Hesse-

---

[b] Reweighting a LO generator with NLO PDF sets is only usable for uncertainty estimation. The relative uncertainty is applied to the helicity results from the LO PDF set used in Protos.
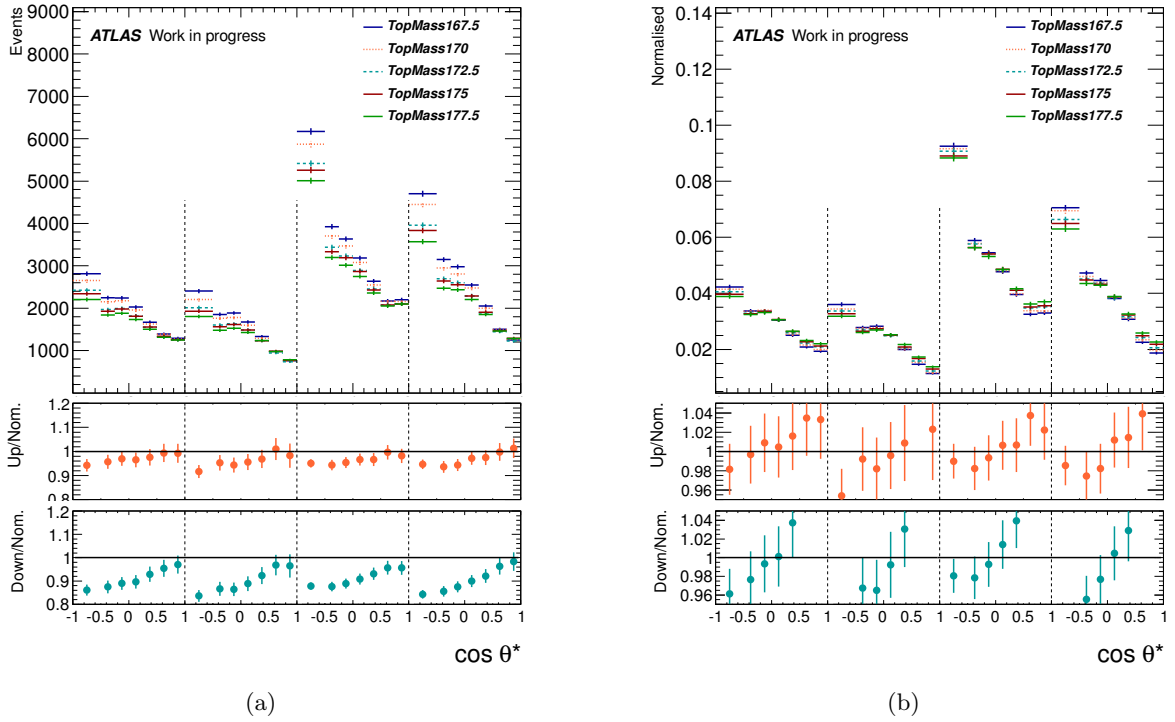
Figure 10.7.: Pseudo-data for (e+jets, 1 excl. b-tag), (e+jets, 2 incl. b-tags) and (μ+jets, 1excl. b-tag), (μ+jets, 2 incl. b-tags) from left to right for samples with different m_t (a). (b) shows the normalised distributions. The ratio plots are with respect to the sample with $m_t = 167.5 \text{ GeV}/c^2$.

matrix as the covariance matrix. For the CT10 sets, the intra-PDF uncertainty is determined building a symmetric Hessian. The corresponding uncertainty is calculated as

$$\Delta_{F_i} = 0.5\sqrt{\sum_{m=1}^{26} \left(F_{i,m+} - F_{i,m-}\right)^2},$$

where F_i is the observable, and $F_{i,m\pm}$ are the means from the ensemble tests with the m-th pseudo-data set pair. The best fit PDF that comes with the CT10 set is associated to $m = 0$. The MSTW uncertainty is evaluated using an asymmetric Hessian. The uncertainties are

$$\Delta_{F_i}^{\text{up}} = \sqrt{\sum_m \left(F_{i,m} - F_{i,0}\right)^2} \quad \text{if} \quad F_{i,m} > F_{i,0},$$

$$\Delta_{F_i}^{\text{down}} = \sqrt{\sum_m \left(F_{i,m} - F_{i,0}\right)^2} \quad \text{if} \quad F_{i,m} < F_{i,0},$$

for up and down directions, respectively. Also for MSTW, the PDF set with $m = 0$ is the best fit PDF. The NNPDF20 set does not provide a best fit PDF set. The 100 sets are an ensemble of PDFs with randomly varying parameters. They are averaged over to find the central value for F_i and the corresponding uncertainty is the standard deviation. Finally, the envelope is calculated by taking the maximal value for $F_{i,\text{central}} + \Delta$ minus the minimal value $F_{i,\text{central}} - \Delta$. Dividing

by two leads to the final uncertainty due to PDF uncertainties. Plots for all helicity fractions from the PDF set ensemble tests and the corresponding error bands are shown in Fig. 10.8.

(a)

(b)

(c)
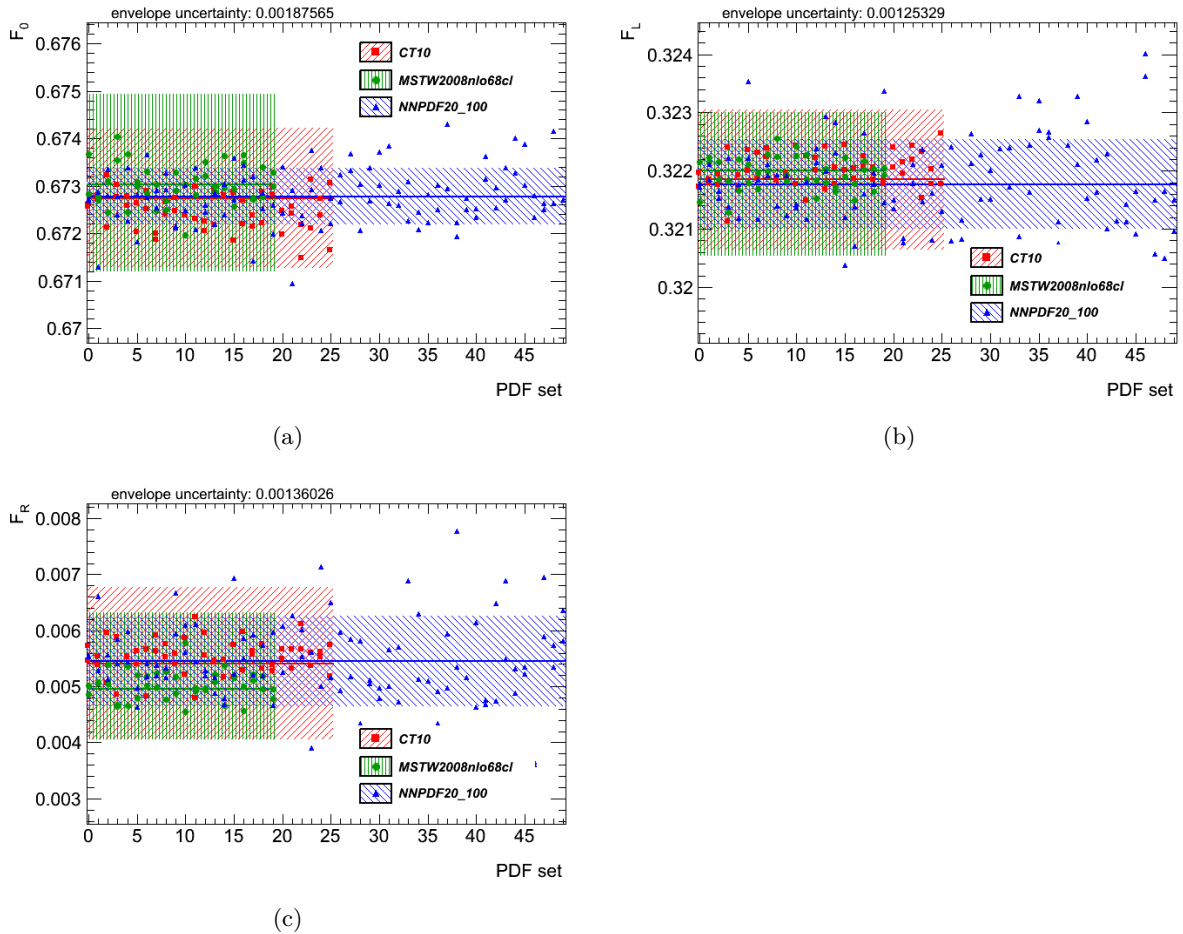
Figure 10.8.: Values for F_0 (a), F_L (b) and F_R (c) from 2 000 ensembles for all PDF sets of CT10, MSTW and NNPDF20. The hashed bands correspond to the intra-PDF uncertainty. The envelope uncertainty is given on top of the plots.

10.2.2. Background Modelling

The background modelling category refers to W+jets, multijet and remaining background processes. Modelling is not only concerned with MC simulation but also with data-driven methods. The relevant systematics are explained in the following.

Background Normalisation

The uncertainty on the background normalisation is taken into account by including a prior on the background templates in the likelihood fit. The width of the prior corresponds to the uncertainty on the background normalisation, including statistical, luminosity and cross-section uncertainty. The cross-section uncertainty on the Z+jets process is 48% for the 4 jets bin [128, 129]. The single top and diboson processes have cross-section uncertainties of 10% and 5%, respectively [129–131]. In the case of the W+jets background, the cross-section uncertainty

is replaced by the uncertainty on the data-driven scale factors (at most 17% [108]), which is propagated to the event yield. The uncertainties on the background priors can be seen in the third column of Tab. 10.3 and amount to ~25% for the W+jets background, ~17% for the summarised single top-quark, Z+jets and diboson backgrounds, ~23% for the summarised multijet background. Finally, the uncertainties are included in the statistical uncertainty of the likelihood estimators.

W+jets Heavy Flavour Composition

The uncertainty on the W+jets heavy flavour scale factors that were introduced in Sect. 7.2.1 includes uncertainties on the W+jets shape, which is taken from MC simulation [108]. Six components modify the W+jets shape, coming from SF variations for the flavour fractions. Up and down variations are provided that only affect the W+jets templates. The systematic shifts
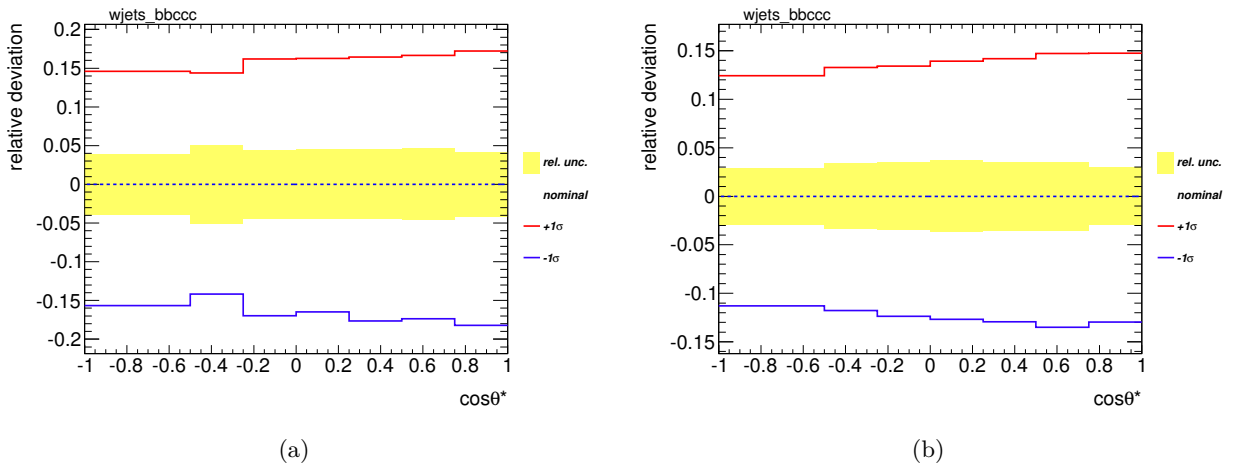
Figure 10.9.: Comparison of relative deviation from one component (`wjets_bbccc`) of the W+jets heavy flavour SFs with the relative statistical uncertainty of the W+jets template in e+jets (a) and μ+jets (b) channel, 1excl b-tag.

caused by one flavour SF on the W+jets template for e+jets and μ+jets channel with 1excl b-tags is compared to the statistical uncertainty of the template in Fig. 10.9. The deviations from all six components can be profiled. In the profile likelihood fit, all other templates but the W+jets template coincide with the nominal templates.

Multijet Background Shape

The uncertainties on the multijet background shape is evaluated differently for e+jets and μ+jets channel.

μ+jets: The multijet background is determined using two matrix methods A and B [129, 130]: these two methods differ by slightly different control regions for determining fake efficiencies. One method parameterises the efficiencies in η and p_T and uses the tag-and-probe method for real efficiencies. The other method takes the real efficiency from MC and does not parameterise it, but takes it as constant. The default multijet estimate is taken as the average from both methods: $(A+B)/2$. The systematic variations are obtained by adding $(A-B)$ as up and down shifts for each bin content. This systematic variation is evaluated via ensemble tests.

e+jets: Variations on the real and fake efficiencies provide up and down variations for both efficiencies independently. These are also evaluated via ensemble tests and added in quadrature.

10.2.3. Detector Modelling

Systematic sources related to the detector modelling can be all included in the profile likelihood fit. However, the influences are different from the various sources and some sources may only be considered for *acceptance profiling* (see Sect. 9.2.2).

Jet Energy Scale

The JES uncertainty has been introduced in Sect. 9.2.1. The 21 subcomponents have been discussed. Seven of them can be considered for usual profiling: the uncertainty due to close-by jets, flavour composition and response, three in-situ nuisance parameters and a theoretical η-intercalibration uncertainty. All other components are considered for acceptance effects. The
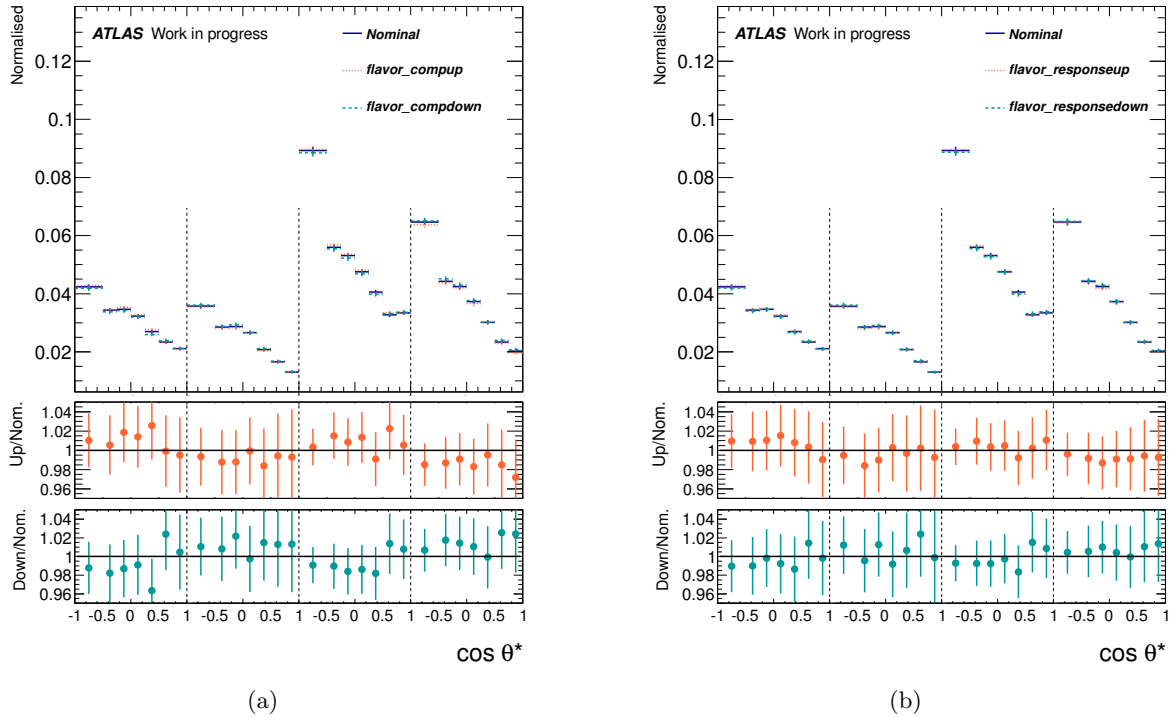
Figure 10.10.: Normalised pseudo-data distribution for (e+jets, 1 excl. b-tag), (e+jets, 2 incl. b-tags) and (μ+jets, 1excl. b-tag), (μ+jets, 2 incl. b-tags) from left to right for samples with flavour composition (a) and flavour response (b) variations by $\pm 1\sigma$. The systematic variation is compared to the nominal distribution.

normalised pseudo-data from the flavour composition and response variations are compared to the nominal pseudo-data in Fig. 10.10. The normalised distributions show shape differences. Therefore, it is expected that a profile likelihood fit is sensitive to these components and can constrain them.

Jet Reconstruction

The jet reconstruction uncertainty is composed of the jet energy resolution (JER), the jet re-construction efficiency (JEFF) and the JVF scale factors. The JER has been introduced in Sect. 9.2.1. The JER variations can be seen in Fig. 10.11 for the pseudo-data and normalised pseudo-data distributions. As pointed out in Sect. 9.2.1, the JER contributes to a shape variation and therefore the profile likelihood is expected to be sensitive to the JER nuisance parameter. This systematic is one-sided and needs to be symmetrised in order to perform the quadratic interpolation. This is done by taking the deviations to the nominal sample for each bin and adding the same deviation in the reverse direction to the nominal bin content. This creates an-other template that is mirrored to the JER template with respect to the nominal template. The
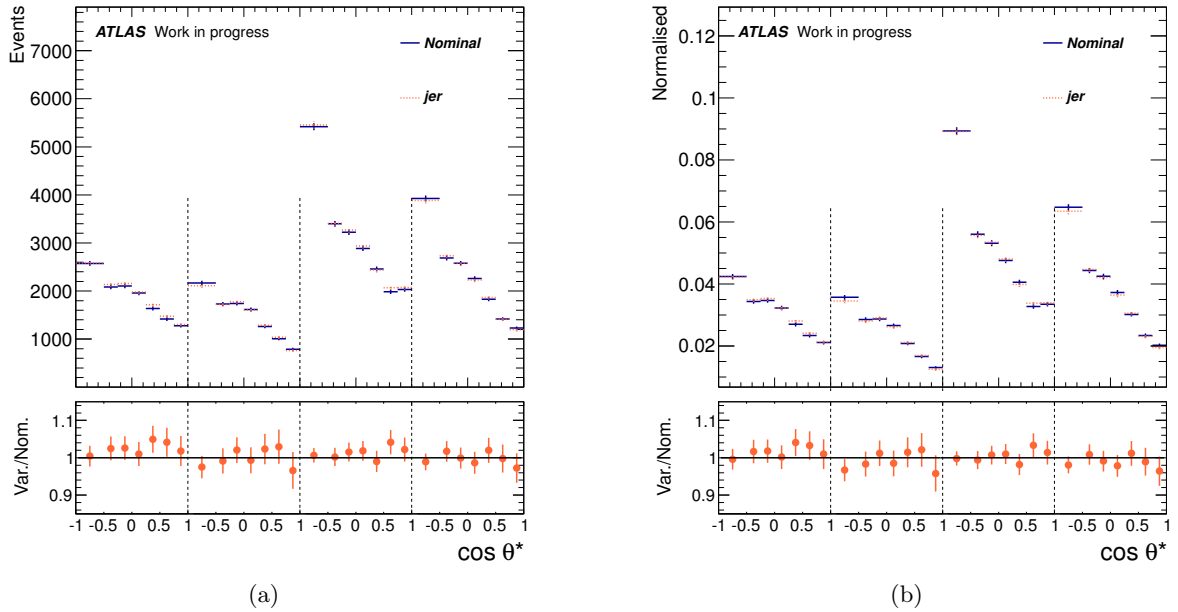
Figure 10.11.: Pseudo-data for (e+jets, 1 excl. b-tag), (e+jets, 2 incl. b-tags) and (μ+jets, 1excl. b-tag), (μ+jets, 2 incl. b-tags) from left to right from JER variation compared with nominal pseudo-data (a). (b) shows the normalised distributions.

uncertainty on the JEFF is assumed to be 2%. According to this uncertainty, reconstructed jets are randomly dropped from events before performing the event selection. Thereby one obtains a one-sided JEFF systematic varied sample that is then also symmetrised like the JER samples. The effect of a JEFF variation turns out to be negligible and this component is therefore only considered for acceptance profiling. The JVF SFs stem from efficiency and mis-tag efficiencies of the JVF cut that has been introduced in Sect. 5.3. The SFs are varied within their uncertainties up and down. This component fulfils the 20% criterion and is considered for usual profiling.

Lepton Energy Scale and Resolution

The lepton energy scale is corrected with the help of $Z \to e^+e^-$ and $Z \to \mu^+\mu^-$ events [132, 133]. The corrections in the e+jets channel is varied within its uncertainties by $\pm 1\sigma$. A one-sided systematic variation in the μ+jets channels is obtained by not applying the energy corrections

to the MC. This one-sided uncertainty is symmetrised like the JER and the JEFF uncertainty. The lepton energy resolution in MC is smeared by default to match the resolution in data. The lepton p_T is smeared with $\pm 1\sigma$. This is done separately for muons in the inner detector and the muon spectrometer. The lepton energy scale and resolution uncertainties do not influence the $\cos\theta^*$ distribution significantly and are included as acceptance nuisance parameters in the combined profile likelihood fit.

Lepton Scale Factors

The lepton efficiency SFs have been discussed in Sect. 9.2.1 and are also determined with $Z \to e^+ e^-$ and $Z \to \mu^+ \mu^-$ auxiliary measurements [132, 133]. The only SFs that are included as usual nuisance parameters are the electron id SF and the muon trigger SF. The other SFs are considered for acceptance profiling. All SF variations cause shifts in $\cos\theta^*$ that are flat, so the usual profiling and the acceptance profiling will be nearly identical. The inclusion of the lepton SFs as nuisance parameters gives the possibilities to change normalisation of the templates independently in e+jets and μ+jets channels, though the templates are merged over all channels (except for the multijet background template). This way the combined profile likelihood fit can adjust the templates to match the data and the normalisation overshoot in the e+jets channel can be corrected.

b-tagging

The treatment of b-tagging related uncertainties has been introduced in Sect. 9.2.1. Nine SF eigenvectors are considered. One component is profiled, the other components were studied including them as acceptance nuisance parameters. The profiling of b-tagging SFs allows to adjust the normalisation in single b-tag bins, thus in each of the four channels separately. This can overcome the description discrepancies observed in the b-tag multiplicity distributions. Fig. 10.12 shows the normalised pseudo-data of variations of *break8* up and down compared with the nominal distribution. It is clearly visible that events migrate from 1excl b-tag bins to 2incl b-tag bins for *break8* up variations. For the down variation the 1excl b-tag bin receives more entries from the 2incl b-tag bins. This behaviour is expected and visible in the ratio plots in Fig. 10.12.

Missing Transverse Momentum

Uncertainties on energy measurements have to be propagated to the $\not{E}_T$ uncertainty. The uncertainty due to the $\not{E}_T$ measurement is evaluated by considering cell-out term variations (100% correlated with soft-jet term) and pile-up variations 1σ up and down. These variations hardly affect the $\cos\theta^*$ distribution and fail the 20% criterion. Therefore, they are only considered as acceptance nuisance parameters.

10.2.4. Method Uncertainties

Template Statistics

The measurement of the W-helicity fractions via a template fit is limited by the available template statistics. The signal samples from PROTOS for pure helicity states were generated with about $1.5 \cdot 10^6$ events each (see exact number in Tab. A.1). After the event selection, this number is highly reduced. Thus, the templates may suffer from a high relative statistical uncertainty due to limited MC statistics. The binning of the $\cos\theta^*$ distribution also influences this uncertainty.
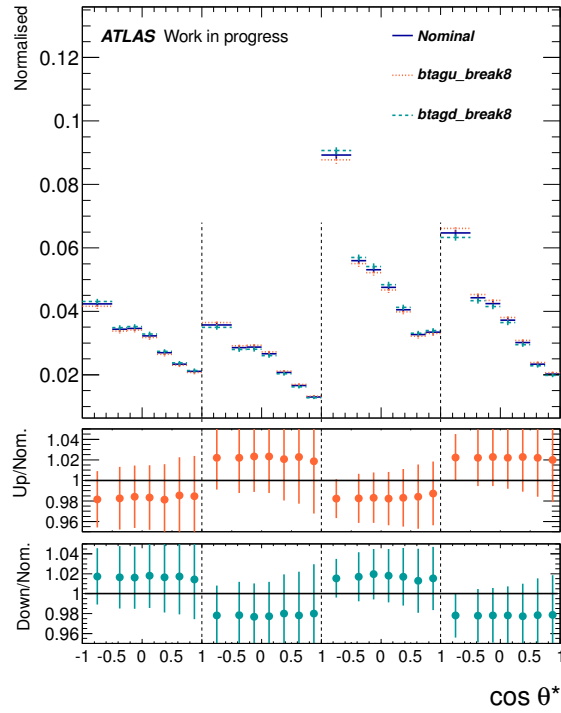
Figure 10.12.: Normalised pseudo-data (e+jets, 1 excl. b-tag), (e+jets, 2 incl. b-tags) and (μ+jets, 1excl. b-tag), (μ+jets, 2 incl. b-tags) from left to right: up and down variations of the relevant b-tagging SF component compared with nominal pseudo-data.

The impact of the limited template statistics on the measured fractions F_i has been evaluated as follows: the templates are not normalised to unity but to the MC luminosity. Then, the individual bin contents are fluctuated with Poissonian probability. Ensemble tests are performed where only the templates are fluctuated while the pseudo-data stays the same. Now the width of the parameter distribution from the fit is taken as uncertainty. All templates are fluctuated simultaneously. Although the MC statistics has been increased by a factor of three for the signal templates compared to the former analysis, the template statistics uncertainty is a dominant uncertainty. Evaluating the influence by fluctuating each template separately reveals that the main contributions to the uncertainty come from the F_0 template and the W+jets template.

All introduced systematic uncertainties are summarised in Tab. 10.2. The treatment of the systematic uncertainties is indicated. In cases where one source of systematic uncertainty consists of several components both acceptance profiling and full profiling of nuisance parameters is possible at the same time. The last column of the table specifies the exact evaluation of the systematic uncertainties in the analysis. The acceptance nuisance parameters of JEFF, JES and b-tagging are omitted from the actual fit, as they have been shown to contribute no significant uncertainty in the profile likelihood fit. In the table they are listed as included as acceptance nuisance parameters.

Source	ensemble test	acc. profiling	full profiling	comments
Signal Modelling				
MC Generator	✓	-	-	full difference
Parton showering	✓	-	-	full difference
ISR/FSR	✓	-	-	half difference
Underlying event	✓	-	-	full difference
Ren./Fac. scale	✓	-	-	full difference
Top-quark mass	✓	-	-	mass dependence
PDF uncertainty	✓	-	-	envelope unc.
Background Modelling				
background norm.	-	-	-	incl. in stat. unc.
W+jets hf scale factor	-	-	✓	six nuis. par.
multijet shape	✓	-	-	full difference
Detector modelling				
Jet energy scale	-	✓	✓	7 full nuis. par. 14 acc. nuis. par.
Jet energy resolution	-	-	✓	symmetrised
Jet reconstruction eff.	-	✓	-	symmetrised
Jet vertex fraction	-	-	✓	1 nuis. par.
Lepton energy scale	-	✓	-	2 nuis. par.
Lepton energy resolution	-	✓	-	3 nuis. par.
Lepton scale factor	-	✓	✓	2 full nuis. par. 4 acc. nuis. par.
b-tagging	-	✓	✓	1 full nuis. par 8 acc. nuis. par.
Missing $\not{E}_T$	-	✓	-	2 nuis. par.
Method uncertainty				
Template statistics	✓	-	-	fraction width

Table 10.2.: Summary of the treatment of all considered systematic uncertainties in the analysis. The check-mark stands for 'yes', otherwise '-' stands for 'no'. The abbreviation hf stands for heavy flavour, Ren./Fac. stands for renormalisation/factorisation, nuis. par. stands for nuisance parameters. The last column details the evaluation in the analysis.

10.3. Combined Fit to Data

The above described systematic treatment is fully included into the profile likelihood fit. The results from this fit are presented in Sect. 10.3.1. The results from a simple ensemble test analysis are compared to the profile likelihood analysis in Sect. 10.3.2.

10.3.1. Results from Profile Fit

The combined profile likelihood fit has been performed in four channels, fitting nine templates to data. In total, 29 nuisance parameters have been included into the fit and were described in Sect. 10.2. The best fit result along with the data points can be seen in Fig. 10.13. The hashed uncertainty bands in the actual fit and in the ratio plot of data over best fit contain the statistical uncertainty plus the systematic uncertainty from all 29 nuisance parameters. The best fit describes the data points very well which is reflected by the low reduced χ^2 and the fit probability of unity which are also given in Fig. 10.13. The fitted quantities are summarised in Tab. 10.3. The fitted helicity fractions are given, the fitted N_i, the fitted background contributions and the k-values for all 29 nuisance parameters. The columns 'Sim.' and '$\sigma_{\text{Sim.}}$' give the values of the mean values and standard deviations, respectively, that are applied on the background priors in the fit. The last column shows how much the fitted background contribution deviates from the input prior mean in units of the input prior standard deviation $\sigma_{\text{Sim.}}$. The fitted background contributions always lie inside the $1\sigma_{\text{Sim.}}$ standard deviation environment around the input value.
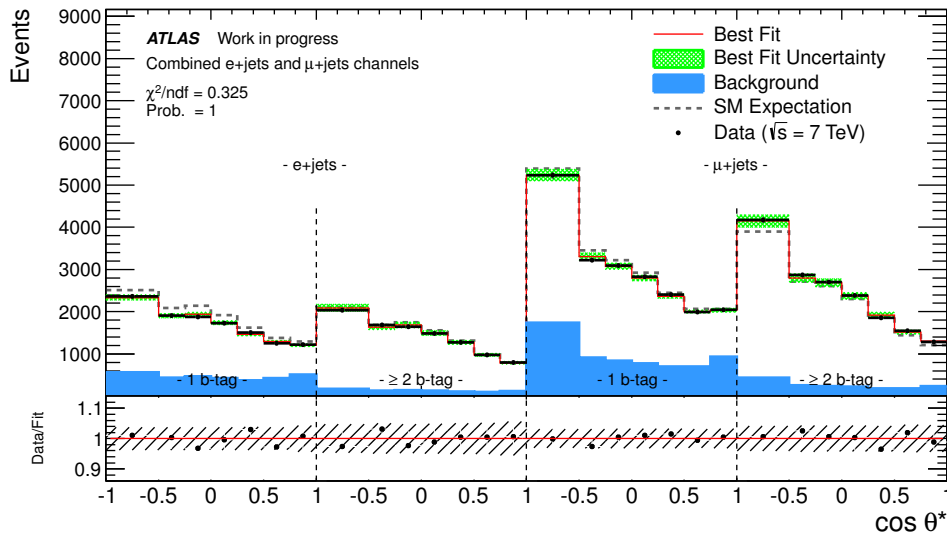
Figure 10.13.: Best fit result of combined profile likelihood fit in four channels with nine templates (red line) compared with data distribution (black points). The hashed uncertainty bands include the statistical uncertainty plus the uncertainty from the fitted nuisance parameters (see text).

It can be also observed that the uncertainty on the background contributions are reduced, especially for the W+jets background. This illustrates how the combined fit is able to constrain this particular background. The fitted nuisance parameters k are also given in Tab. 10.3. The abbreviations EES and EER stand for electron energy scale and electron energy resolution. MUID and MUMS stand for the muon energy resolution systematic smearing in inner detector

and muon spectrometer. MUSC denotes the muon energy scale. The other denotations are self-explanatory. The fitted output values for the background contributions and the nuisance parameters are visualised in Fig. 10.14: the k in the plot for the background templates give the ratio of fitted value over input value. They are all compatible with one which corresponds to the values in the last column in Tab. 10.3. The nuisance parameters k are distributed around $k = 0$. The error bars that are below one (green band for orientation) indicate that the fit was sensitive to the respective nuisance parameters and able to constrain it. Nuisance parameters that lie near zero with an uncertainty of about one hardly influenced the fit and contributed no significant uncertainty to the fitted helicity fractions. The ks corresponding to electron efficiencies were fitted with a value below zero or even below -1 (electron id efficiency). This complies with the observed overshoot from PROTOS in the e+jets channel: the fit prefers lower values and
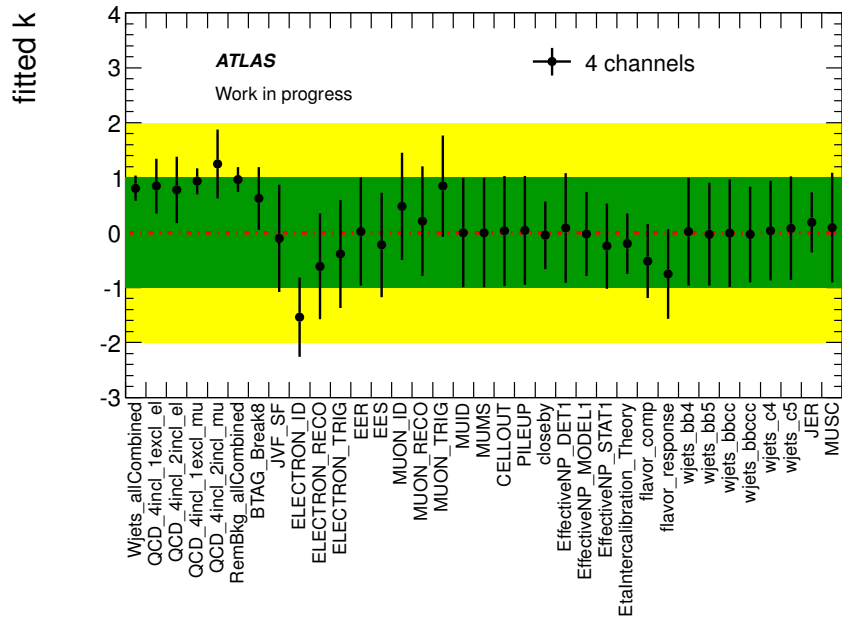
Figure 10.14.: Fitted nuisance parameters in the combined profile likelihood fit with 29 nuisance parameters. The background output-over-input values are shown as well.

thus a lower e+jets event yield. The b-tag related k has a value of about 0.6 which indicates a shift of the event yields in the 1excl b-tag channels down and in the reversed direction for the 2incl b-tag channels. This was expected for the fit to match the data, e.g. by considering the plot in Fig. 7.2(b). The flavour composition and response components are the most sensitive components of the JES, having k-values away from zero.

The uncertainties in Tab. 10.3 on the W-helicity fractions include the systematic uncertainties from all profiled systematic sources. The other missing uncertainties were evaluated as discussed in Sect. 10.2. The corresponding uncertainties are summarised in Tab. 10.4. All uncertainties were added in quadrature and constitute the total uncertainty given in the last row of Tab. 10.4. Dominant uncertainties for the three helicity fractions can be easily identified by looking at Fig. 10.15. Besides the uncertainty from the profile fit (denoted as 'statistical unc.' in the plots), the MC generator uncertainty (F_0 and F_R), the ISR/FSR uncertainty (F_0 and F_R), the top-quark mass uncertainty (F_L and F_R), the fake lepton shape and the limited template statistic contribute the dominant uncertainties.

Parameter	Sim.	$\sigma_{\text{Sim.}}$	Fit	$\sigma(\text{Fit})$	Diff. [$\sigma_{\text{Sim.}}$]
F_0			0.634	0.025	
F_L			0.336	0.015	
F_R			0.030	0.014	
N_0			277 954	15 714	
N_L			147 631	9 639	
N_R			13 190	6 210	
W+jets	7 244	1 770	5 852	843	0.786
multijet ($= 1$ b-tag, e+jets)	678	339	574	178	0.307
multijet (≥ 2 b-tags, e+jets)	160	80	124	75	0.450
multijet ($= 1$ b-tag, μ+jets)	1 557	312	1 454	221	0.330
multijet (≥ 2 b-tags, μ+jets)	273	110	341	102	0.618
RemBkg	4 269	709	4 122	685	0.207
k (BTAG_Break8)			0.620	0.571	
k (JVF_SF)			-0.104	0.976	
k (ELECTRON_ID)			-1.541	0.721	
k (ELECTRON_RECO)			-0.618	0.961	
k (ELECTRON_TRIG)			-0.389	0.985	
k (EER)			0.018	0.981	
k (EES)			-0.225	0.951	
k (MUON_ID)			0.476	0.975	
k (MUON_RECO)			0.209	0.995	
k (MUON_TRIG)			0.846	0.921	
k (MUID)			-0.001	0.994	
k (MUMS)			-0.002	0.995	
k (CELLOUT)			0.031	1.001	
k (PILEUP)			0.039	0.990	
k (closeby)			-0.050	0.614	
k (EffectiveNP_DET1)			0.082	0.998	
k (EffectiveNP_MODEL1)			-0.023	0.765	
k (EffectiveNP_STAT1)			-0.245	0.774	
k (EtaIntercalibration_Theory)			-0.202	0.551	
k (flavor_comp)			-0.517	0.672	
k (flavor_response)			-0.751	0.816	
k (wjets_bb4)			0.018	0.980	
k (wjets_bb5)			-0.030	0.936	
k (wjets_bbcc)			-0.013	0.975	
k (wjets_bbccc)			-0.035	0.867	
k (wjets_c4)			0.036	0.908	
k (wjets_c5)			0.079	0.943	
k (JER)			0.189	0.546	
k (MUSC)			0.093	0.999	

Table 10.3.: Fit results from combined profile likelihood fit to data. The multijet background templates are not merged, all other templates are coupled over the four channels. The mean and width of the background priors are given in the first two columns. The last column displays the differences in $\sigma_{\text{Sim.}}$ of the fitted background contribution to the input value. The fitted uncertainties include statistical plus uncertainties from the 29 nuisance parameters.

Category	$\sigma(F_0)$	$\sigma(F_L)$	$\sigma(F_R)$
Stat. + Det.Mod. unc.	0.025	0.015	0.014
Signal and background modelling			
MC Generator	0.008	0.001	0.008
Parton showering	0.001	0.002	0.001
ISR/FSR	0.007	0.002	0.006
Underlying event	0.003	0.002	0.001
Ren./Fac. Scale	0.002	0.002	0.000
Top mass (1.4 GeV)	0.002	0.013	0.015
PDF	0.002	0.001	0.001
Fake lepton shape	0.010	0.006	0.004
Method uncertainties			
Template stat.	0.011	0.007	0.006
Total uncertainty	0.031	0.022	0.024

Table 10.4.: Table of uncertainties for the four channel fit. The Stat. + Det.Mod. uncertainty includes JES, JER, b-tagging, lepton SF, LER, LES, $\not{E}_T$ and W+jets heavy flavour SF uncertainties (from profile fit).
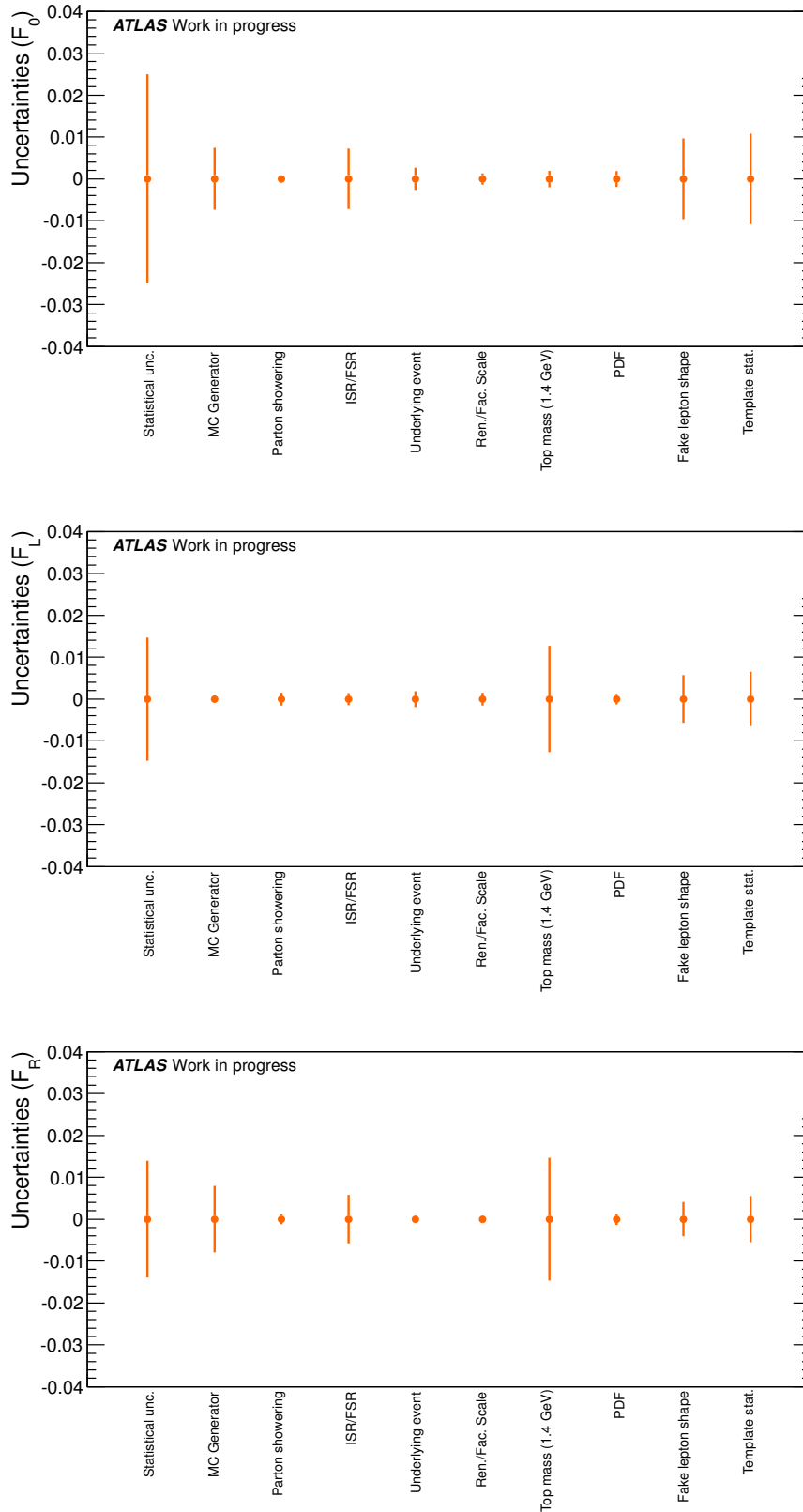
Figure 10.15.: Summary of uncertainty components from the four channel fit for the three helicity fractions. The statistical uncertainty also includes detector modelling uncertainties and W+jets heavy flavour SF uncertainties.

The results from the combined profile likelihood fit in four channels with nine templates finally read:

$$F_0 = 0.634 \pm 0.031,$$
$$F_L = 0.337 \pm 0.022,$$
$$F_R = 0.030 \pm 0.024.$$

(10.1)

To be able to compare these results for the W-helicity fractions with NNLO QCD prediction, the results of F_0 and F_L are plotted in a 2-dimensional plane. The correlation between F_0 and F_L has to be calculated to be able to draw the error ellipse around the F_0-F_L measured point. The correlation amounts to $\varrho(F_0, F_L) = -0.646$, the error ellipse is drawn in Fig. 10.16 and covers the 68% confidence region. The SM prediction is indicated by the solid rectangle. The error ellipse does not cover the SM prediction, but is not significantly away.
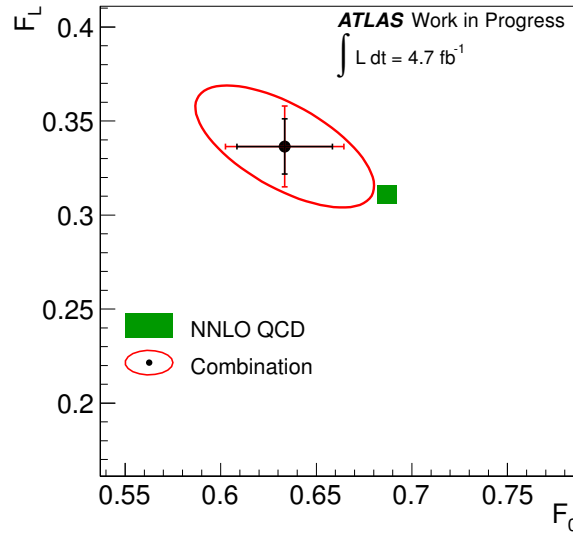
Figure 10.16.: Best-fit result from four channel fit in F_0-F_L plane: the fitted value and the corresponding error ellipse are shown together with the NNLO QCD prediction (rectangle).

The same analysis has been repeated with a combined fit in six channels with eleven templates where again all templates are merged but the multijet background templates. The best fit can be seen in Fig. 10.17 along with data points. Also here, a good description of the data is achieved by the profile likelihood fit (low reduced χ^2, probability close to one). The same uncertainties as in the four channel profile fit were evaluated here via profiling. Table 10.5 summarises the uncertainties for the six channel fit. The total uncertainties are slightly lower than for the four channel fit. Finally, the results for the six channel fit for the W-helicity fractions read:

$$F_0 = 0.632 \pm 0.030$$
$$F_L = 0.345 \pm 0.023$$
$$F_R = 0.024 \pm 0.022$$

The calculated correlation between F_0 and F_L is $\varrho(F_0, F_L) = -0.702$.
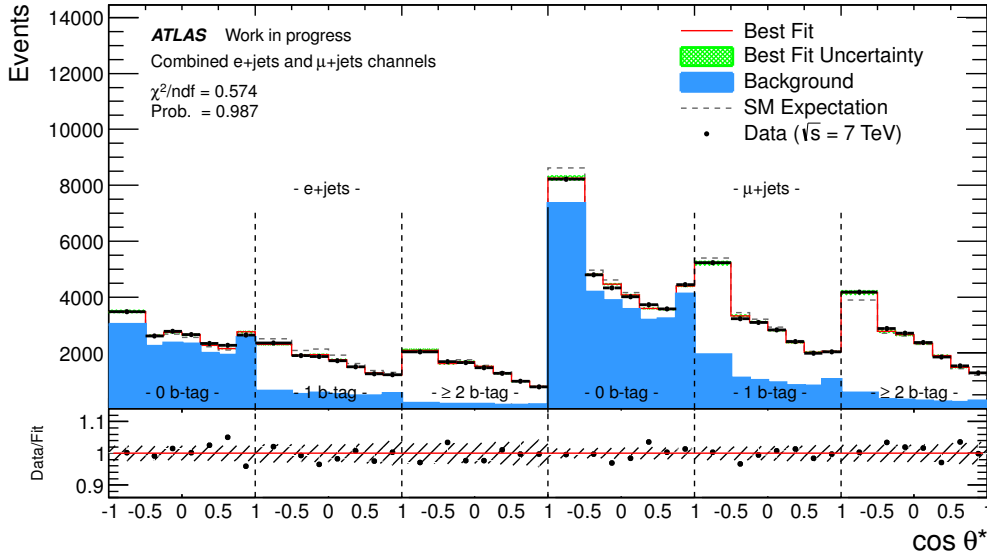
Figure 10.17.: Best fit result from combined profile likelihood fit to six channels with eleven templates (red line) compared to data. The hashed uncertainty bands include the statistical uncertainty plus the uncertainty from the fitted nuisance parameters (see text).

Category	$\sigma(F_0)$	$\sigma(F_L)$	$\sigma(F_R)$
Stat. + Det.Mod. unc.	0.024	0.015	0.011
Signal and background modelling			
MC Generator	0.008	0.001	0.009
Parton showering	0.000	0.001	0.001
ISR/FSR	0.006	0.007	0.001
Underlying event	0.002	0.001	0.001
Ren./Fac. Scale	0.003	0.002	0.001
Top mass (1.4 GeV)	0.001	0.012	0.014
PDF	0.002	0.001	0.002
Fake lepton shape	0.010	0.007	0.005
Method uncertainties			
Template stat.	0.011	0.007	0.007
Total uncertainty	0.030	0.023	0.022

Table 10.5.: Table of uncertainties for the six channel fit. Stat. + Det.Mod. uncertainty includes JES, JER, b-tagging, lepton SF, LER, LES, $\not{E}_T$ and W+jets heavy flavour SF uncertainties (from profile fit).

10.3.2. Results from Ensemble Testing

The whole analysis is repeated evaluating all systematic sources via ensemble tests. The profiled systematic sources in Sect. 10.3.1 mostly provided $\pm 1\sigma$ variations. Here, ensemble tests are performed with these variations. The largest difference in F_i is taken as symmetrised uncertainty due to the responsible source. In case of one-sided systematics, only one difference in F_i is obtained by the ensemble test evaluation and taken as the respective symmetrised uncertainty. All uncertainties obtained from ensemble testing are summarised in Tab. 10.6. The total uncertainty is given in the last row and was obtained by adding up all single uncertainties in quadrature. It can be observed that the profile likelihood analysis exceeds the precision of ensemble testing significantly, reducing the uncertainty on F_0 by more than a factor of 2. Fig. 10.18 helps to identify the dominant uncertainties of the ensemble test evaluation. Besides the statistical uncertainty, the JES and JER uncertainties are dominant systematic uncertainties. The JES is composed of all 21 subcomponents that were added up in quadrature. The same has been done with the b-tagging SF components that contribute another dominant uncertainty. The lepton energy scale and the $\not{E}_T$ uncertainty give also notable contributions to the total uncertainty. All these systematics could be reduced in a profile likelihood fit giving the foundation of the highly improved measurement presented in Sect. 10.3.1.

Category	$\sigma(F_0)$	$\sigma(F_L)$	$\sigma(F_R)$
Statistical unc.	0.022	0.014	0.010
Detector modelling			
Jet energy scale	0.036	0.017	0.023
Jet energy res.	0.035	0.023	0.011
Jet reconstruction eff.	0.002	0.001	0.001
JVF SF	0.000	0.000	0.000
Lepton energy scale	0.008	0.001	0.008
Lepton energy res.	0.003	0.002	0.002
Lepton SF	0.003	0.002	0.002
B-tagging	0.019	0.007	0.013
Missing E_T	0.016	0.006	0.010
Signal and background modelling			
MC Generator	0.008	0.001	0.008
Parton showering	0.001	0.002	0.001
ISR/FSR	0.007	0.002	0.006
Underlying event	0.003	0.002	0.001
Ren./Fac. Scale	0.002	0.002	0.000
Top mass (1.4 GeV)	0.002	0.013	0.015
PDF	0.002	0.001	0.001
W+jets HF	0.006	0.002	0.005
Fake lepton shape	0.010	0.006	0.004
Method uncertainties			
Template stat.	0.011	0.007	0.006
Total uncertainty	0.064	0.037	0.039

Table 10.6.: Table of uncertainties for four channel fit with nine templates. All systematics were evaluated via ensemble tests with 2 000 ensembles each.
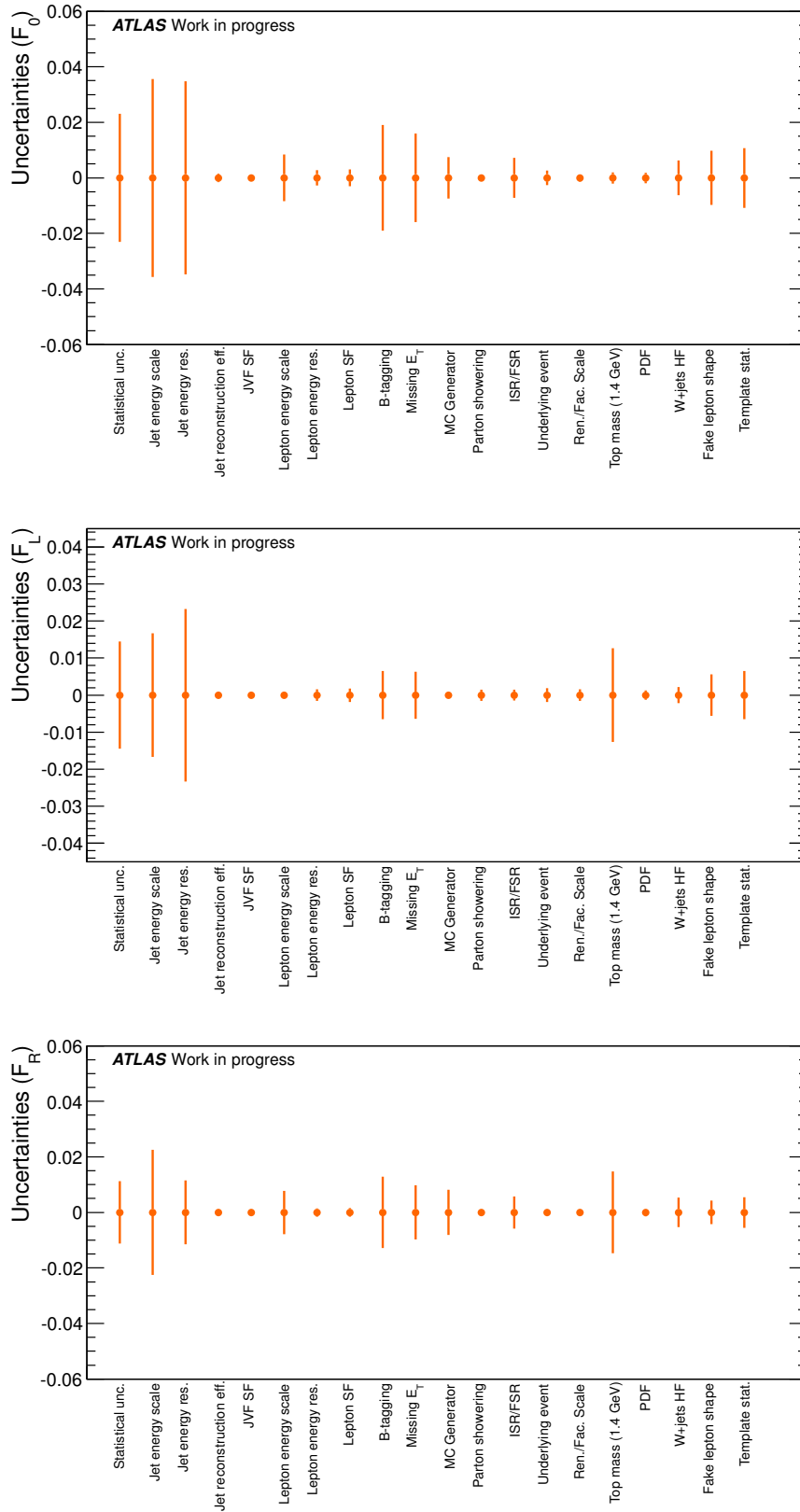
Figure 10.18.: Summary of uncertainty components from the four channel fit for the three helicity fractions. The systematic uncertainties were obtained performing 2 000 ensemble tests each.

10.4. Limits on Anomalous Couplings

From the results in Eq. 10.1, limits are derived on the anomalous couplings g_R and g_L (real parts) that were introduced in Eq. 3.5. The same approach is followed as used in [60]. An effective field theory formalism is used to derive the functional dependence of the helicity fractions on the anomalous couplings [62–64]. Thereby $V_L = V_{tb}$ is set to unity and V_R is set to zero. The helicity fractions are functions like $F_i(g_L, g_R, m_t, m_W, \dots)$. For each point in the g_L-g_R space the probability from the measured values in Eq. 10.1 is calculated. Thereby the correlation of $\varrho(F_0, F_L) = -0.646$ is taken into account. Finally, limits are set in this g_L-g_R space analogue to the ones shown in Fig. 3.11. The resulting allowed regions are shown in Fig. 10.19: Not only 68% and 95% confidence level regions are shown, but also a 99% confidence level region. Again, from the W-helicity fractions measurement, a region with non-zero g_R is allowed (upper, disconnected region), that has been excluded by single top-quark cross-section measurements [65–67]. This region occurres as a second solution to the quadratic equation emerging from the dependence of the helicity fractions on the anomalous couplings. The SM expectation of $g_R = g_L = 0$ is contained in the other allowed region within the 95% confidence interval (yellow area in Fig. 10.19). Thus, the limits in the g_R-g_L space are compatible with the SM expectation.
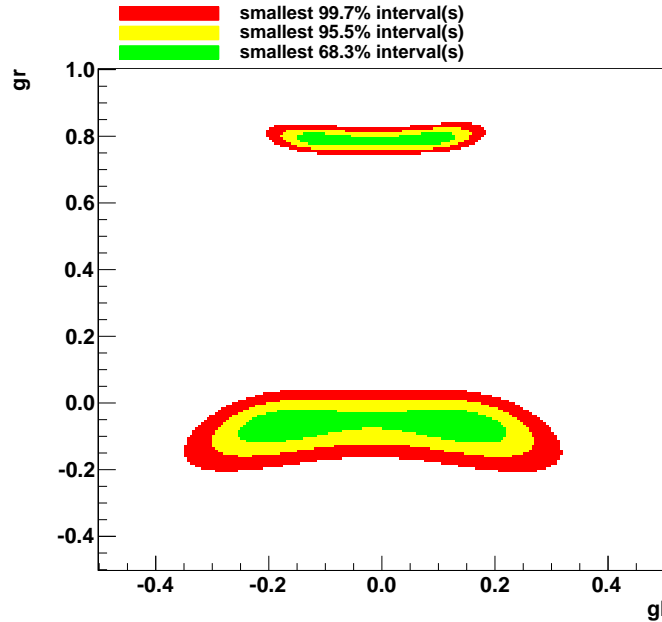

Figure 10.19.: Allowed regions according to 68.3%, 95.5% and 99.7% confidence intervals for g_L and g_R (real parts) from the measured helicity fractions in Eq. 10.1 and a correlation of $\varrho(F_0, F_L) = -0.646$. V_L is set to one and V_R is set to zero.

11. Summary and Outlook

A measurement of the W-helicity fractions in top-quark decays was presented. The measurement uses the full 2011 data set corresponding to an integrated luminosity of $4.7\,\text{fb}^{-1}$, recorded by the ATLAS detector. The analysis is performed in the ℓ+jets channel of top-quark pair events. The event selection requires exactly one high energetic and isolated lepton, at least four jets of which at least one has to be identified as a b-jet and missing transverse momentum. The selected events are fully reconstructed with the help of the kinematic likelihood fitter KLFitter. The event reconstruction allows the reconstruction of the angular variable $\cos\theta^*$. This variable serves as a spin analyser of the W-boson. The three different possible helicity states (longitudinal polarised, left- and right-handed) have different distributions in $\cos\theta^*$. A combined profile likelihood fit is performed to the data distribution in $\cos\theta^*$ to extract the W-helicity fractions F_0, F_L and F_R. The combined fit is performed in four channels simultaneously, namely the e+jets and μ+jets channels with 1 exclusive and 2 inclusive b-tag bins. Uncertainties that are not suited for profiling were evaluated via ensemble tests. The final results for the helicity fractions are:

$$F_0 = 0.634 \pm 0.031,$$
$$F_L = 0.337 \pm 0.022,$$
$$F_R = 0.030 \pm 0.024.$$

A cross-check of this measurement has been performed via a combined fit in six channels including 0 exclusive b-tag control regions for the e+jets and μ+jets channel. The result from this fit is in agreement with the above quoted results. The precision of this measurement significantly exceeds the one from the standard analysis with ensemble test evaluation of systematic uncertainties only (Sect. 10.3.2). The profile likelihood analysis demonstrated its full strength leading to uncertainties reduced by factors of 2.1 for $\sigma(F_0)$ and 1.7 for $\sigma(F_L)$ and 1.6 for $\sigma(F_R)$ compared to the pure ensemble test analysis.

Fig. 11.1 compares the result with former measurements, all performed with $\sqrt{s} = 7\,\text{TeV}$ data: the ATLAS combination of four measurements (ℓ+jets and dilepton channel with template method and asymmetry method) [58], the LHC combination [60] and the most recent measurement performed by CMS in the ℓ+jets channel using a reweighting method [68]. The measured helicity fractions are compatible with all former measurements shown in Fig. 11.1. The measurement is consistent with the NNLO QCD predictions within slightly more than one standard deviation. The precision on F_0 and F_L exceed the ones from the shown previous analyses. The measurement of F_R however is less precise than the one performed by CMS (see Eq. 3.10). The dominant uncertainties in the CMS measurement are the W+jets background normalisation, the $t\bar{t}$ signal modelling (including uncertainties on the choice of μ_R^2 and μ_F^2 and the top-quark mass uncertainty), the limited statistics of the simulated samples and the statistical uncertainty on the fraction estimators in the likelihood fit.

The limits set on the real parts of the anomalous couplings g_R and g_L are of similar strength as the CMS limits and include the SM expectation in the 95% confidence interval.

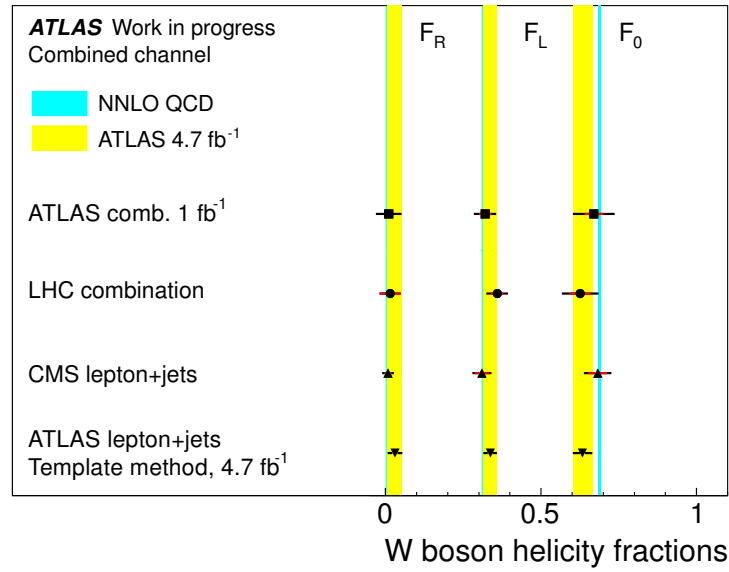***Figure 11.1.:*** Comparison of analysis results with the previous ATLAS combination [58], the LHC combination [60] and the CMS result in the ℓ+jets channel [68]. All measurements were performed at $\sqrt{s} = 7$ TeV. The NNLO QCD prediction [1] is indicated by the cyan-blue band. The yellow band belongs to the 1σ environment of the presented measurement from the four channel combined profile likelihood fit.

Outlook

The presented measurement is the most precise measurement of the W-helicity in top-quark decays performed with the ATLAS detector. The precision also competes with the most recent CMS measurement. Nevertheless, there are possibilities to improve the measurement further. Ideas are to assimilate the e+jets channel selection to the μ+jets channel selection: the e+jets channel suffers from less events due to the tighter selection cuts. An improvement in the statistical uncertainty can be achieved by changing the e+jets selection accordingly and reducing the statistical uncertainty in data. It has been observed that MC generators have problems to describe the b-tag multiplicity in data. This may be due to the used MV1 tagger at the 70% working point. It may be promising to move to a higher working point which means a higher efficiency: this way more events will be selected, at the same time the $t\bar{t}$ purity of the selected samples will be reduced. The benefit of this change has to be studied. A dominant uncertainty is due to the limited template statistics available. A method to decrease this uncertainty may be to not apply b-tagging cuts in the selection but to follow a tag-rate-function approach. This approach assigns weights to the events in a pre-tag selection according to the tagging efficiency (η, p_T and true jet-flavour dependent). The normalisation and shape after b-tag cuts are then predicted without reducing the MC statistics.

Most recently, a new combination of ATLAS and CMS measurements of the top-quark mass resulted in an improved precision [134]: the total uncertainty is 0.95 GeV/c^2 instead of 1.4 GeV/c^2 that was assumed in the analysis. This will lead to a decreased uncertainty on the helicity fractions due to the top-quark mass uncertainty.

Another goal is to additionally include information from ± 2 and $\pm 3\sigma$ systematic shifts into the profiling as it has been illustrated in Sect. 8.3.2, Fig. 8.3. These shifts are available only for the JES components. They have not been taken into account here due to time constraints.

In Sect. 3.4.1, different spin analysers apart from $\cos\theta^*$ have been introduced, like the lepton p_T and the invariant mass $m_{\ell b}$. As pointed out in Sect. 7.5.1, discrepancies are observed between MC and data for the lepton p_T distribution. Therefore, to follow an approach using this variable, the data/MC agreement needs to be better understood. For future analyses, it may be beneficial to include the information from all of the spin-analysers into a likelihood discriminant in a multivariate analysis. The 2012 data set provides statistics of more than five times of the currently analysed data set. This promises to increase the statistical precision further.

A. Appendix

A.1. Monte Carlo Samples

A.1.1. Signal Processes

Process	Generator	Showering	PDF	# events
$t\bar{t}$ ℓ+jets	PROTOS	PYTHIA	CTEQ6L1	498 999
$t\bar{t}$ dilepton	PROTOS	PYTHIA	CTEQ6L1	499 500
PROTOS pure helicity states:				
$t\bar{t}$ ℓ+jets, F_0	PROTOS	PYTHIA	CTEQ6L1	1 500 000
$t\bar{t}$ ℓ+jets, F_L	PROTOS	PYTHIA	CTEQ6L1	1 499 494
$t\bar{t}$ ℓ+jets, F_R	PROTOS	PYTHIA	CTEQ6L1	1 488 998
$t\bar{t}$ dilepton, F_0	PROTOS	PYTHIA	CTEQ6L1	1 497 998
$t\bar{t}$ dilepton, F_L	PROTOS	PYTHIA	CTEQ6L1	1 498 701
$t\bar{t}$ dilepton, F_R	PROTOS	PYTHIA	CTEQ6L1	1 498 499

Table A.1.: Sample information for the $t\bar{t}$ signal process used in the analysis. The information is given for the SM configuration (first two rows) as well as for the pure helicity states F_0, F_L and F_R.

A.1.2. Background Processes

Process	Generator	Showering	PDF	# events	σ [pb]
$W(\to e\nu_e)$ Np0	ALPGEN	HERWIG	CTEQ6L1	6 952 874	6 930.50
$W(\to e\nu_e)$ Np1	ALPGEN	HERWIG	CTEQ6L1	4 998 487	1 305.30
$W(\to e\nu_e)$ Np2	ALPGEN	HERWIG	CTEQ6L1	3 768 632	378.13
$W(\to e\nu_e)$ Np3	ALPGEN	HERWIG	CTEQ6L1	1 008 947	101.86
$W(\to e\nu_e)$ Np4	ALPGEN	HERWIG	CTEQ6L1	744 998	25.68
$W(\to e\nu_e)$ Np5	ALPGEN	HERWIG	CTEQ6L1	419 947	6.99
$W(\to \mu\nu_\mu)$ Np0	ALPGEN	HERWIG	CTEQ6L1	6 962 239	6 932.40
$W(\to \mu\nu_\mu)$ Np1	ALPGEN	HERWIG	CTEQ6L1	4 998 236	1 305.90
$W(\to \mu\nu_\mu)$ Np2	ALPGEN	HERWIG	CTEQ6L1	3 768 737	378.07
$W(\to \mu\nu_\mu)$ Np3	ALPGEN	HERWIG	CTEQ6L1	1 008 446	101.85
$W(\to \mu\nu_\mu)$ Np4	ALPGEN	HERWIG	CTEQ6L1	754 898	25.72
$W(\to \mu\nu_\mu)$ Np5	ALPGEN	HERWIG	CTEQ6L1	418 496	7.00
$W(\to \tau\nu_\tau)$ Np0	ALPGEN	HERWIG	CTEQ6L1	3 418 296	6 931.80
$W(\to \tau\nu_\tau)$ Np1	ALPGEN	HERWIG	CTEQ6L1	2 499 194	1 304.90
$W(\to \tau\nu_\tau)$ Np2	ALPGEN	HERWIG	CTEQ6L1	3 750 928	377.93
$W(\to \tau\nu_\tau)$ Np3	ALPGEN	HERWIG	CTEQ6L1	1 009 946	101.96
$W(\to \tau\nu_\tau)$ Np4	ALPGEN	HERWIG	CTEQ6L1	249 998	25.71
$W(\to \tau\nu_\tau)$ Np5	ALPGEN	HERWIG	CTEQ6L1	65 000	7.00
Wbb Np0	ALPGEN	HERWIG	CTEQ6L1	474 997	47.35
Wbb Np1	ALPGEN	HERWIG	CTEQ6L1	205 500	35.76
Wbb Np2	ALPGEN	HERWIG	CTEQ6L1	174 499	17.33
Wbb Np3	ALPGEN	HERWIG	CTEQ6L1	69 999	7.61
Wcc Np0	ALPGEN	HERWIG	CTEQ6L1	1 274 846	127.53
Wcc Np1	ALPGEN	HERWIG	CTEQ6L1	1 049 847	104.68
Wcc Np2	ALPGEN	HERWIG	CTEQ6L1	524 947	52.08
Wcc Np3	ALPGEN	HERWIG	CTEQ6L1	170 000	16.96
Wc Np0	ALPGEN	HERWIG	CTEQ6L1	6 497 837	644.4
Wc Np1	ALPGEN	HERWIG	CTEQ6L1	2 069 646	205.0
Wc Np2	ALPGEN	HERWIG	CTEQ6L1	519 974	50.8
Wc Np3	ALPGEN	HERWIG	CTEQ6L1	115 000	11.4
Wc Np4	ALPGEN	HERWIG	CTEQ6L1	30 000	2.8
WW	HERWIG	HERWIG	MRST	2 489 242	11.5003
ZZ	HERWIG	HERWIG	MRST	249 999	0.9722
WZ	HERWIG	HERWIG	MRST	999 896	3.4641

Table A.2.: Sample information for the W+jets and diboson background processes used in the analysis. NpX denotes the number of X additional partons.

Process	Gen.	Shower.	PDF	# events	σ [pb]
$Z(\to e^+e^-)$ Np0	ALPGEN	HERWIG	CTEQ6L1	6 618 284	668.32
$Z(\to e^+e^-)$ Np1	ALPGEN	HERWIG	CTEQ6L1	1 334 897	134.36
$Z(\to e^+e^-)$ Np2	ALPGEN	HERWIG	CTEQ6L1	2 004 195	40.54
$Z(\to e^+e^-)$ Np3	ALPGEN	HERWIG	CTEQ6L1	549 949	11.16
$Z(\to e^+e^-)$ Np4	ALPGEN	HERWIG	CTEQ6L1	149 948	2.88
$Z(\to e^+e^-)$ Np5	ALPGEN	HERWIG	CTEQ6L1	50 000	0.83
$Z(\to \mu^+\mu^-)$ Np0	ALPGEN	HERWIG	CTEQ6L1	6 615 230	668.68
$Z(\to \mu^+\mu^-)$ Np1	ALPGEN	HERWIG	CTEQ6L1	1 334 296	134.14
$Z(\to \mu^+\mu^-)$ Np2	ALPGEN	HERWIG	CTEQ6L1	1 999 727	40.33
$Z(\to \mu^+\mu^-)$ Np3	ALPGEN	HERWIG	CTEQ6L1	549 896	11.19
$Z(\to \mu^+\mu^-)$ Np4	ALPGEN	HERWIG	CTEQ6L1	150 000	2.75
$Z(\to \mu^+\mu^-)$ Np5	ALPGEN	HERWIG	CTEQ6L1	50 000	0.77
$Z(\to \tau^+\tau^-)$ Np0	ALPGEN	HERWIG	CTEQ6L1	10 613 179	668.40
$Z(\to \tau^+\tau^-)$ Np1	ALPGEN	HERWIG	CTEQ6L1	3 334 137	134.81
$Z(\to \tau^+\tau^-)$ Np2	ALPGEN	HERWIG	CTEQ6L1	1 004 847	40.36
$Z(\to \tau^+\tau^-)$ Np3	ALPGEN	HERWIG	CTEQ6L1	509 847	11.25
$Z(\to \tau^+\tau^-)$ Np4	ALPGEN	HERWIG	CTEQ6L1	144 999	2.79
$Z(\to \tau^+\tau^-)$ Np5	ALPGEN	HERWIG	CTEQ6L1	45 000	0.77
$Z(e^+e^-)$ Np0 ($m_{\ell\ell} = 10\text{-}40$ GeV)	ALPGEN	HERWIG	CTEQ6L1	994 949	3 055.20
$Z(e^+e^-)$ Np1 ($m_{\ell\ell} = 10\text{-}40$ GeV)	ALPGEN	HERWIG	CTEQ6L1	299 998	84.92
$Z(e^+e^-)$ Np2 ($m_{\ell\ell} = 10\text{-}40$ GeV)	ALPGEN	HERWIG	CTEQ6L1	999 946	41.40
$Z(e^+e^-)$ Np3 ($m_{\ell\ell} = 10\text{-}40$ GeV)	ALPGEN	HERWIG	CTEQ6L1	149 998	8.38
$Z(e^+e^-)$ Np4 ($m_{\ell\ell} = 10\text{-}40$ GeV)	ALPGEN	HERWIG	CTEQ6L1	40 000	1.85
$Z(e^+e^-)$ Np5 ($m_{\ell\ell} = 10\text{-}40$ GeV)	ALPGEN	HERWIG	CTEQ6L1	10 000	0.46
$Z(\mu^+\mu^-)$ Np0 ($m_{\ell\ell} = 10\text{-}40$ GeV)	ALPGEN	HERWIG	CTEQ6L1	999 849	3 054.90
$Z(\mu^+\mu^-)$ Np1 ($m_{\ell\ell} = 10\text{-}40$ GeV)	ALPGEN	HERWIG	CTEQ6L1	300 000	84.87
$Z(\mu^+\mu^-)$ Np2 ($m_{\ell\ell} = 10\text{-}40$ GeV)	ALPGEN	HERWIG	CTEQ6L1	999 992	41.45
$Z(\mu^+\mu^-)$ Np3 ($m_{\ell\ell} = 10\text{-}40$ GeV)	ALPGEN	HERWIG	CTEQ6L1	150 000	8.38
$Z(\mu^+\mu^-)$ Np4 ($m_{\ell\ell} = 10\text{-}40$ GeV)	ALPGEN	HERWIG	CTEQ6L1	39 999	1.85
$Z(\mu^+\mu^-)$ Np5 ($m_{\ell\ell} = 10\text{-}40$ GeV)	ALPGEN	HERWIG	CTEQ6L1	10 000	0.46
$Z(\tau^+\tau^-)$ Np0 ($m_{\ell\ell} = 10\text{-}40$ GeV)	ALPGEN	HERWIG	CTEQ6L1	999 649	3 055.10
$Z(\tau^+\tau^-)$ Np1 ($m_{\ell\ell} = 10\text{-}40$ GeV)	ALPGEN	HERWIG	CTEQ6L1	299 999	84.93
$Z(\tau^+\tau^-)$ Np2 ($m_{\ell\ell} = 10\text{-}40$ GeV)	ALPGEN	HERWIG	CTEQ6L1	498 899	41.47
$Z(\tau^+\tau^-)$ Np3 ($m_{\ell\ell} = 10\text{-}40$ GeV)	ALPGEN	HERWIG	CTEQ6L1	150 000	8.36
$Z(\tau^+\tau^-)$ Np4 ($m_{\ell\ell} = 10\text{-}40$ GeV)	ALPGEN	HERWIG	CTEQ6L1	39 999	1.85
$Z(\tau^+\tau^-)$ Np5 ($m_{\ell\ell} = 10\text{-}40$ GeV)	ALPGEN	HERWIG	CTEQ6L1	10 000	0.46

Table A.3.: Sample information for the Z+jets background processes used in the analysis. NpX denotes the number of X additional partons.

Process	Generator	Showering	PDF	# events	σ [pb]
$Z(\to e^+e^-)bb$ Np0	ALPGEN	HERWIG	CTEQ6L1	409 832	6.57
$Z(\to e^+e^-)bb$ Np1	ALPGEN	HERWIG	CTEQ6L1	160 000	2.48
$Z(\to e^+e^-)bb$ Np2	ALPGEN	HERWIG	CTEQ6L1	60 000	0.89
$Z(\to e^+e^-)bb$ Np3	ALPGEN	HERWIG	CTEQ6L1	30 000	0.39
$Z(\to \mu^+\mu^-)bb$ Np0	ALPGEN	HERWIG	CTEQ6L1	409 949	6.56
$Z(\to \mu^+\mu^-)bb$ Np1	ALPGEN	HERWIG	CTEQ6L1	155 000	2.47
$Z(\to \mu^+\mu^-)bb$ Np2	ALPGEN	HERWIG	CTEQ6L1	60 000	0.89
$Z(\to \mu^+\mu^-)bb$ Np3	ALPGEN	HERWIG	CTEQ6L1	29 999	0.39
$Z(\to \tau^+\tau^-)bb$ Np0	ALPGEN	HERWIG	CTEQ6L1	150 000	6.57
$Z(\to \tau^+\tau^-)bb$ Np1	ALPGEN	HERWIG	CTEQ6L1	99 999	2.49
$Z(\to \tau^+\tau^-)bb$ Np2	ALPGEN	HERWIG	CTEQ6L1	40 000	0.89
$Z(\to \tau^+\tau^-)bb$ Np3	ALPGEN	HERWIG	CTEQ6L1	9 000	0.39

Table A.4.: Sample information for the *Zbb*+jets background processes used in the analysis. NpX denotes the number of X additional partons.

Process	Generator	Showering	PDF	# events	σ [pb]
Single top (s-chan., $W \to e\nu_e$)	MC@NLO	HERWIG	CT10	253 410	0.47
Single top (s-chan., $W \to \mu\nu_\mu$)	MC@NLO	HERWIG	CT10	253 594	0.47
Single top (s-chan., $W \to \tau\nu_\tau$)	MC@NLO	HERWIG	CT10	253 511	0.47
Single top (associated Wt prod.)	MC@NLO	HERWIG	CT10	797 024	14.59
Single top (t-chan., $W \to e\nu_e$)	ACERMC	PYTHIA	MRST	999 295	8.06
Single top (t-chan., $W \to \mu\nu_\mu$)	ACERMC	PYTHIA	MRST	999 948	8.06
Single top (t-chan., $W \to \tau\nu_\tau$)	ACERMC	PYTHIA	MRST	845 149	8.05

Table A.5.: Sample information for the single top-quark background processes used in the analysis.

A.2. Control Plots - Kinematic Distributions
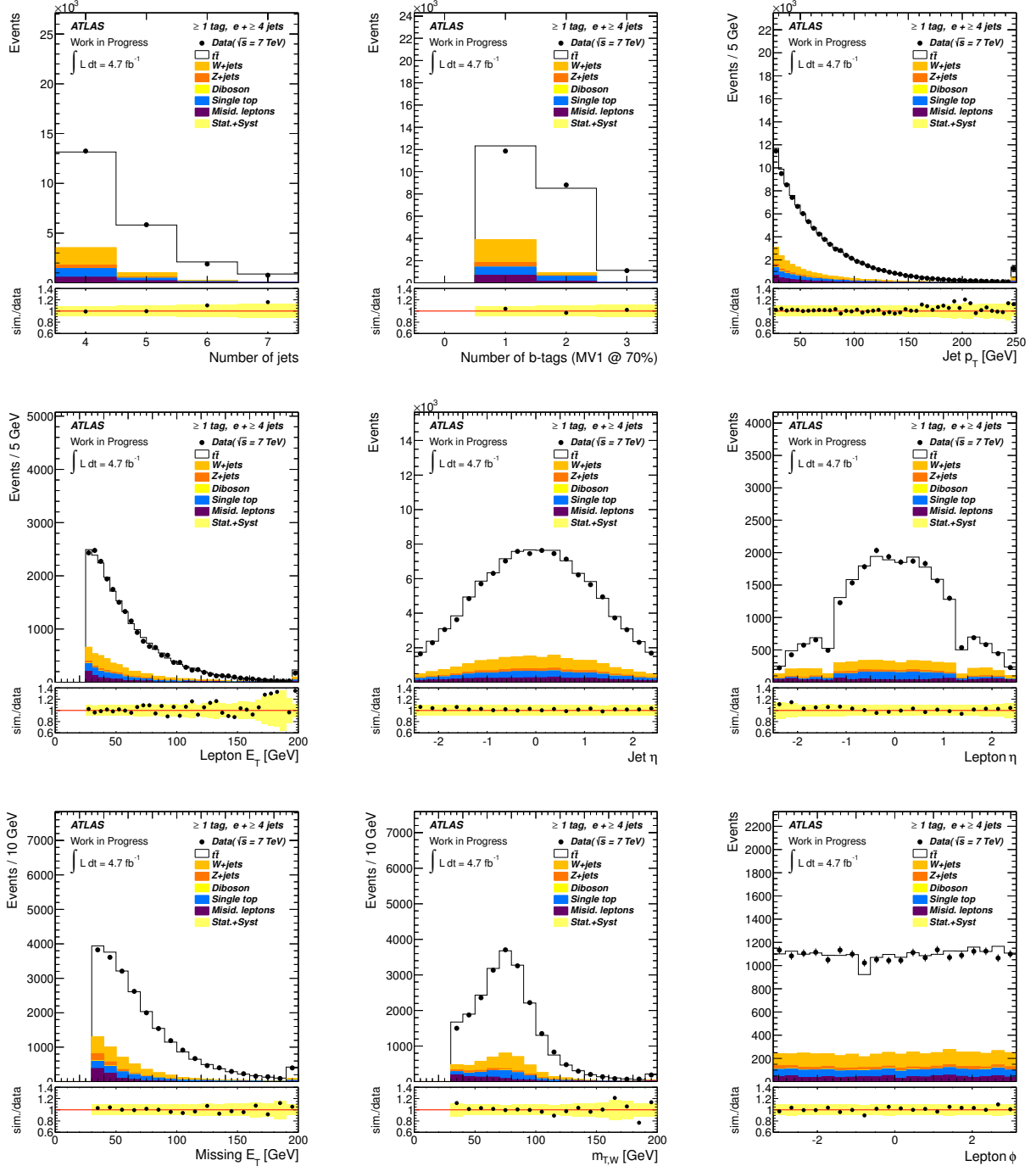
A.2.1. Standard Selection - Powheg+Pythia

Figure A.1.: Kinematic distributions in the e+jets channel for standard $t\bar{t}$ selection with Powheg+Pythia $t\bar{t}$ simulation. The uncertainty band in the ratio plots includes statistical, cross-section and luminosity uncertainties.

Figure A.2.: Kinematic distributions in the μ+jets channel for standard $t\bar{t}$ selection with POWHEG+PYTHIA $t\bar{t}$ simulation. The uncertainty band in the ratio plots includes statistical, cross-section and luminosity uncertainties.
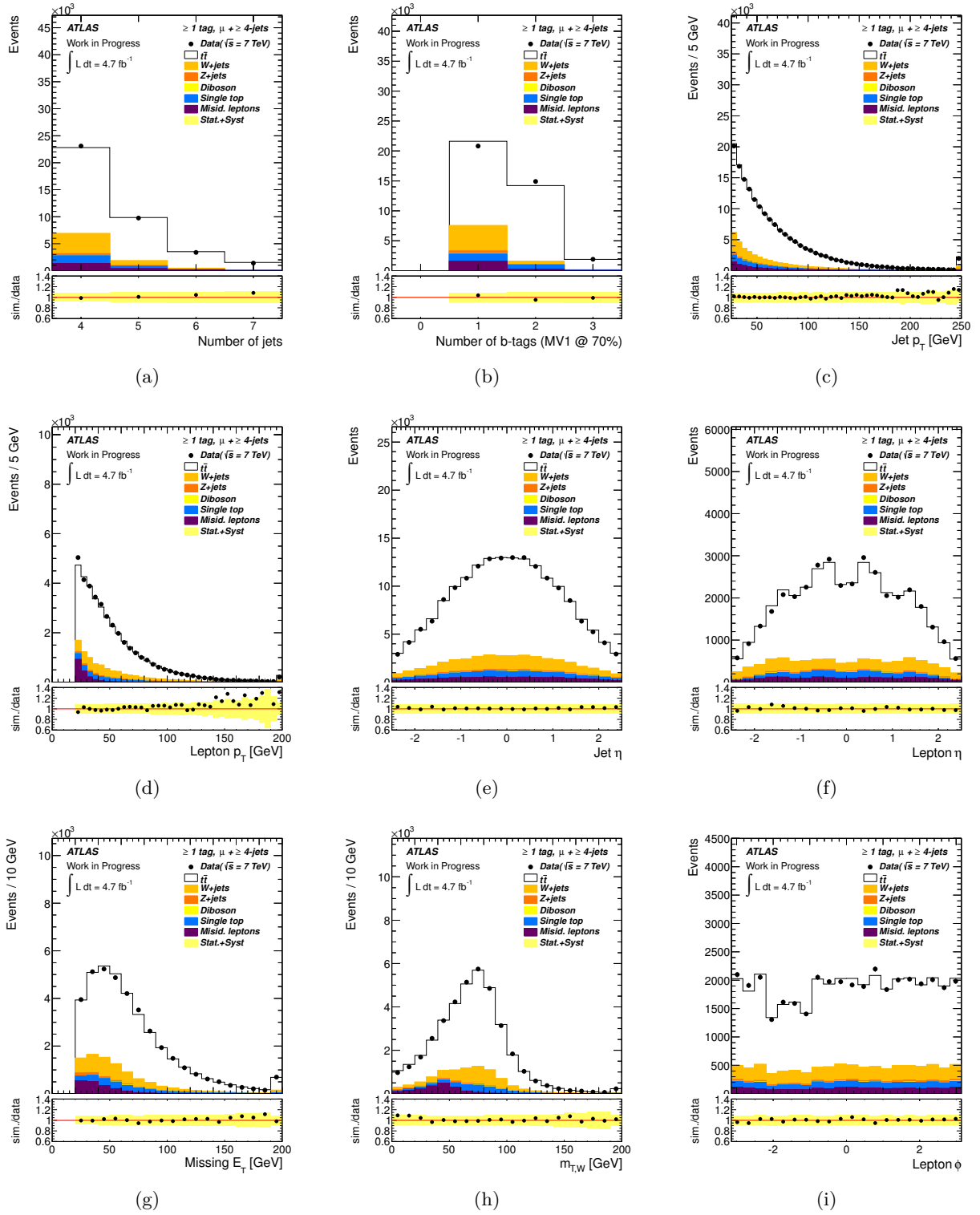
	e+jets		μ+jets	
Process	Events	Uncertainty	Events	Uncertainty
$t\bar{t}$ (POWHEG+PYTHIA)	17 092	1 856	28 417	3 085
Single top	1 204	165	2 005	247
W+jets	2 337	567	4 907	1 117
Z+jets	452	250	488	257
Diboson	47	12	74	17
Multijet	838	419	1 830	367
Total predicted	21 968	1 961	37 721	3 234
Observed	21 770		37 645	
S/B	3.50		3.05	

Table A.6.: Number of events per process for e+jets and μ+jets channel for the standard $t\bar{t}$ selection (≥ 4 jets and ≥ 1 b-tag). The prediction is compared with the observed data. The ratio signal over background (S/B) is also shown.
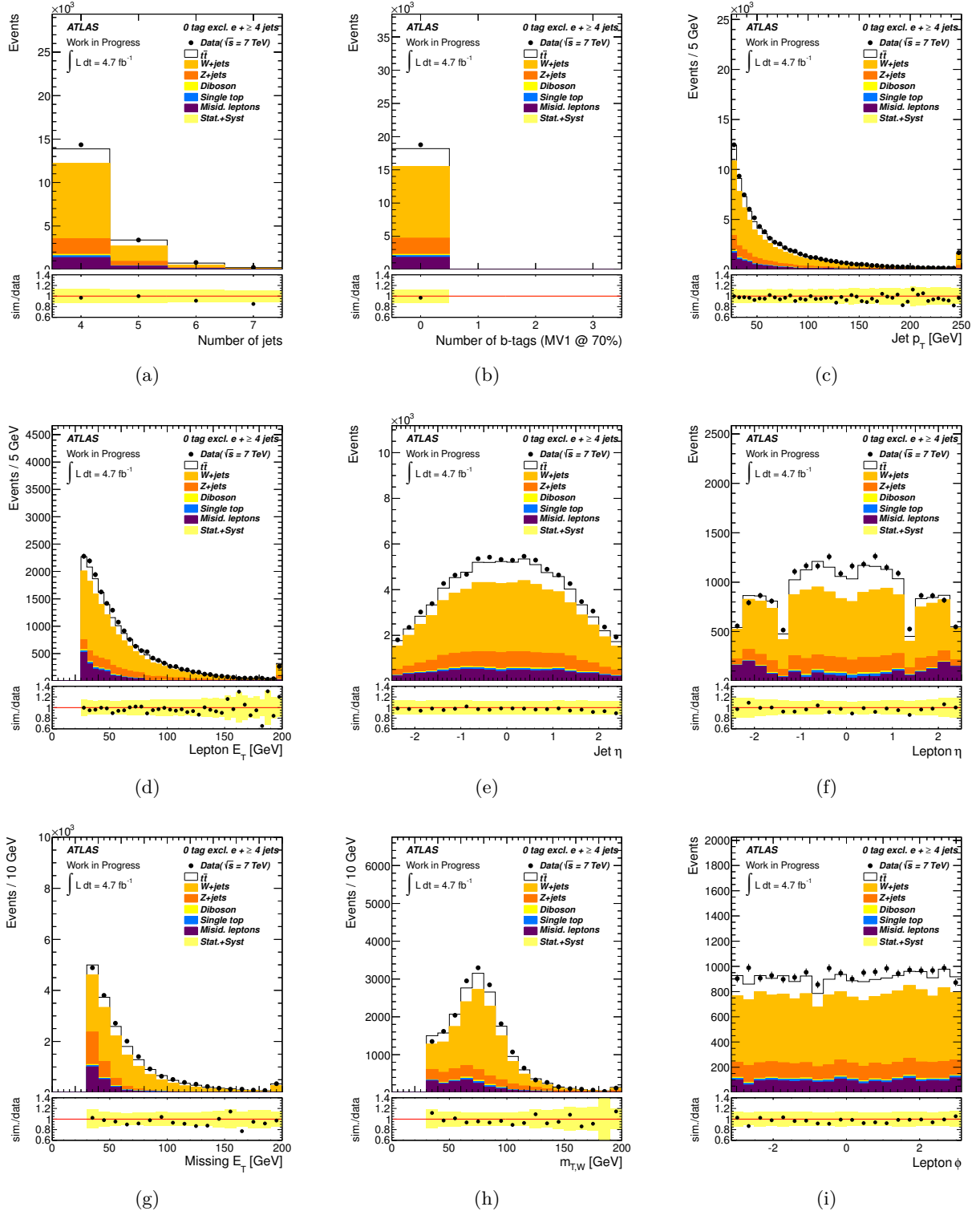
A.2.2. Zero exclusive *b*-tag region - Protos

Figure A.3.: Kinematic distributions in the *e*+jets channel for 0 excl *b*-tag *tt̄* selection with PROTOS *tt̄* simulation. The uncertainty band in the ratio plots includes statistical, cross-section and luminosity uncertainties.

Figure A.4.: Kinematic distributions in the μ+jets channel for 0excl b-tag $t\bar{t}$ selection with PROTOS $t\bar{t}$ simulation. The uncertainty band in the ratio plots includes statistical, cross-section and luminosity uncertainties.
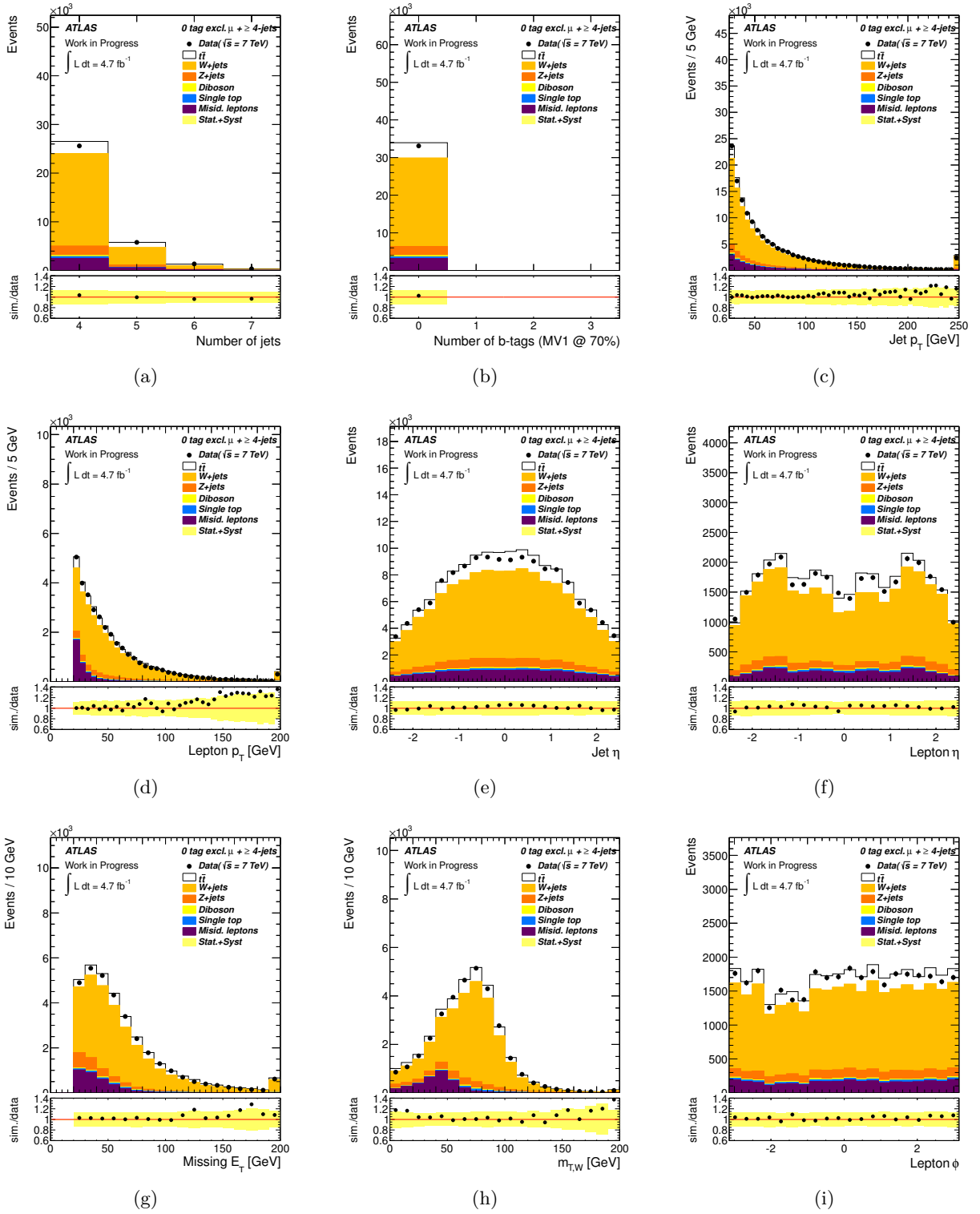
| | *e*+**jets** | | *μ*+**jets** | |
Process	Events	Uncertainty	Events	Uncertainty
$t\bar{t}$ (PROTOS)	2 696	316	4 088	467
Single top	274	25	453	38
W+jets	10 805	1 855	23 451	4 018
Z+jets	2 443	1 175	2 450	1 179
Diboson	185	12	303	19
Multijet	1 785	893	3 182	637
Total predicted	18 189	2 391	33 927	4 261
Observed	18 776		33 093	
S/B	0.17		0.14	

Table A.7.: Number of events per process for *e*+jets and *μ*+jets channel for 0 excl *b*-tag $t\bar{t}$ selection. The prediction is compared with the observed data. The ratio signal over background (S/B) is also shown.
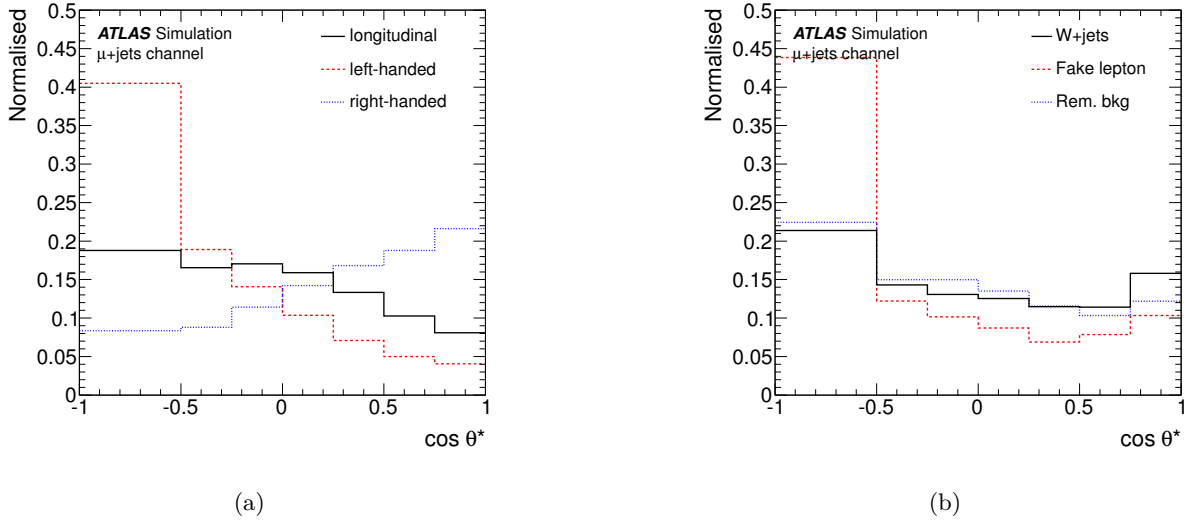
A.3. Templates

(a)   (b)

Figure A.5.: Signal (a) and background (b) templates with seven bins for the *μ*+jets channel with standard $t\bar{t}$ selection.

A.4. Template Fit

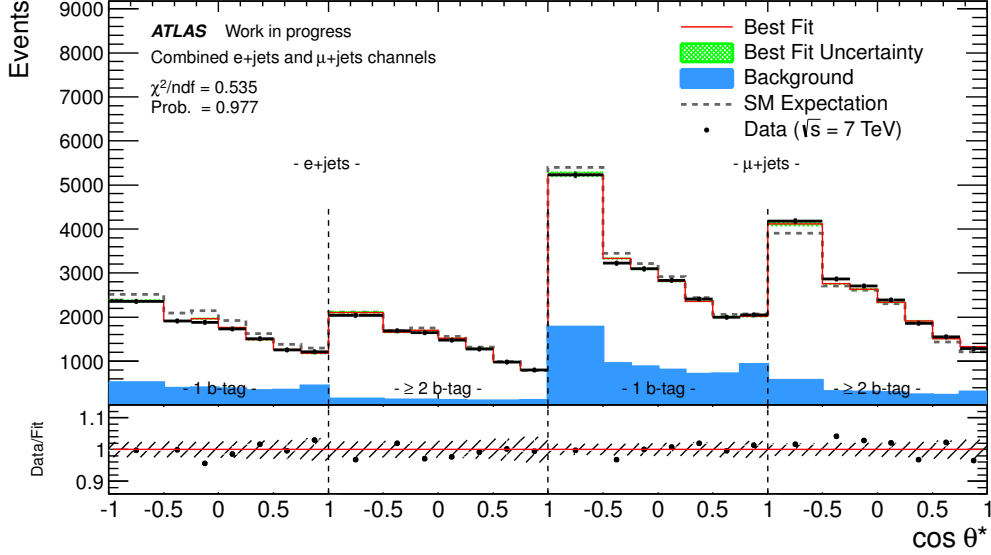### A.4.1. Template Fit in Four Channels with 15 Templates

Figure A.6.: Template fit result in four channels with 15 templates: the red line is the best fit result, the black points are the data. The blue area is the fitted background contribution, the hashed bands give the statistical uncertainty of the fit. The reduced χ^2 and probability of the fit are also given.
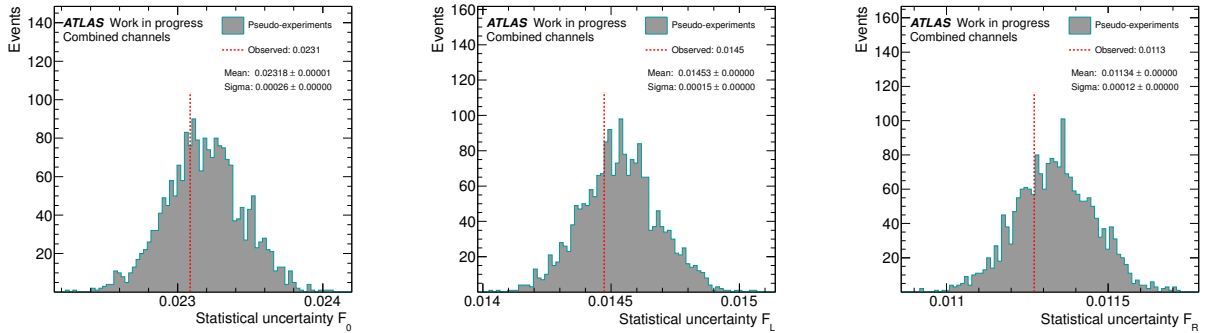

Figure A.7.: Comparison of expected uncertainty (mean value of pseudo-data distribution) with uncertainty from data fit output (dashed line) for the four channel fit with 15 templates. 2 000 ensembles were created from the data fit output fractions for F_0, F_L and F_R.

Fit setup	F_0	F_L	F_R
Four channels, 15 templates	0.625±0.023	0.338±0.015	0.037±0.011

Table A.8.: Measured helicity fractions in combined template fit in four channels to data with 15 templates.
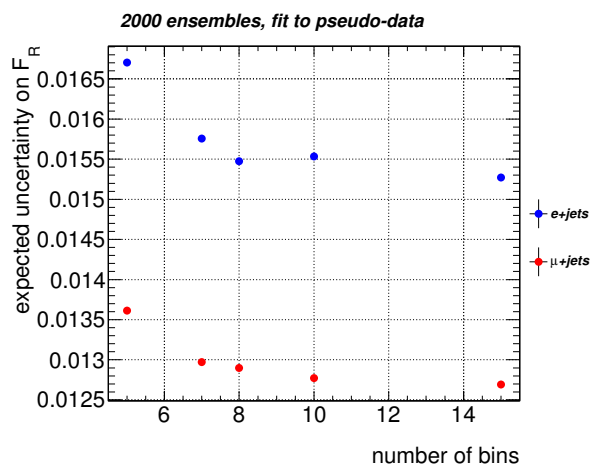
A.5. Uncertainty as function of number of bins

Figure A.8.: Expected statistical uncertainty on F_R as a function of number of bins. The background was fixed in the template fit.

Bibliography

[1] A. Czarnecki, J. G. Korner, J. H. Piclum, *Helicity fractions of W bosons from top quark decays at NNLO in QCD*, Phys. Rev. **D81**, 111503 (2010)

[2] G. Aad, et al. (ATLAS Collaboration), *Observation of a new particle in the search for the Standard Model Higgs boson with the ATLAS detector at the LHC*, Phys. Lett. **B716**, 1 (2012)

[3] S. Chatrchyan, et al. (CMS Collaboration), *Observation of a new boson at a mass of 125 GeV with the CMS experiment at the LHC*, Phys. Lett. **B716**, 30 (2012)

[4] T. Aaltonen, et al. (CDF Collaboration, DØ Collaboration), *Combination of the top-quark mass measurements from the Tevatron collider*, Phys. Rev. **D86**, 092003 (2012)

[5] S. Weinberg, *The Making of the Standard Model*, Eur. Phys. J. **C34**, 5 (2004)

[6] A. Salam, *Weak and Electromagnetic Interactions*, ed. Nobel Symposium No. 8 (Almqvist & Wiksell, Stockholm, 1968)

[7] D. J. Gross, F. Wilczek, *Asymptotically Free Gauge Theories*, Phys. Rev. **D8**, 3633 (1973)

[8] S. Weinberg, *A Model of Leptons*, Phys. Rev. Lett. **19**, 1264 (1967)

[9] H. D. Politzer, *Asymptotic Freedom: An Approach to Strong Interactions*, Phys. Rept. **14**, 129 (1974)

[10] J. Beringer, et al. (Particle Data Group), Phys. Rev. **D86**, 010001 (2012)

[11] C. Kraus, et al., *Final results from phase II of the Mainz neutrino mass searchin tritium β decay*, Eur. Phys. J. **C40(4)**, 447 (2005)

[12] V. N. Aseev, et al., *Upper limit on the electron antineutrino mass from the Troitsk experiment*, Phys. Rev. **D84**, 112003 (2011)

[13] K. Assamagan, et al., *Upper limit of the muon-neutrino mass and charged-pion mass from momentum analysis of a surface muon beam*, Phys. Rev. **D53**, 6065 (1996)

[14] R. Barate et al., *An upper limit on the τ neutrino mass from three- and five-prong tau decays*, Eur. Phys. J. **C2(3)**, 395 (1998)

[15] M. Altmann, et al. (GNO COLLABORATION), *Complete results for five years of GNO solar neutrino observations*, Phys. Lett. **B616**, 174 (2005)

[16] M. H. Ahn, et al. (K2K Collaboration), *Measurement of neutrino oscillation by the K2K experiment*, Phys. Rev. **D74**, 072003 (2006)

[17] Y. Fukuda, et al. (The Super-Kamiokande Collaboration), *Measurement of the Flux and Zenith-Angle Distribution of Upward Throughgoing Muons by Super-Kamiokande*, Phys. Rev. Lett. **82**, 2644 (1999)

[18] P. Adamson, et al. (MINOS Collaboration), *Measurement of the Neutrino Mass Splitting and Flavor Mixing by MINOS*, Phys. Rev. Lett. **106**, 181801 (2011)

[19] T. Lasserre, et al., *Comment on Phys. Rev. Lett. 108, 191802 (2012): 'Observation of Reactor Electron Antineutrino Disappearance in the RENO Experiment'* (2012)

[20] H. Georgi, S. L. Glashow, *Unified Weak and Electromagnetic Interactions without Neutral Currents*, Phys. Rev. Lett. **28**, 1494 (1972)

[21] M. Goldhaber, L. Grodzins, A. W. Sunyar, *Helicity of Neutrinos*, Phys. Rev. **109**, 1015 (1958)

[22] N. Cabibbo, *Unitary Symmetry and Leptonic Decays*, Phys. Rev. Lett. **10**, 531 (1963)

[23] M. Kobayashi, T. Maskawa, *CP Violation in the Renormalizable Theory of Weak Interaction*, Prog. Theor. Phys. **49**, 652 (1973)

[24] Z. Maki, M. Nakagawa, S. Sakata, *Remarks on the unified model of elementary particles*, Prog. Theor. Phys. **28(5)**, 870 (1962)

[25] B. Pontecorvo, *Neutrino experiments and the problem of conservation of leptonic charge*, Sov. Phys. JETP **26(984-988)**, 165 (1968)

[26] B. Pontecorvo, *Mesonium and antimesonium*, Zhur. Eksptl'. i Teoret. Fiz. **33** (1957)

[27] P. Higgs, *Broken symmetries, massless particles and gauge fields*, Phys. Lett. **12(2)**, 132 (1964)

[28] F. Englert, R. Brout, *Broken Symmetry and the Mass of Gauge Vector Mesons*, Phys. Rev. Lett. **13**, 321 (1964)

[29] G. S. Guralnik, C. R. Hagen, T. W. B. Kibble, *Global Conservation Laws and Massless Particles*, Phys. Rev. Lett. **13**, 585 (1964)

[30] *Combined measurements of the mass and signal strength of the Higgs-like boson with the ATLAS detector using up to 25 fb^{-1} of proton-proton collision data*, Technical Report ATLAS-CONF-2013-014, CERN, Geneva (2013)

[31] *Combination of standard model Higgs boson searches and measurements of the properties of the new boson with a mass near 125 GeV*, Technical Report CMS-PAS-HIG-13-005, CERN, Geneva (2013)

[32] F. Zwicky, *On the Masses of Nebulae and of Clusters of Nebulae*, Astrophys. J. **86**, 217 (1937)

[33] C. L. Bennett, et al., *First-Year Wilkinson Microwave Anisotropy Probe (WMAP) Observations: Foreground Emission*, Astrophys. J. Supplement Series **148(1)**, 97 (2003)

[34] P. Ade, et al. (Planck Collaboration), *Planck 2013 results. I. Overview of products and scientific results* (2013)

[35] E. Majorana, *Teoria simmetrica dell'elettrone e del positrone*, Il Nuovo Cimento **14(4)**, 171 (1937)

[36] S. Martin, *A Supersymmetry Primer* (1997)

[37] H. P. Nilles, *Supersymmetry, supergravity and particle physics*, Phys. Rep. **110**, 1 (1984)

[38] R. N. Cahn, *The Eighteen arbitrary parameters of the standard model in your everyday life*, Rev. Mod. Phys. **68**, 951 (1996)

[39] S. Abachi, et al. (DØ), *Observation of the Top Quark*, Phys. Rev. Lett. **74**, 2632 (1995)

[40] F. Abe, et al. (CDF), *Observation of Top Quark Production in $p\bar{p}$ Collisions with the Collider Detector at Fermilab*, Phys. Rev. Lett. **74**, 2626 (1995)

[41] G. Alexander, et al. (LEP Collaborations, ALEPH Collaboration, DELPHI Collaboration, L3 Collaboration, OPAL Collaboration), *Electroweak parameters of the Z^0 resonance and the Standard Model: the LEP Collaborations*, Phys. Lett. **B276**, 247 (1992)

[42] I. I. Y. Bigi, et al., Phys. Lett. **B181**, 157 (1986)

[43] H.-L. Lai, M. Guzzi, J. Huston, Z. Li, P. M. Nadolsky, et al., *New parton distributions for collider physics*, Phys. Rev. **D82**, 074024 (2010)

[44] *Online PDF plotting and calculation*, retrieved on 27/02/2013 URL http://hepdata.cedar.ac.uk/pdf/pdf3.html

[45] M. Cacciari, et al., Sov. Phys. JETP **04**, 068 (2004)

[46] T. M. Liss, A. Quadt (Particle Data Group), *The Top Quark*, Phys. Rev. **D86**, 010001 (2012)

[47] V. Abazov, et al. (DØ Collaboration), *Observation of Single Top Quark Production*, Phys. Rev. Lett. **103**, 092001 (2009)

[48] T. Aaltonen, et al. (CDF Collaboration), *First Observation of Electroweak Single Top Quark Production*, Phys. Rev. Lett. **103**, 092002 (2009)

[49] N. Kidonakis, *Single top quark production at the Fermilab Tevatron: Threshold resummation and finite-order soft gluon corrections*, Phys. Rev. **D74**, 114012 (2006)

[50] F. A. Berends, H. Kuijf, B. Tausk, W. T. Giele, *On the production of a W and jets at hadron colliders*, Nucl. Phys. **B357(1)**, 32 (1991)

[51] *Single Top associated tW production at 8 TeV in the two lepton final state*, Technical Report CMS-PAS-TOP-12-040, CERN, Geneva (2013)

[52] S. Chatrchyan, et al. (CMS Collaboration), *Evidence for Associated Production of a Single Top Quark and W Boson in pp Collisions at $\sqrt{s} = 7$ TeV*, Phys. Rev. Lett. **110**, 022003 (2013)

[53] G. Aad, et al. (ATLAS Collaboration), *Evidence for the associated production of a W boson and a top quark in ATLAS at $\sqrt{s} = 7$ TeV*, Phys. Lett. **B716(1)**, 142 (2012)

[54] G. L. Kane, G. A. Ladinsky, C. P. Yuan, *Using the top quark for testing standard-model polarization and CP predictions*, Phys. Rev. **D45(1)**, 124 (1992)

[55] D. Acosta, et al. (CDF Collaboration), *Measurement of the W boson polarization in top decay at CDF at $\sqrt{s} = 1.8$ TeV*, Phys. Rev. **D71**, 031101 (2005)

[56] T. Affolder, et al. (CDF), *Measurement of the Helicity of W Bosons in Top Quark Decays*, Phys. Rev. Lett. **84**, 216 (2000)

[57] A. Abulencia, et al. (CDF Collaboration), *Measurement of the helicity of W bosons in top-quark decays*, Phys. Rev. **D73**, 111103 (2006)

[58] G. Aad, et al. (ATLAS Collaboration), *Measurement of the W boson polarization in top quark decays with the ATLAS detector*, JHEP **1206**, 088 (2012)

[59] J. Aguilar-Saavedra, J. Carvalho, N. F. Castro, F. Veloso, A. Onofre, *Probing anomalous Wtb couplings in top pair decays*, Eur. Phys. J. **C50**, 519 (2007)

[60] *Combination of the ATLAS and CMS measurements of the W-boson polarization in top-quark decays*, Technical Report ATLAS-CONF-2013-033, CERN, Geneva (2013)

[61] L. Lyons, D. Gibaut, P. Clifford, *How to combine correlated estimates of a single physical quantity*, Nucl. Instrum. Meth. **A270**, 110 (1988)

[62] W. Buchmüller, D. Wyler, *Effective lagrangian analysis of new interactions and flavour conservation*, Nucl. Phys. **B268(3–4)**, 621 (1986)

[63] J. Aguilar-Saavedra, *A Minimal set of top anomalous couplings*, Nucl. Phys. **B812**, 181 (2009)

[64] C. Zhang, S. Willenbrock, *Effective-Field-Theory Approach to Top-Quark Production and Decay*, Phys. Rev. **D83**, 034006 (2011)

[65] J. Aguilar-Saavedra, *Single top quark production at LHC with anomalous Wtb couplings*, Nucl. Phys. **B804**, 160 (2008)

[66] S. Chatrchyan, et al. (CMS Collaboration), *Measurement of the single-top-quark t-channel cross section in pp collisions at $\sqrt{s} = 7$ TeV*, JHEP **2012(12)**, 1 (2012)

[67] G. Aad, et al. (ATLAS Collaboration), *Measurement of the t-channel single top-quark production cross section in pp collisions at $\sqrt{s} = 7$ TeV with the ATLAS detector*, Phys. Lett. **B717**, 330 (2012)

[68] S. Chatrchyan, et al. (CMS Collaboration), *Measurement of the W-boson helicity in top-quark decays from ttbar production in lepton+jets events in pp collisions at sqrt(s)=7 TeV* (2013)

[69] G. Aad, E. Abat, J. Abdallah, A. Abdelalim, A. Abdesselam, O. Abdinov, B. Abi, M. Abolins, H. Abramowicz, E. Acerbi, et al., *The ATLAS experiment at the CERN large hadron collider*, JINST **3**, S08003 (2008)

[70] *ATLAS detector and physics performance: Technical Design Report, 1*, Technical Design Report ATLAS, CERN, Geneva (1999)

[71] L. R. Evans, *The Large Hadron Collider (LHC)*, Eur. Phys. J. **C34**, S11 (2004)

[72] *CMS Detector and Physics Performance Technical Design Report*, CERN/LHCC-2006-001 (2006)

[73] *ALICE: Technical proposal for a Large Ion collider Experiment at the CERN LHC*, LHC Tech. Proposal, CERN, Geneva (1995)

[74] S. Amato, et al. (LHCb Collaboration), *LHCb technical proposal* (1998)

[75] Luminosity Public Results - ATLAS Public Results (Aug. 2013), URL https://twiki.cern.ch/twiki/bin/view/AtlasPublic/LuminosityPublicResults

[76] G. Aad, et al. (ATLAS Collaboration), *Improved luminosity determination in pp collisions at sqrt(s) = 7 TeV using the ATLAS detector at the LHC* (2013)

[77] K. Bachas, et al., *A measurement of the ATLAS muon reconstruction and trigger efficiency using J/psi decays*, Technical Report ATLAS-COM-CONF-2011-002, CERN, Geneva (2011)

[78] *Muon reconstruction efficiency in reprocessed 2010 LHC proton-proton collision data recorded with the ATLAS detector*, Technical Report ATLAS-CONF-2011-063, CERN, Geneva (2011)

[79] G. Aad, et al., *Electron performance measurements with the ATLAS detector using the 2010 LHC proton-proton collision data*, Eur. Phys. J. **C72(3)**, 1 (2012)

[80] F. Kohn, *Measurement of the charge asymmetry in top-quark pair production in pp collision data at $\sqrt{7}$ TeV using the ATLAS detector*, II.Physik-UniGö-Diss-2012-03 (2012)

[81] M. Cacciari, G. P. Salam, G. Soyez, *The anti-k_t jet clustering algorithm*, JHEP **2008(04)**, 063 (2008)

[82] *Commissioning of the ATLAS high-performance b-tagging algorithms in the 7 TeV collision data*, Technical Report ATLAS-CONF-2011-102, CERN, Geneva (2011)

[83] *Measuring the b-tag efficiency in a top-pair sample with 4.7 fb^{-1} of data from the ATLAS detector*, Technical Report ATLAS-CONF-2012-097, CERN, Geneva (2012)

[84] G. Aad, et al. (ATLAS Collaboration), *Performance of Missing Transverse Momentum Reconstruction in Proton-Proton Collisions at 7 TeV with ATLAS*, Eur. Phys. J. **C72**, 1844 (2012)

[85] M. Denny, *Introduction to importance sampling in rare-event simulations*, Eur. Phys. J. **22(4)**, 403 (2001)

[86] T. Sjostrand, S. Mrenna, P. Z. Skands, *PYTHIA 6.4 Physics and Manual*, JHEP **0605**, 026 (2006)

[87] G. Corcella, et al., *HERWIG 6: an event generator for hadron emission reactions with interfering gluons (including supersymmetric processes)*, JHEP **0101**, 010 (2001)

[88] T. Gleisberg, S. Hoeche, F. Krauss, A. Schälicke, S. Schumann, J. Winter, *SHERPA 1.α, a proof-of-concept version*, JHEP **0402**, 056 (2004)

[89] G. Altarelli, G. Parisi, *Asymptotic freedom in parton language*, Nucl. Phys. **B126(2)**, 298 (1977)

[90] V. Gribov, L. Lipatov, *Deep inelastic e p scattering in perturbation theory*, Sov. J. Nucl. Phys. **15**, 438 (1972)

[91] Y. L. Dokshitzer, *Calculation of the Structure Functions for Deep Inelastic Scattering and e^+e^- Annihilation by Perturbation Theory in Quantum Chromodynamics.*, Sov. Phys. JETP **46**, 641 (1977)

[92] V. Sudakov, *Vertex parts at very high-energies in quantum electrodynamics*, Sov. Phys. JETP **3**, 65 (1956)

[93] B. Andersson, G. Gustafson, G. Ingelman, T. Sjostrand, *Parton Fragmentation and String Dynamics*, Phys. Rept. **97**, 31 (1983)

[94] B. Webber, *A QCD Model for Jet Fragmentation Including Soft Gluon Interference*, Nucl. Phys. **B238**, 492 (1984)

[95] S. Agostinelli, et al. (Geant4), *GEANT4: A Simulation Toolkit*, Nucl. Instrum. Meth. **A506**, 250 (2003)

[96] E. Richter-Was, D. Froidevaux, L. Poggioli, *ATLFAST 2.0 a fast simulation package for ATLAS* (1998)

[97] M. Cacciari, M. Czakon, M. Mangano, A. Mitov, P. Nason, *Top-pair production at hadron colliders with next-to-next-to-leading logarithmic soft-gluon resummation*, Phys. Lett. **B710**, 612 (2012)

[98] P. Baernreuther, M. Czakon, A. Mitov, *Percent Level Precision Physics at the Tevatron: First Genuine NNLO QCD Corrections to $q\bar{q} \to t\bar{t} + X$*, Phys. Rev. Lett. **109**, 132001 (2012)

[99] M. Czakon, A. Mitov, *NNLO corrections to top-pair production at hadron colliders: the all-fermionic scattering channels*, JHEP **1212**, 054 (2012)

[100] M. Czakon, A. Mitov, *NNLO corrections to top pair production at hadron colliders: the quark-gluon reaction*, JHEP **1301**, 080 (2013)

[101] M. Czakon, P. Fiedler, A. Mitov, *The total top quark pair production cross-section at hadron colliders through $\mathcal{O}(\alpha\_s^4)$*, Phys. Rev. Lett. **110**, 252004 (2013)

[102] M. Czakon, A. Mitov, *Top++: A Program for the Calculation of the Top-Pair Cross-Section at Hadron Colliders* (2011)

[103] J. Pumplin, D. R. Stump, H. L. Lai, P. Nadolsky, W. K. Tung, *New generation of parton distributions with uncertainties from global QCD analysis*, JHEP **0207**, 012 (2002)

[104] B. P. Kersevan, E. Richter-Was, *The Monte Carlo event generator AcerMC version 2.0 with interfaces to PYTHIA 6.2 and HERWIG 6.5* (2004)

[105] S. Frixione, B. Webber, *The MC@NLO Event Generator* (2004)

[106] M. L. Mangano, et al., *ALPGEN, a generator for hard multiparton processes in hadronic collisions*, JHEP **0307**, 001 (2003)

[107] M. L. Mangano, M. Moretti, F. Piccinini, M. Treccani, *Matching matrix elements and shower evolution for top-quark production in hadronic collisions*, JHEP **0701**, 013 (2007)

[108] G. Aad, et al. (ATLAS Collaboration), *Measurement of the charge asymmetry in top quark pair production in pp collisions at $\sqrt{s} = 7$ TeV using the ATLAS detector*, Eur. Phys. J. **C72**, 2039 (2012)

[109] G. Aad, et al. (ATLAS Collaboration), *Measurement of the $W \to \ell\nu$ and $Z/\gamma^* \to \ell\ell$ production cross sections in proton-proton collisions at $\sqrt{s} = 7$ TeV with the ATLAS detector*, JHEP **1012**, 060 (2010)

[110] G. Aad, et al. (ATLAS Collaboration), *Measurement of the top quark mass with the template method in the $t\bar{t} \to$ lepton + jets channel using ATLAS data*, Eur. Phys. J. **C72**, 2046 (2012)

[111] S. Guindon, *A Top Quark Mass Measurement Using the Stabilized R_32 Variable with the ATLAS Detector*, II.Physik-UniGö-Diss-2012/07 (2012)

[112] R. A. Fisher, *On an absolute criterion for fitting frequency curves*, Messenger of Mathematics **41**, 155 (1912)

[113] J. Aldrich, *R. A. Fisher and the Making of Maximum Likelihood 1912-1922*, Statistical Science **12(3)**, pp. 162 (1997)

[114] F. James, *MINUIT—A System for Function Minimization and Analysis of the Parameter Errors and Correlations*, Computer Physics Communications **10**, 343 (1975)

[115] O. Behnke, K. Kröninger, G. Schott, T. Schörner-Sadenius, *Data Analysis in High Energy Physics: A Practical Guide to Statistical Methods*, Wiley (2013)

[116] R. Brun, F. Rademakers, *ROOT - An object oriented data analysis framework*, Nucl. Instrum. Meth. **389(12)**, 81 (1997)

[117] A. Henrichs, *Precision Measurements of the Top Quark Pair Production Cross Section in the Single Lepton Channel with the ATLAS Experiment*, II.Physik-UniGö-Diss-2012/05 (2012)

[118] P. Stolte, *Studies of Top Quark Properties Using a Profile Likelihood Fit at ATLAS*, II.Physik-UniGö-MSc-2012/06 (2012)

[119] A. Knue, *Measurement of the W-boson Polarisation in Top-Quark Decays with the ATLAS Detector*, II.Physik-UniGö-Diss-2013/01 (2013)

[120] *Calibrating the b-Tag Efficiency and Mistag Rate in 35 pb^{-1} of Data with the ATLAS Detector*, Technical Report ATLAS-CONF-2011-089, CERN, Geneva (2011)

[121] *Jet energy scale and its systematic uncertainty in proton-proton collisions at sqrt(s)=7 TeV with ATLAS 2011 data*, Technical Report ATLAS-CONF-2013-004, CERN, Geneva (2013)

[122] G. Aad, et al. (ATLAS Collaboration), *Jet energy measurement with the ATLAS detector in proton-proton collisions at $\sqrt{s} = 7$ TeV*, Eur. Phys. J. **C73**, 2304 (2013)

[123] G. Aad, et al. (ATLAS Collaboration), *Jet energy resolution in proton-proton collisions at $\sqrt{s} = 7$ TeV recorded in 2010 with the ATLAS detector*, Eur. Phys. J. **C73**, 2306 (2013)

[124] *Combination of ATLAS and CMS results on the mass of the top quark using up to 4.9 fb^{-1} of data*, Technical Report ATLAS-CONF-2012-095, CERN, Geneva (2012)

[125] G. Watt, R. Thorne, *Study of Monte Carlo approach to experimental uncertainty propagation with MSTW 2008 PDFs*, JHEP **1208**, 052 (2012)

[126] R. D. Ball, et al. (NNPDF Collaboration), *Unbiased global determination of parton distributions and their uncertainties at NNLO and at LO*, Nucl. Phys. **B855**, 153 (2012)

[127] M. Whalley, D. Bourilkov, R. Group, *The Les Houches accord PDFs (LHAPDF) and LHAGLUE* (2005)

[128] M. L. Mangano, *Understanding the Standard Model, as a bridge to the discovery of new phenomena at the LHC*, Int. J. Mod. Phys. **A23**, 3833 (2008)

[129] G. Aad, et al. (ATLAS Collaboration), *Measurement of the top quark pair production cross-section with ATLAS in the single lepton channel*, Phys. Lett. **B711**, 244 (2012)

[130] G. Aad, et al. (ATLAS Collaboration), *Measurement of the top quark-pair production cross section with ATLAS in pp collisions at $\sqrt{s} = 7$ TeV*, Eur. Phys. J. **C71**, 1577 (2011)

[131] J. M. Campbell, R. K. Ellis, *Radiative corrections to Z b anti-b production*, Phys. Rev. **D62**, 114012 (2000)

[132] G. Aad, et al., *Electron performance measurements with the ATLAS detector using the 2010 LHC proton-proton collision data*, Eur. Phys. J. **C72(3)** (2012)

[133] *Muon Momentum Resolution in First Pass Reconstruction of pp Collision Data Recorded by ATLAS in 2010*, Technical Report ATLAS-CONF-2011-046, CERN, Geneva (2011)

[134] *Combination of ATLAS and CMS results on the mass of the top-quark using up to 4.9 fb^{-1} of $\sqrt{s} = 7$ TeV LHC data*, Technical Report ATLAS-CONF-2013-102, CERN, Geneva (2013)

Acknowledgement

First of all, I would like to thank my two supervisors Andrea Knue and Kevin Kröninger. They were the best supervisors I could wish for. Especially Andrea built the fundamental framework for this analysis which made it comparatively easy for me to obtain meaningful results in a short time. Thanks to both of you for many helpful discussions, ideas and support wherever and whenever it was needed.

Further thanks go to Lisa Shabalina for fruitful physics discussions and for assisting when I gave talks in ATLAS meetings. Thanks to Philipp Stolte for answering all my questions related to profile likelihood fits and his code. I am also grateful to Boris Lemmer for helping me with issues related to the TRC code and Grid related tasks without ever hesitating. Thanks to the whole HEP group of the II. Physikalisches Institut for providing an enjoyable atmosphere to work in. Also, I would like to thank my referees Prof. Dr. Arnulf Quadt and Prof. Dr. Ariane Frey, who both encouraged me to focus on particle physics and gave me the opportunity to participate in the Summer Students Programme at CERN. Special thanks to Arnulf Quadt for letting me work in his group and participate at the frontier of research and for encouraging me to make to best out of my possibilities.

Schließlich möchte ich mich bei meiner Familie bedanken für all die Unterstützung, die ich während des Studiums erfahren habe. Ohne euch wäre ein erfolgreiches Studium nicht möglich gewesen. Außerdem möchte ich mich bei meinen Freunden und Bojan bedanken, dass ihr immer da wart, wenn ich euch gebraucht habe.

Erklärung nach §18(8) der Prüfungsordnung für den Bachelor-Studiengang Physik und den Master-Studiengang Physik an der Universität Göttingen:

Hiermit erkläre ich, dass ich diese Abschlussarbeit selbständig verfasst habe, keine anderen als die angegebenen Quellen und Hilfsmittel benutzt habe und alle Stellen, die wörtlich oder sinngemäß aus veröffentlichten Schriften entnommen wurden, als solche kenntlich gemacht habe. Darüberhinaus erkläre ich, dass diese Abschlussarbeit nicht, auch nicht auszugsweise, im Rahmen einer nichtbestandenen Prüfung an dieser oder einer anderen Hochschule eingereicht wurde.

Göttingen, den 7. Dezember 2013

(Cora Fischer)